Politecnico di Torino

Corso di Laurea Magistrale in
Electronics Engineering for Micro & Nano Systems

Tesi di Laurea Magistrale

Towards graphene decoration with nanoparticles for enhanced gas sensing

Relatori:
prof. Matteo Cocuzza
prof. Massimo Mastrangeli
prof. Sten Vollebregt

Candidato:
Niccolò Bandinelli

Anno Accademico 2019/2020

Contents

Part I

Introduction

Research objectives

The aim of this thesis project is to investigate the possibility of decorating graphene with nanoparticles to enhance performance of graphene-based gas sensors. In recent years, graphene has attracted particular attention in the field of gas sensing. The affinity of such material with numerous gas species, the ability to operate at room temperature and the large specific surface area are just some of the characteristics that make it a promising material.

However, the use of graphene has some limitations that make it difficult to be exploited in commercial sensors. Among these limitations: the low selectivity towards different analyte, the difficult of the signal to reach saturation and to return at the initial level during the restoration phase. The functionalization of graphene, through the introduction of doping elements on the its surface, turns out to be the most promising method. In particular in this work we will investigate if graphene obtained by chemical vapour deposition with methane on molybdenum catalyst is a suitable material to be decorated with nanoparticles using capillary assembly technique.

Thesis Outline

This thesis work divided in three main parts:

- Literature review: the state of the art about graphene fabrication and its sensing properties toward different gases is presented.
- Experimental results: the graphene will be fabricated and characterized inside the EKL cleanroom facility, moreover all the instruments needed for the capillary assembly will be set up.
- Conclusions: final consideration on the work done and future prospectives.

Part II

Literature review

Chapter 1

Graphene

Through history, technological developments has been the measure of progress, economy and social changes of a community. Each era is named from a crucial material, whose discovery or exploitation marks a radical change in the structure and socio-economic architecture. From the stone age, through that of copper, bronze, iron and steel, up to nowadays silicon age, scientific and technological progress has influenced progressively our life and habits. In every age, technology evolves with our needs and makes possible what was impossible in the past. In 2004 Andrei Geim and Konstantin Novoselov form University of Manchester were able to isolate for the first time graphene from graphite flake by mechanically peeling it with Scotch® tape [1]. This was a real breakthrough for science that let Geim and Novoselov won the Nobel Prize in 2010; before their experiment graphene was thought to be unstable at room temperature due to its extremely low thickness. Graphene and 2D materials more in general are very interesting, they showed unusual physical properties that will be pointed out in the next sections, they are promising material to solve the future technological challenges. Starting from 2012 the European Union invested 1 billion euros in the Graphene Flagship consortium which involves over 150 academic and industrial research groups (TU Delft is one of these) in 23 countries. There are good chances that next era cold be the *2D materials* era.

1.1 Crystalline structure

Carbon is one of the most interesting and important elements of the periodic table. It has atomic number 6 and it is an essential element for organic life together with hydrogen and oxygen, and it is the fundamental building block of graphene.

In its electronic configuration, carbon has two electrons in the inner $1s$ shell which are not involved in bonding, two electrons in the $2s$ orbital and two electrons in the $2p$ orbital. Orbitals $2p$ and $2s$ are very narrow energy levels (2s orbital is approximately 4eV lower than the 2p), for this reason it could happen that electrons from the $2s$ orbital jump in the $2p$ orbital that is not completely filled up. This phenomenon is called *hybridization* and it is the reason why carbon can be found in nature in so many different form with different properties, from the organic compounds (methane, glucose) to the pure carbon compounds (diamond, graphite).

When only one electron jump from the $2s$ to the $2p$ orbital this is called sp^2 hybridization, thanks to this kind of hybridization, graphene can be formed. In Figure 1.1 sp^2 hybridization is schematically represented remembering that electrons arrange themselves in energy levels by filling up the lower energy levels before and by following the Pauli exclusion's principle. The final result is 3 sp^2 orbitals ($2s$,$2p_x$,$2p_y$) that form the strong planar σ bond, that gives strength and stability properties to graphene while the remaining electron occupy the $2p_x$ orbital and form a π bond out of graphene plane, all these de-localized electrons involved in π bonds are identified as Van der Waals interactions that are responsible for the extraordinary electrical properties of graphene [2]. This is also graphically represented in Figure 1.1.

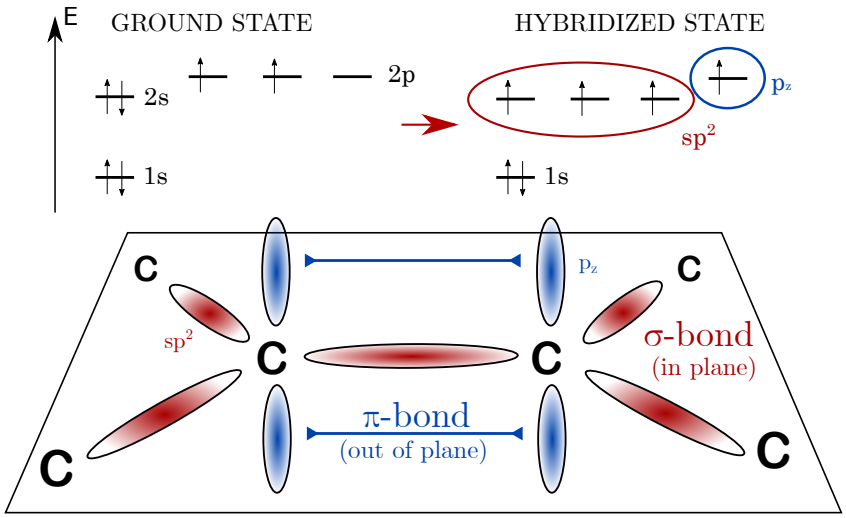

Figure 1.1: Graphical representation of sp^2 hybridization of carbon and bonding between sp^2-hybridized carbon atoms in the graphene unit cell.

Due to sp^2 hybridization each atom binds with other 3 carbon atoms forming a 120° angle. Graphene consists of a single layer of carbon atoms arranged in a honeycomb lattice. This crystalline structure is not a Bravais lattice but can be viewed as two interpenetrating triangular lattices A and B like shown in Figure 1.2. Each atom from sublattice A being surrounded by three atoms from sublattice B and vice versa (bipartite lattice). The distance between A and B atoms is $a_0 = 1.42$ Å and is called neighbour interatomic distance while the lattice constant is $a = \sqrt{3}a_0$. A base of vectors called primitive vectors can be created which, through a linear combination, allow us to identify each point on the lattice. In this case we have a two-dimensional crystal, so we call these vectors $\vec{a_1}$ and $\vec{a_2}$. The Bravais lattice could be mathematically defined as the set of vectors $\mathbf{R} = n_1\vec{a_1} + n_2\vec{a_2}$ with n_1 and n_2 integers. The unit cell of graphene lattice is highlighted in Figure 1.2, the real space basis vectors of this unit cell can then be written as:

$$\vec{a_1} = \begin{pmatrix} \sqrt{3}a/2 \\ a/2 \end{pmatrix} \vec{a_2} = \begin{pmatrix} \sqrt{3}a/2 \\ -a/2 \end{pmatrix}$$

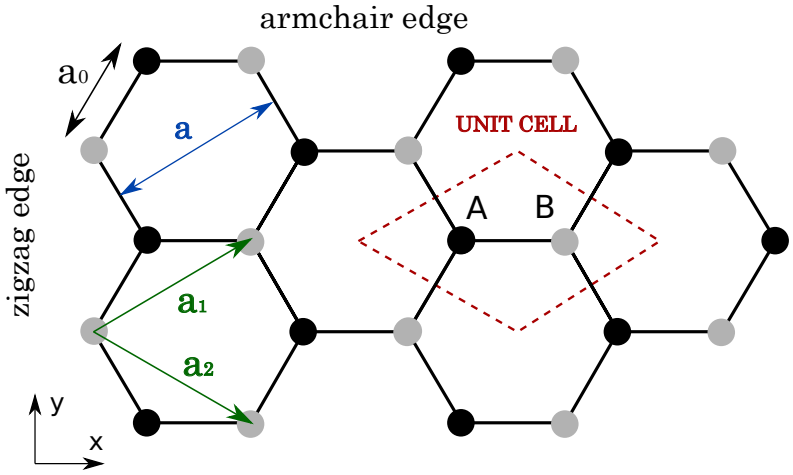

Figure 1.2: Graphene honeycomb lattice made by sublattices A (black) and B (grey), primitive vector $\vec{a_1}$ e $\vec{a_2}$ and unit cell are also highlighted [3].

The reciprocal lattice and its Wigner-Seitz primitive cell, defined as first Brillouin zone, are depicted in Figure 1.3, where $\vec{b_1}$ and $\vec{b_2}$ are the reciprocal basis vectors, expressed as:

$$\vec{b_1} = \begin{pmatrix} 2\pi/\sqrt{3}a \\ 2\pi/a \end{pmatrix} \vec{b_2} = \begin{pmatrix} 2\pi/\sqrt{3}a \\ -2\pi/a \end{pmatrix}$$

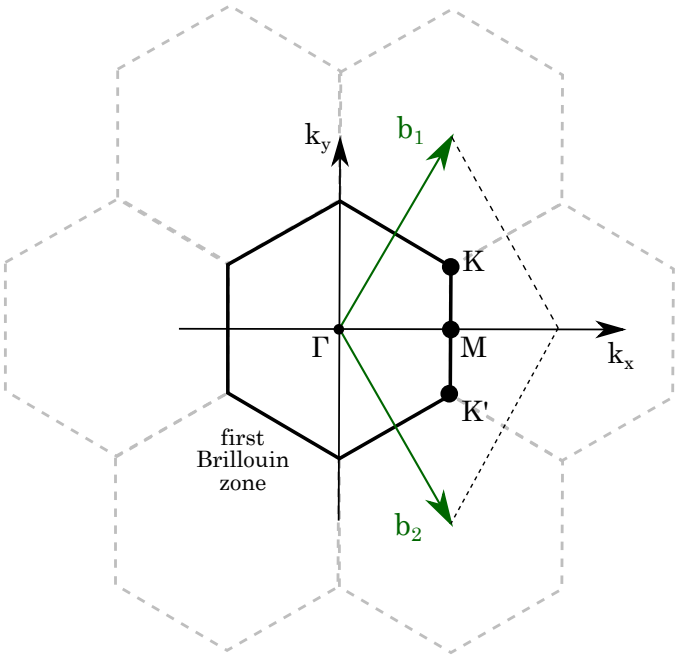

Figure 1.3: Reciprocal lattice with high symmetry points and reciprocal lattice vectors $\vec{b_1}$ $\vec{b_2}$, first Brillouin zone is marked in black [3].

Graphene is also the building block of different carbon allotrope: it can be stacked into three-dimensional graphite, rolled into one-dimensional nanotubes, or wrapped into zero-dimensional fullerenes like shown in Figure 1.4.

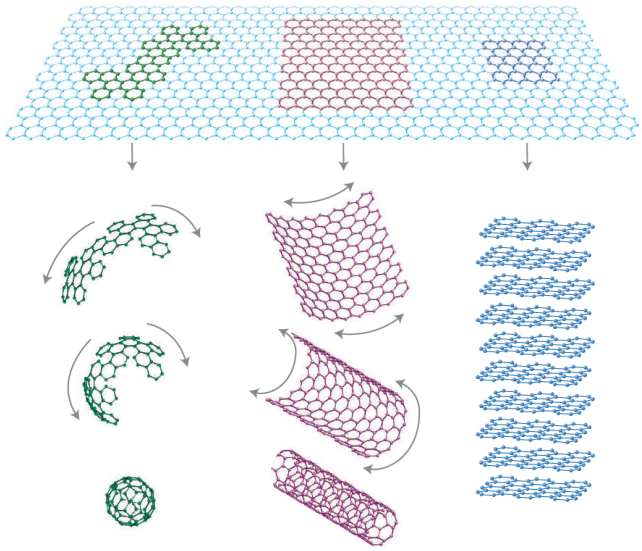

Figure 1.4: Graphical representation of different carbon allotrope. Graphene is the 2D building material for fullerenes, nanotubes and graphite [4].

1.2 Electronic properties

Conduction properties of graphene can be derived by analysing the energy band of its structure. Let's now consider only π-bonds which are responsible of energy band next to the Fermi level (the one involved in current flow). σ-bonds are responsible for energy states far from Fermi level, their investigation is more useful to give a deeper understanding of the mechanical properties. Since the graphene unit cell contains two identical carbon atoms (A and B), the energy band structure originating by π-orbitals has two energy bands: a *valence band* which is completely filled with electrons and a *conduction band* which is empty. The energy band structure of graphene in the first Brillouin zone and the dispersion relation at one symmetry point is represented in Figure 1.5.

The valence band and the conductance band are connected together at the so called Dirac points (K and K') which are the vertices of the reciprocal lattice hexagon. Graphene behaves like a semiconductor with zero energy gap, inversion of charge carriers between electrons and holes can be obtained by applying a voltage, moreover the dispersion relation next to the Dirac points has a conical shape, instead of the regular parabolic shape encountered in most other materials which has very interesting implications. If we name k the momentum of a single electron, and we consider the electron energy as only kinetic, the dispersion relation can be written as follow:

$$E(k) = \frac{\hbar^2 k^2}{2m^*} \tag{1.1}$$

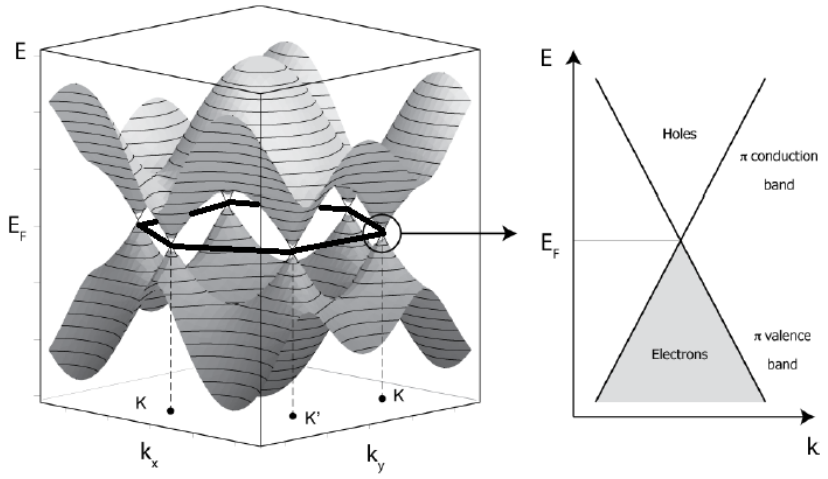

Figure 1.5: Energy band structure of graphene in the first Brillouin zone and dispersion relation at one symmetry point.

where $\hbar$ is the reduced Plank constant and m^* is the effective mass. Effective mass is not the electron mass $m_0 = 9,11 \cdot 10^{-31}$ kg, it is a parameter that helps us to describe the interactions between electrons and the crystalline lattice. The dependence of the energy on the square of the momentum is typical for all the metals and semiconductors, and it is the indication that the Schrödinger equation is appropriate to describe the physics of these systems at low energies. It is interesting to observe that the curvature of the $E(k)$ relation is proportional to the effective mass of the electron:

$$\frac{\partial^2 E}{\partial k^2} = \frac{1}{m^*} \tag{1.2}$$

The bigger is the dispersion relation curvature, the bigger is the electron effective mass, the lower is the mobility. In graphene, close to Dirac points, the equation describing the low-energy physics is not the Schrödinger equation but the massless Dirac equation in two-dimensions, so the relation between energy and momentum is linear and linear dispersion relation has no curvature, so for equation 1.2 leading to a null effective mass and infinite mobility. Dispersion relation in graphene can be expressed as:

$$E(k) = \pm \hbar v_F k \tag{1.3}$$

where v_F is the Fermi velocity that is $c/300$ with c the speed of light. This means that in pristine graphene, the mobility can reach values up to 10^5 cm^2/Vs at room temperature and so graphene has a theoretical resistivity as low as 10^{-18} Ωcm, such low resistivity values determine very high current densities. Good thermal conductivity instead is due to the phonon conduction that dominates the long-scale heat transport in graphene. Finally it should be pointed out that since electrons in graphene behaves like massless Dirac electrons, graphene offers the possibility of studying relativistic effects. This particular behaviour is still valid in the case of bilayer graphene, where the band-gap is still equal

to zero but it is possible to open up a bandgap when stacked specific ways. For three or more layers (few layers) the electronic structure evolves rapidly and approaches the 3D limit of graphite at 10 layers. Therefore, the term graphene is usually used to denote a single layer [5]. A few layers of graphene (FLG) is usually adopted to indicate up to 10 layer, whereas multi-layer graphene (MLG) refers 10+ layers [6].

1.3 Mechanical and optical properties

Thanks to the strong σ-bonds (615 kJ/mol), stronger than the C-C bonds in diamond (345 kJ/mol) graphene has extremely large stiffness, the Young modulus of graphene has been shown to be $E = 1,0$ TPa [7] which make it one of the strongest material ever measured. Furthermore, the material is chemically stable and almost impermeable to gases. Another noticeable property of graphene is its transparency to light. The theoretical transmissivity (percentage of light that passes trough the material) is given by the relation:

$$T = 1 - \pi\alpha \approx 97.7\% \tag{1.4}$$

with $\alpha = e^2/\hbar c$ that is a constant with no dependency on the material. This formula could be applied for multiple graphene layers. [5]

Thanks to these properties graphene is an ideal material for nano-electronics, especially for high-frequency applications. Furthermore, its optical and mechanical properties are ideal for micro and nano-mechanical systems, thin-film transistors (although the lack of a bandgap is a serious issue here), transparent and conductive composites and electrodes, flexible and printable (opto)electronics, photonics and bio-compatible electronics.

1.4 Production processes

Graphene can be produced in laboratory through different chemicals and physical processes. The most commons are represented in Figure 1.6. We will briefly describe each of these techniques that has different costs and results, with a final focus on chemical vapour deposition or CVD that is the most promising technique for industrial production and is the method we will use to produce our substrate.

Mechanical exfoliation

Mechanical exfoliation (ME) is the technique that allowed Geim and Novoselov to isolate the graphene for the first time. It consists in using a Scotch® tape to mechanically peel a graphite flake. By applying this process several times the small interaction force between graphite planes will be broken and the final result will be a mono-atomic layer of carbon atoms. This process is really simple to be done but it give us very unpredictable results. The final result depend by several parameters that cannot be controlled easily. The number of peeling steps cannot be defined a priori and the process is not scalable and so it is not suitable for industrial production. Moreover an additional step is usually required to remove graphene from Scotch® tape and placing it to a target substrate, generally SiO_2. Acetone or isopropyl alcohol (IPA) are generally used to remove glue residues.

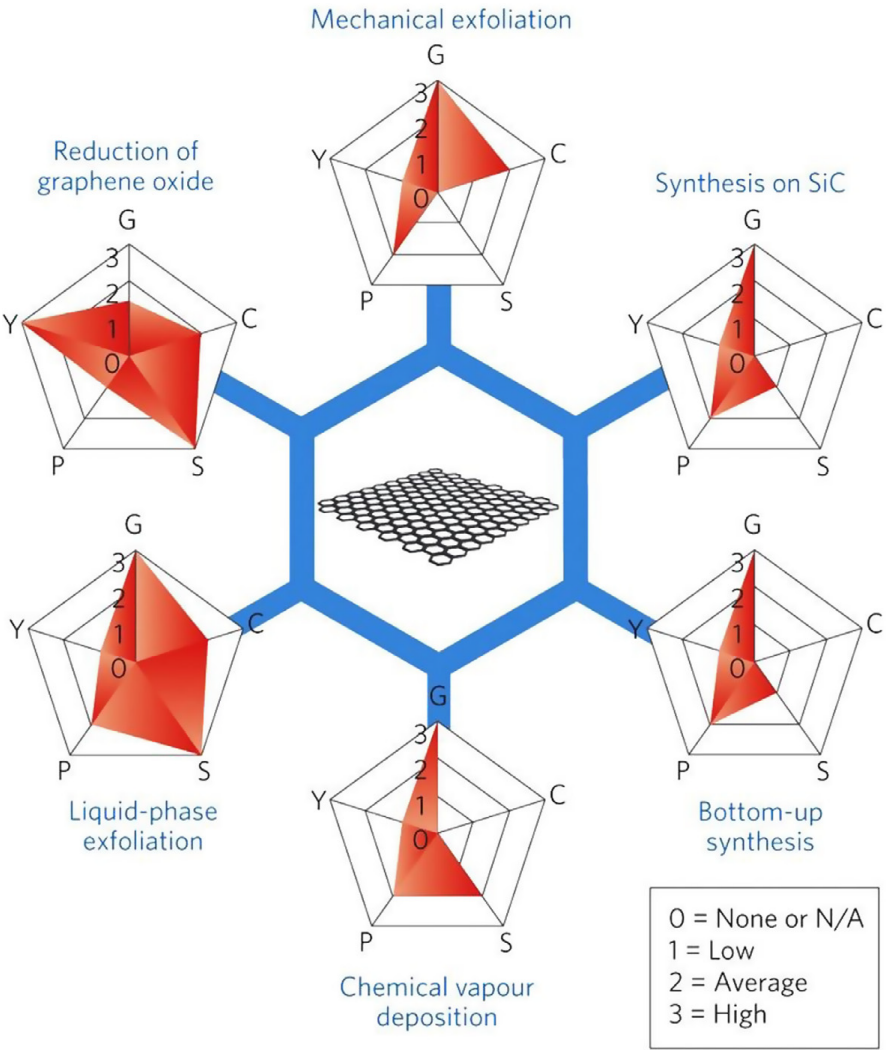

Figure 1.6: Characteristics of most common graphene production methods: (G) refers to graphene quality, (C) refers to the production cost, (S) refers scalability, (P) refers to purity and (Y) refers to the yield [8]

Liquid phase exfoliation

Liquid phase exfoliation or LPE is a popular method for graphene production and it consists in three steps:

1. dispersion in a solvent or surfactant
2. exfoliation
3. purification

A graphite powder is submerged and dispersed in a solvent, usually NMP (N-methyl-2-pyrrolidone), and sonicated. The liquid solvent penetrate between graphite planes and thanks to sonication separate them. The concentration of graphene flakes in the solution is linearly proportional to the sonication time. Thanks to a further centrifugation step the flakes can be separated by their thickness so graphene can be separated by residual graphite. Finally the solution is purified. This technique is very suitable for industrial production but it doesn't produce good quality graphene samples, the process yield can be tuned by parameters like the initial graphite concentration, the sonication time and the centrifuge speed but the high reactive solvents increase a lot the production costs while the process is not eco-friendly [8].

Electrochemical exfoliation

This technique uses a liquid solution (electrolyte) and an electric current. A graphite electrode (anode) is submersed in the electrolyte and oxidized by an electric current. The resulting anodic material is composed by several graphene layer, has a low yield and it's more similar to graphene oxide in terms of its oxidation state instead of pristine graphene. This process is widely used to produce conductive FLG for energy and optical applications and the main tuning parameters are the graphite source and the intercalation-exfoliation conditions given by electrolyte, time and current. This technique if compared with LPE it has the advantage of requiring only one step and it doesn't use any expansive and toxic solvent. [2, 8]

Chemical reduction of reduced graphene oxide

The chemical reduction of reduced graphene oxide (rGO) consists in the exfoliation of graphene oxide (GO) in single layer of GO sheets and then reducing them in graphene-like sheets. The produced sheets has not a very good quality due to their edges and oxygen residuals, it could be argued if it is proper to call them graphene. This process is strongly affected by the choice of the solvent, the reducing agent and the surfactant that are critical to maintain the graphene-like flakes stable in the suspension and reach high yield. [8]

Epitaxial growth

Epitaxy comes from the Greek words epi (upon) and taxis (ordered). Epitaxial growth refers to the growth of a monocrystalline layer of graphene with the same crystal orientation of the substrate. The raw material usually used for epitaxial growth of graphene

is silicon carbide (SiC) over a silicon substrate. A SiC crystal is placed in a vacum chamber and heated up to 1300 °C. At this temperature and pressure conditions, the silicon sublimates and the carbon atoms re-arrange themselves on the surface forming a single layer of graphene. The quality of the final material is very good but the process is very expansive in terms of energy. Moreover it is impossible to detach the graphene layer from the substrate that change its properties, so it is difficult to integrate it in electronics devices. [9]

1.4.1 Chemical vapour deposition

Chemical vapour deposition or CVD is a physical deposition mechanism widely used especially in industry for graphene production. This process involves a carbon based gas, a reaction chamber and a metal that acts as a catalyst. The CVD deposition system is described in Figure 1.7 and it includes a reaction chamber with a controlled low pressure argon atmosphere, an heating element and a mass flow controllers (MFC) to dispense gas inside the chamber. Several carbon based gases can be used but the most common are methane (CH_4) and ethylene (C_2H_4), in our deposition we used methane.

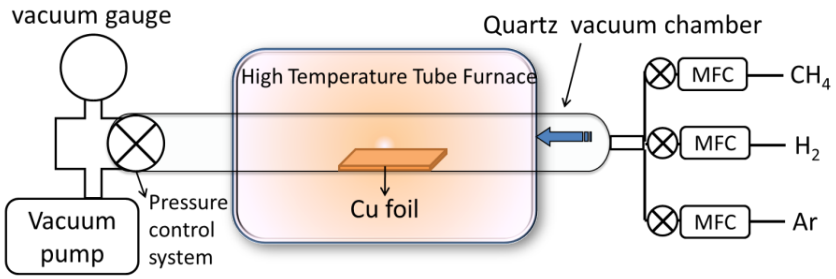

Figure 1.7: CVD reaction chamber and apparatus [10]

Growth mechanism

When the gas is introduced inside the chamber it decomposes due to the high temperature on the catalyst substrate. Carbon atoms split from hydrogen and the light hydrogen gas is removed from the chamber while the heavier carbon fall on the metal catalyst.

$$CH_4\,(\text{gas}) \xrightarrow[\text{catalyst}]{} C\,(\text{solid}) + 2\,H_2\,(\text{gas})$$

The mechanism that lead to graphene formation are different for every metal catalyst, the processes that dominate this growth are two: *dissolution and segregation* and *surface adsorption*, they could also happen concurrently [11, 12].

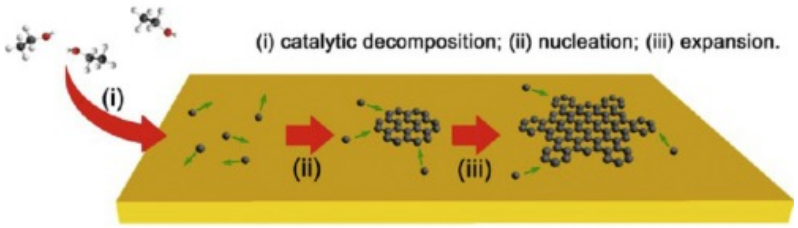

Figure 1.8: Representation of the three steps CVD graphene growth mechanism [11]

The growth of graphene layers on metal catalyst can be controlled by the following parameters:

- **Chamber temperature:** this parameter define the amount of energy involved in the growth process, generally the more is the energy the better is the result in terms of crystallinity of the final layer. In this case the maximum temperature is limited by the furnace and the melting temperature of the metal catalyst. This temperature is generally chosen between 900 and 1200 °C.
- **Gas species and amount/time:** by tuning gas flow rate and time, we can control the speed and amount of carbon injected in the reaction chamber. If the amount of carbon is not enough we don't have segregation whereas if the amount of carbon is too much we grow graphite instead of graphene.
- **Metal catalyst:** as previously said, different metals has different carbon solubility and melting point, the metal choice influence all the other parameters. In the following section we will focus on the influence of different metal catalyst in the process.
- **Cooling time:** during the cooling phase the carbon atoms segregate on the surface of the metal catalyst, so controlling the cooling time and rate we can control the amount of segregated carbon and so the number of graphene layers [13, 14]. This phenomenon is depicted in Figure 1.10.

A general growth process usually consists in these steps:

- Chamber heat up
- Metal annealing
- Carbon gas introduction
- Cooling down

Metal catalysts

Transition metals are usually involved in the graphene synthesis. A metal catalyst is annealed in an hydrogen/argon atmosphere before the injection of the hydrocarbon gas, this improve graphene formation and increase quality. Hydrogen help to reduce the native surface oxide layer that may have formed on the surface of the metal and the high temperature increase the metal grain size, so the number of metal grain boundaries is reduced. Zhang et al. [15] revealed that graphene growth in CVD is not uniform if the catalyst is not monocrystalline. They found that the preferential formation of monolayer/bilayer graphene on the single crystal nickel (Ni) surface is attributed to its atomically smooth surface and the absence of grain boundaries. In contrast, CVD graphene formed on polycrystalline Ni leads to higher percentage of multilayer graphene, which is attributed to the presence of grain boundaries in Ni that can serve as nucleation sites for multilayer growth. This is represented in Figure 1.9.

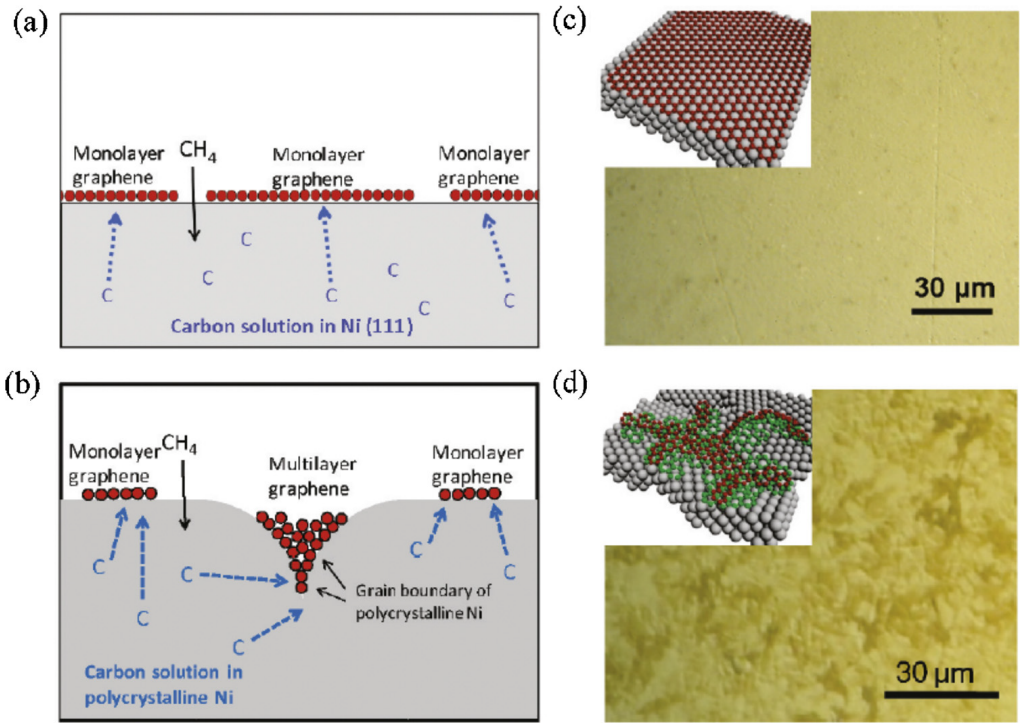

Figure 1.9: Schematic diagrams of graphene growth mechanism on Ni (111) and polycrystalline Ni surface, respectively. (c and d) show the Optical image of graphene growing on Ni (111) and polycrystalline Ni surfaces after the CVD process. [15]

CVD graphene was reported first in 2008 and 2009 by Yu et al. and Li et al. using rispectively Ni and Cu as substrates. They shown that for Ni the growth mechanism is *dissolution and segregation* (Figure 1.10), while for Cu the growth mechanism is *surface adsorption*, the carbon atoms doesn't dissolve into the metal but remain on its surface making this process self-limiting. Li et al. addresses the different behaviour of the two metals during growth process to their different carbon solubility [14, 16]. In Table 1.1

carbon solubility for the considered metals is reported.

Metal	Carbon solubility @1000°C (wt%)
Copper (Cu)	0.004
Nickel (Ni)	0.28
Molybdenum (Mo)	0.0026

Table 1.1: Carbon solubility on typical metals for CVD graphene [13]

In 2012 Wu et al. deposited large-area graphene on molybdenum foils by chemical vapour deposition. Carbon has a solubility in Mo (see Table 1.1) that is even lower than Cu. They expected that the ultra-low C solubility in bulk Mo could lead to an even more self-limiting growth of graphene films. They found that the graphene thickness can be controlled by the cooling rate, this suggest that the growth mechanism is more similar to the one that happen in Ni that to the one in Cu. So they conclude that the main mechanism that allow graphene growth on Cu shouldn't be addressed to the lower solubility of carbon in Cu but to the lower affinity of carbon and Cu [13].

Successively also Wang et al. in 2013 proved that molybdenum is a very good catalyst and the growth mechanism of graphene is a combination of *dissolution and segregation* and *surface adsorption* [17].

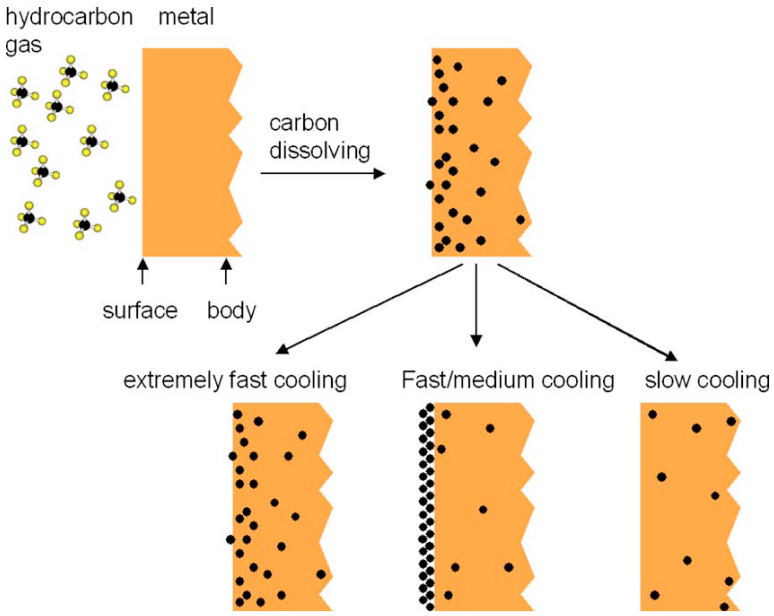

Figure 1.10: Illustration of carbon segregation at metal surface in the dissolution and segregation process [14]

Metal catalysts influence on graphene quality mainly depend on its:

- **grains shape and size:** as highlighted by [15] and [13] metal grains has impact on the crystal orientation and graphene thickness, generally graphene has different crystallographic orientation on different grains.
- **thermal expansion coefficients:** thermal stress due to differences between expansion coefficient of metal and the substrate can lead to wrinkle formation [2].

In order to exploit the different properties of different metals, alloys has been also exploited as catalyst (e.g. Cu-Ni alloys) [11] but they are more expensive to be realized and more difficult to etch in the following steps. Considering all the aforementioned things, molybdenum (Mo) seems a really promising material for the future of graphene CVD growth. Grachova et al. [18] demonstrates some of its advantages:

- **higher melting point than other metals:** resulting in less thermal stress and encouraging wrinkle-free graphene deposition, moreover its higher melting point resulting in a larger process window (100°C) which is advantageous for a large volume production.
- **similar temperature expansion coefficient to Si:** molybdenum has 4.8 $\cdot 10^{-6}$ 1/K thermal expansion coefficient that is very close to that of Si (2.6 $\cdot 10^{-6}$ 1/K), while Cu is 17 $\frac{um}{m \cdot K}$.
- **cleanroom compatibility:** molybdenum in considered a CMOS compatible metal so it is compatible with cleanroom processes. This allow us to integrate the graphene growth as a standard step during the device fabrication in cleanroom.
- **Transfer-free process:** Vollebregt et al. [19] demonstrated in 2016 that the transfer of graphene from molybdenum to a SiO_2 substrate can be easily made without requiring any special materials and can be easily integrated in a batch fabrication. Etch of molybdenum can be easily done with H_2O_2.

Grachova et al. [18] grown graphene with an AIXTRON Black Magic Pro system at 25 mbar, using the same recipe on 500 nm Cu and 50 nm Mo sputtered on a 10 mm wafer with 100nm thermal oxide on top. In Figure 1.11 a SEM image of the two materials highlight the difference in grains and roughness, this is also confirmed by the AFM analysis reported in Figure 1.12. The average roughness for Cu is 118 nm whereas for Mo is 35 nm.

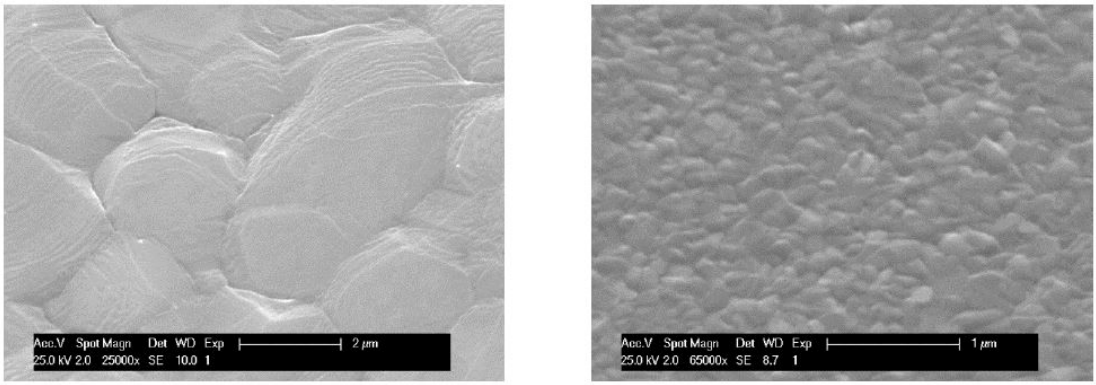

Figure 1.11: SEM images of the Cu (left) and Mo (right) film after graphene growth [18]

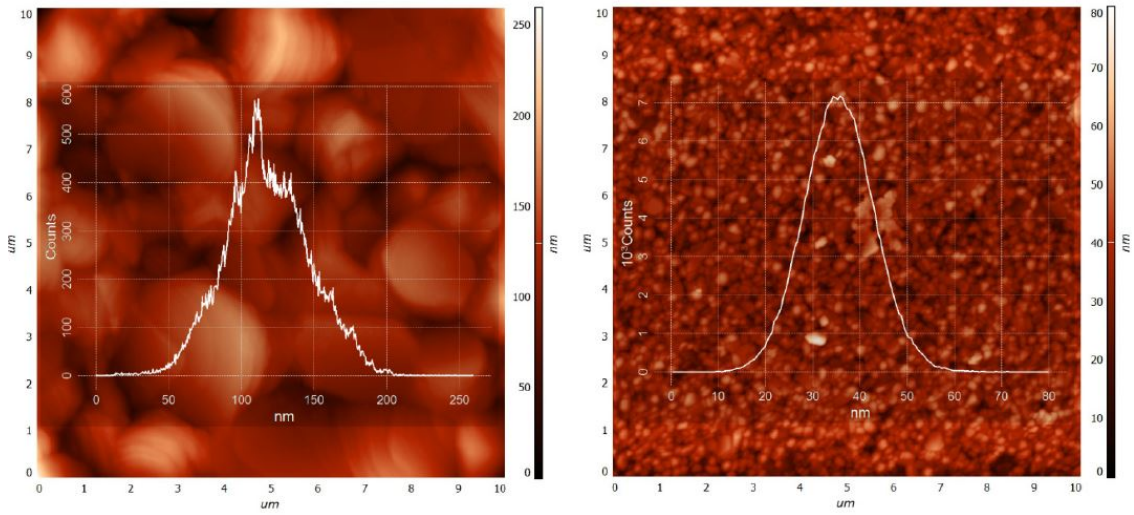

Figure 1.12: AFM images of Cu (left) and Mo (right) after graphene growth. Insets: histograms displaying surface roughness in nm [18]

In 2019 Ricciardella et al. [20] demonstrated the growth of MLG on top of the Mo catalyst with a-C both below and above the Mo layer, eliminating the need for a gaseous carbon precursor. They found that the highest quality of MLG, proved through Raman spectroscopy was obtained with a 20 nm-thick Mo layer deposited on a 500 nm-thick a-C film. They also found that the quality is at least as good as that obtained in conventional CVD with gaseous hydrocarbon sources. A scheme of the experiment is represented in Figure 1.13.

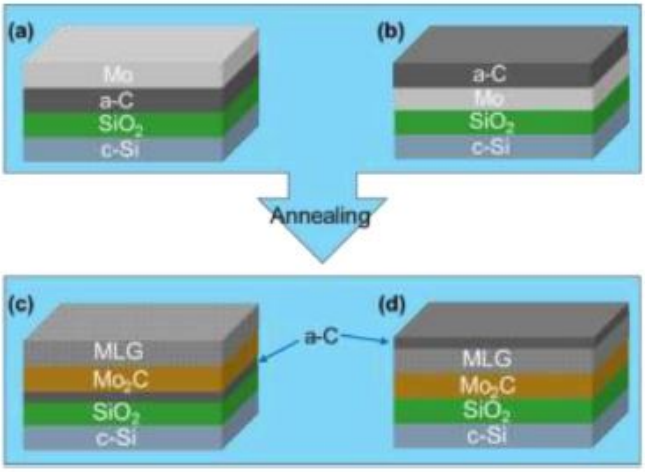

Figure 1.13: Schematics of layer stacks before (a) and (b) and after synthesis process (c) and (d) [20]

Transfer-free process

After graphene growth using CVD, the thin carbon layer needs to be moved from the metal to an insulating substrate in order to exploit its conductive properties. The common method is generally made by using a sacrificial support material. A thin layer of polymer (generally poly methyl metacrylate or PMMA) is spin coated on the graphene, then the metal catalyst is etched. The PMMA acts as a support for the thin layer of graphene and avoids folding. The graphene + PMMA is then placed on the insulating support material and after a baking the PMMA is removed. This process in not trivial and it can compromise the graphene quality. In the recent years several technique like the one developed by Dong et al. [21] has been designed to minimize the complexity of the transfer process. In 2016 Vollebregt et al. [19] develop a *transfer-free process* using molybdenum as metal catalyst. In this process no support material is needed, the metal is patterned before the graphene growth. After the growth the metal is etched using hydrogen peroxide and the graphene gently deposit on the insulating substrate. This technique has also been recently proved successfully on an entire wafer [22].

Vollebregt et al. sputtered 3N5 pure Mo on 90 nm SiO2 layer, and they found that Mo film can be made as thin as 25 nm without the metal film segregating at the graphene CVD temperature in contrast with [17] that found de-wetting in molybdenum films thinner than 100 nm. SF_6 gas was used to dry etch Mo pattern with resist mask before graphene growth. When the MLG is grown in this condition it forms a small bonding with the silicon oxide under the metal. This bonding is stronger enough to keep the graphene attached to the substrate while the metal is etched, so in the last step it will fall on the substrate. The process is depicted in Figure 1.14.

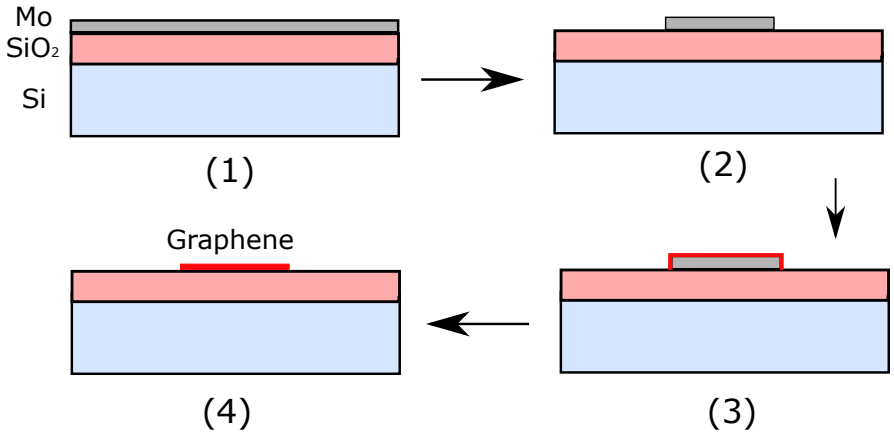

Figure 1.14: Transfer-free process

1.5 Graphene characterization

In order to characterize the grown graphene we used the following tools:

- Raman Spectroscopy
- Ultraviolet-visible spectroscopy (UV/Vis)
- Scanning Electron Microscope (SEM)
- Atomic Force Microscopy (AFM)

Here is a brief explanation of each characterization technique we used, the results of this characterization are reported in the experimental results section.

1.5.1 Raman spectroscopy

Raman spectroscopy applied to graphene is a technique used to determine the number and orientation of layers, the quality and types of edge, and the effects of perturbations of graphene. Raman is the ideal characterization tool for graphene because it is non-destructive, offer high resolution, give both structural and electronic information and can be applicable at both laboratory and mass-production [23].

This molecular spectroscopy technique is based on the scattering of an electromagnetic radiation by atoms and molecules. Light has a certain probability of being adsorbed scattered by a material. Photons can be scattered following two different phenomenons:

1. **Rayleigh scattering:** the majority are scattered elastically such that the scattered photons have the same energy (frequency, wavelength and colour) as the incident photons but different direction.
2. **Raman scattering:** a small amount of this photons is scattered at a lower en-

ergy (Stokes scattering) or at a higher energy (anti-Stokes scattering) due to an interaction with the sample. The energy difference between the incident and the inelastically scattered photons corresponds to the vibrational energy levels of the diffusing molecule in the sample. When a particle loses a unit of vibrational energy (phonon), it is said to have passed to a lower state of vibrational energy.

Raman spectrum contains information about both atomic structure and electronic properties. The spectra of carbon-based materials show characteristic peaks. By analysing the shapes, the intensities and the position of these peaks we can obtain a considerable amount of information. Peaks are indicated with a letter and each peak is characterized by a certain: intensity (I), area (A), position and FWHM (full-width at half-maximum). The most relevant peaks in a graphene Raman spectrum are:

- **D peak:** it is due to the breathing mode of the six-atoms (sp^2) ring, it requires defects for its activation, it measure disorder (number of defects), its intensity is directly proportional to density of defects. It is usually positioned around 1350 cm^{-1}.
- **G peak:** it is generated from the bond stretching of all pairs of sp^2 atoms in both rings and chains and thus is always present in any sp^2 carbon spectrum. It usually appears around 1587 cm^{-1}.
- **2D peak:** overtone of D peak, originated by a double phonon scattering and doesn't require a defect.

An important Figure of merit we can obtain from Raman analysis is the ratio between peaks intensity, in particular:

- **I(D)/I(G):** proportional to the amount of structural defects.
- **I(2D)/I(G):** if graphene has less than five layers, it is inversely proportional to the number of graphene layers, than it levels off.

FWHM(D) is a good indicator of disorder. It always increases with increasing disorder and is sensitive to all types of defects while FWHM(2D) is a good indicator of the number of layer. The information about peaks are very good Figure of merit, useful to compare different samples and to evaluate the amount of defects on the sample. In Figure 1.15 the difference between a defect free and a defective layer graphene Raman spectra is shown. The more defects presents the layer, the higher is the D peak.

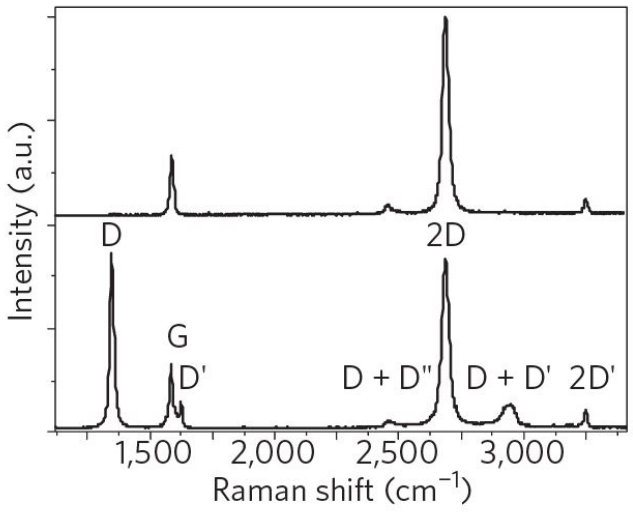

Figure 1.15: Comparison between Raman spectrum of defect-free graphene (top spectrum) and defective graphene (bottom spectrum) [23]

Raman spectroscopy has also been extensively used by [13] and [24] to evaluate the graphene thickness and quality for different gas flows and time parameters.

1.5.2 Scanning Electron Microscopy

Scanning Electron Microscopy (SEM) is a microscopy technique that uses electron beam and electromagnetic coils instead of a light source and optical lenses. In microscopy the resolution is defined as the minimum distances by which two structures can be separated and still appear as two distinct objects. Resolution in a perfect optical system can be described by Abbe's equation that is:

$$d = \frac{0.612\lambda}{\text{NA}} \tag{1.5}$$

where λ is the wavelength of the imaging radiation and NA is the numerical aperture that depends on the aperture of the system and by the refraction index of the medium between point source and lens. Electrons could be modelled as wave and they result to have a very small λ, so exploiting electrons as radiation source, SEM allows high-resolution images of surface topology at micro/nano-scale exploiting the smaller wavelength of electrons if compared to visible light [25].

The electron beam is focused and scanned across the surface of the sample. Thanks to the interactions between electrons and substrate we can obtain useful information, the scattered electrons can be classified according to their properties like shown in Figure 1.16. The more relevant are:

1. **Backscattered electron:** they are the result of an elastic collision, usually they are scattered with an angle of more than 90° and since their energy is relatively

high they are good to process the image. Since they come from elastic interaction, contains also compositional information, they are useful to identify different kind of materials. The larger is the atomic number of the observed matarial, the highter is the amount of backscattered electrons.

2. **Secondary electrons:** they are the result of the inelastic scattering that occurs during interaction. The lost of energy in the bump cause the excitation of the substrate electrons during the bombardment. Due to their energy interaction with the substrate secondary electrons have a lower energy (<50 eV) but they contain information the surface of the sample.

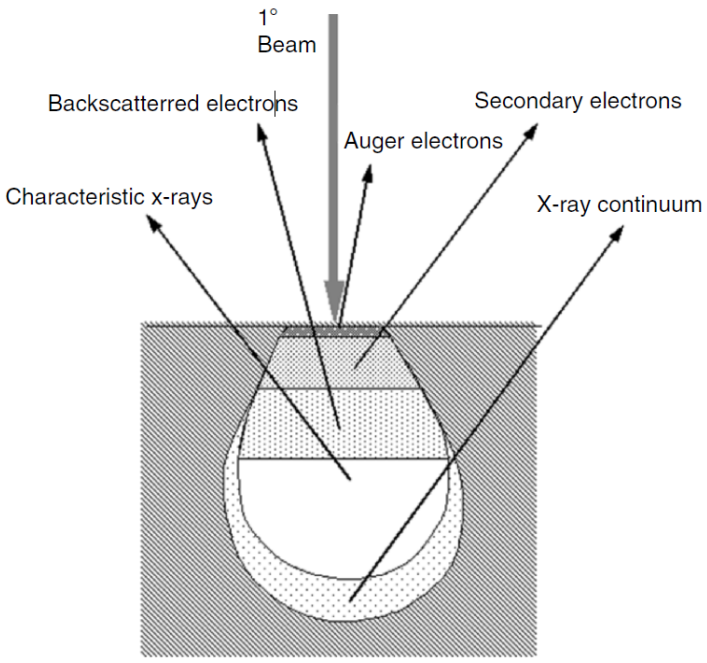

Figure 1.16: Different types of signal generated from the interaction between the incident beam and the substrate. [25]

1.5.3 Atomic Force Microscopy

Atomic Force Microscopy (AFM) is a characterization technique that uses a probing tip located at the end of a spring cantilever like shown in Figure 1.17. The tip can be made of different materials that is chosen according to the substrate material. The tip is placed very close to the substrate and scanned across it. The weak signal generated by the atomic interaction of tip and analysed material is registered. The tip is put in resonation by a piezoelectric actuator and is kept at a constant distance from the substrate by a feedback system while scanning.

Depending on the distance between the substrate and the tip the AFM can work in two different modes:

1. **Contact mode:** this mode exploits the shortest distance between the tip and the substrate (from which the name is originated). It uses the repulsive force caused by the superposition of the electronic clouds of tip and substrate atoms.

2. **Non-contact mode:** this mode exploit a bigger distance between substrate and tip if compared with contact mode. When the tip is close to the substrate it is attracted by the Van Der Waals forces.

3. **Tapping mode:** in this mode the cantilever oscillates with an amplitude of 20-200 nm that is much higher than in non-contact mode. This mode is generally used to characterize soft materials like polymers. The tip makes contact with the surface for a very short duration in each oscillation cycle. The tip-sample interaction alters the amplitude and phase of the feedback signal.

The feedback system is needed to keep the distance from tip and substrate within the distance range of the mode. The force interaction between tip and substrate with respect to the distance is represented in Figure 1.18.

AFM is particularly suited for surface topography characterisation of nano-scale materials: high-resolution images can be obtained, with a range of few nm and less than 1 nm of lateral and vertical resolution respectively. Compared to other microscopy techniques no special preparation to make the sample conducting is required, as only molecular interactions are involved. The only disadvantage with respect to the other characterization technique is that it requires expensive instrumentation installed in a vibration-free environment.

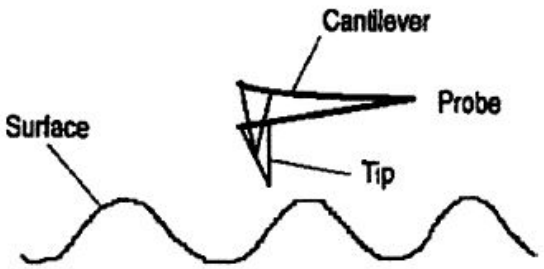

Figure 1.17: Principle of the AFM [26]

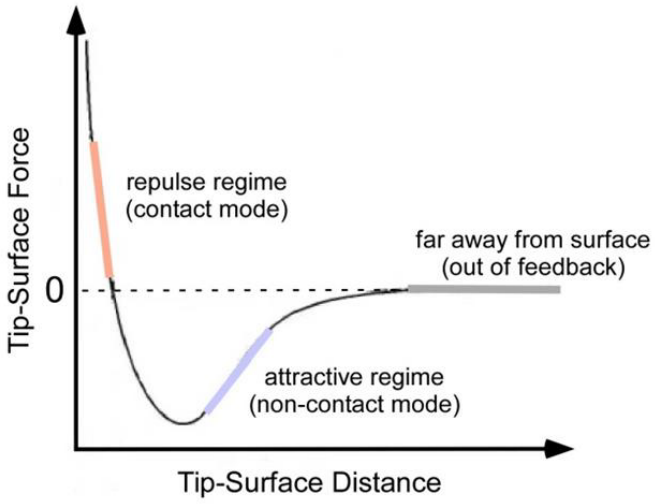

Figure 1.18: Tip surface force vs. tip-substrate distance in AFM [26]

Chapter 2

Gas sensors

Gas sensors has been deeply investigated in the last decade, they are devices that convert the gas volume fraction (ratio of a specific gas volumetric flow with respect to the volumetric flow of all fluids and gases) into a corresponding electrical signal. Gas sensing devices can be divided in two main groups: single gas sensor and array gas sensor. Single gas sensor recognize only one gas species whereas gas sensor array can detect multiple species simultaneously acting as a artificial nose. Depending on the application, this type of sensor can monitor the concentration of the target gas in the environment, and/or indicate that the concentration exceeds a specified threshold. Gas sensors are crucial for: environmental monitoring, industrial chemical processing, public safety, agriculture and medicine.

The working principle of a gas sensor can be explained by its two functions: *recognition* and *transduction*. Recognition consists in the adsorption of the target gas (named analyte) in the sensing element of the device. The process can occur either at the surface or in the bulk. In the first case the process is named adsorption, while in the second case it is named absorption. As a result, certain physical or chemical properties of the sensing material (e.g. resistance, capacitance, work function) vary as a function of the analyte concentration [27]. The transduction process is depicted in Figure 2.1.

The key parameters for measuring a gas sensor performances are:

- **Sensitivity:** it is usually expressed as the ratio of the resistance of the gas sensor in the gas under test to the resistance in normal air (or N_2) and is denoted by: S=R_g/R_a where R_g is the resistance of the gas sensing material at a certain concentration of a target gas, while R_a is the resistance of the sensing material at neutral atmosphere.
- **Selectivity:** it is the ability of a gas sensor to differentiate gas species in the presence of multiple gases.
- **Response time (t_{RES}):** is the time that the sensor needs to chance its resistance to 90% of the final change due to saturation. The shorter is this time, the better is the sensor performance.
- **Recovery time (t_{REC}):** like the response time is the time that the sensor needs

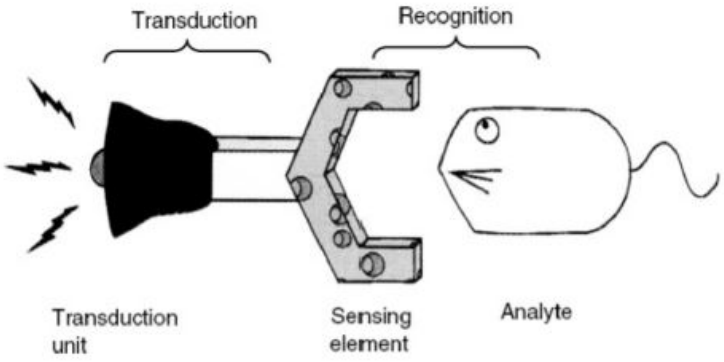

Figure 2.1: Schematic representation of the recognition and transduction functions performed by a gas sensor [27]

to change its resistance to 90% of the original value before the gas exposure. Even in this case: the faster is the recovery time, the better is the sensor performance.

- **Stability:** is the ability of a gas sensor to maintain the same output characteristics over a specified period in which the gas concentration is kept constant.
- **Repeatability:** is the measure of how different test results made in the same test environment are consistent each other.
- **Limit of detection (LOD):** is the minimum gas concentration that the gas sensor is able to reliably detect. This parameter is usually influenced by noise which in turns is influenced by the sensing element.
- **Working temperature:** is the temperature that can gives the gas sensor its highest sensitivity. Adsorption and desorption rates are temperature dependant, so for different temperatures we have different response.

Nowadays semiconductor gas sensors (SGS), known also as chemo-resistive gas sensors, typically based on metal oxides, are the most widely used in the world due to their good sensitivity and fast response. The sensing mechanism of these SGS sensors is attributed to the changes of the electrical charge carrier on a metal oxide surface due to reduction and oxidation chemical reaction with gases. These gas sensors have not a sufficiently high sensitivity for precision measurement and this could be caused by their low surface area that is the total material surface per unit mass. Another disadvantages about SGS is the relatively high working temperature they require, in the range of 200 to 500 °C, which is often a limit in commercial applications [28]. For this reason, in the recent years a variety of new materials are being explored as possible replacement to metal oxides and graphene is attracting intensive attention.

2.1 Graphene gas sensors

Graphene is considered a promising material for gas sensing applications since 2007 when Schedin et al. proved that detection of individual gas molecules was possible [29]. Pristine graphene could be a really good candidate for gas sensing for its:

- large theoretical specific surface area (2630 m^2/g)
- extreme sensitivity up to single molecules, graphene is sensitive to the smallest change in its electronic configuration even at room temperature [30]
- good thermal and electrical conductivity
- low signal-to-noise ratio due to the good quality of the crystal
- high mechanical robustness

Graphene gas sensors can be based on different working principles:

- **Resistive gas sensor:** the resistance of a graphene sheet is measured, and a change in resistance corresponds to gas interaction. The greater is the interaction the greater is the resistance change. These sensors are also called chemo-resistors.
- **FET gas sensors:** graphene is used as channel for a FET transistor, gas interaction with graphene leads to a variation of carriers in the channel, this variation can be detected by measuring I_{DS}.
- **Quality sensitive gas sensors:** the principle of quality sensitive sensor is that the operating frequency of the device changes with the type and concentration of the gas being detected. This effect could be exploited in two different ways: with quartz crystal micro-balance (QCM) or with surface acoustic wave (SAW) sensors.

Among these three types, graphene chemo-resistors are te most common and easy to fabricate sensors. In Figure 2.2 a chemo-resistor structure is represented. A small strip of graphene is fixed between two metallic electrodes.

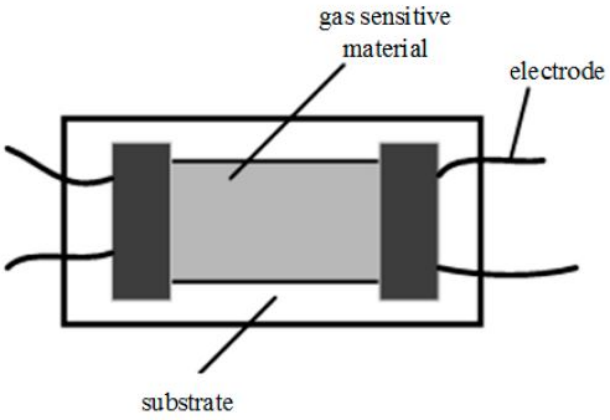

Figure 2.2: Graphene chemo-resistor illustration

In their experiment in 2007, Schedin et al. tested the response of a mechanically exfoliated graphene chemo-resistor to 1 ppm of ammonia (NH_3), carbon monoxide (CO), nitric oxide (NO_x) and water vapour in pure helium or nitrogen at atmospheric pressure. They found that the initial rapid response to gas was followed by a region of saturation, in which the resistivity changed relatively slowly. They attribute this region to redistribution of adsorbed gas molecules. After a near-equilibrium state was reached, they evacuated the container and this led only to small and slow changes, indicating that adsorbed molecules were strongly attached to the graphene devices at room temperature. Nevertheless, they found that the initial undoped state could be recovered by annealing at 150 °C in vacuum. Repetitive exposure–annealing cycles showed no 'poisoning' effects of these chemicals (that is, the devices could be annealed back to their initial state). A short-time ultraviolet illumination offered an alternative to thermal annealing. Figure 2.3 shows that the resistance of graphene increases after exposure to NH_3 and CO. The Hall measurements revealed that electron were transferred to the graphene material as these two gases molecules were adsorbed on the surface of graphene, resulting in reduced conductivity, which increased resistance. The opposite happened after exposing to water vapour and nitrogen dioxide (NO_2) [29]. To explain this doping behaviour we have to take into account that typically graphene acts as a p-type material due to its interaction with the substrate, moisture, and other contaminants from the atmosphere. Furthermore, most metal contacts to carbon materials have the tendency to improve the conductivity of holes with respect to electrons, also turning the material into a p-type like semi-metal. As holes are the majority charge carriers absorbing electrons would actually reduce the majority charge carriers and hence increase the resistance. In case the graphene acts as a n-type material the reverse would happen.

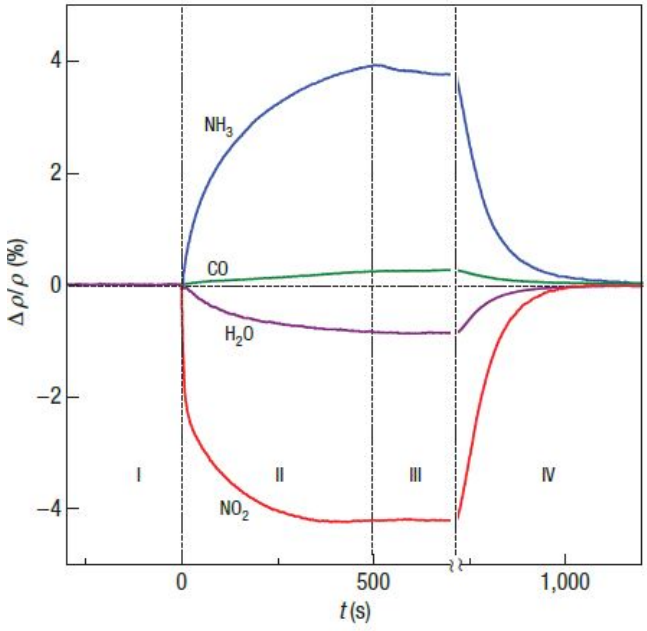

Figure 2.3: Graphene response to gas chemical doping [29]

In 2012, Hwang et al. from Yonsei University studied the response of graphene to NH_3 with different layer number and length-to-width (L/w) ratio. As can be seen in Figure 2.4 they found that different layers of graphene have similar responses to NH_3, indicating that the number of layer has no obvious influence on the sensitivity of gas sensing whereas he found that response intensity changes with the change of L/w. To sum up, the key factor that affects the sensing of NH_3 by graphene is the aspect ratio rather than the number of layers [31].

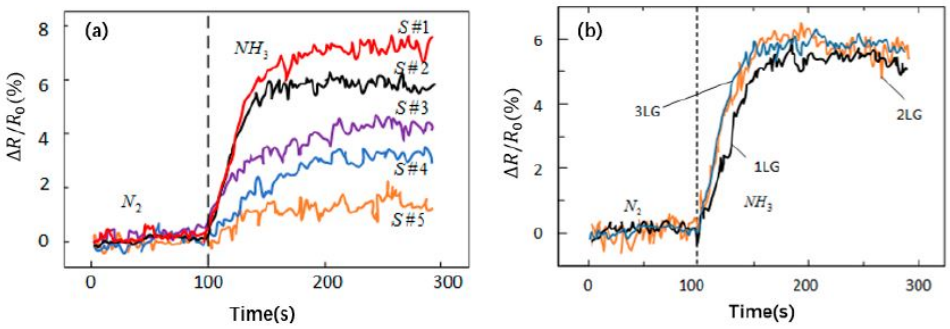

Figure 2.4: Hwang et al. experiment: (a) Comparison of the response of monolayer, double and triple layer graphene to NH3 with a flow rate of 200 mL/min; and (b) The change in response due to L/w ratio and surface area of graphene with NH3 flowing at 200 mL/min [31].

Graphene as previously said has an excellent electron mobility and a large specific surface area which are both really good sensing properties. Pristine graphene is undoped, but interaction with the substrate, residues from the transfer and moisture from the air cause p-type doping. When gas molecules are adsorbed by graphene they couple with electron on the surface resulting in a Fermi level shift. If the valence band (VB) of the adsorbed gas is higher than the Fermi surface of graphene, the gas molecule act as donor for electrons; whereas if the VB of the gas is lower than the Fermi surface of graphene, the gas molecule act as acceptor. [32]

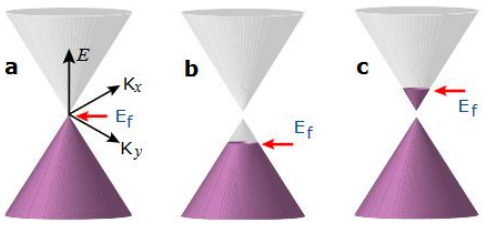

Figure 2.5: Schematic band structures of graphene. (a) Band structure of pristine graphene with zero band gap. Band structures of (b)p-type and (c)n-type graphene with the band gap [33]

2.1.1 Graphene gas sensing mechanism and defects

When the analyte (in our case the gas) interact with graphene it can react with it chemically or physically. The two processes can be described as:

- **Physisorption:** physical interaction between the analyte and substrate due to weak dipole and Van der Waals interactions. This kind of interaction happen in shorter time than chemisorption.
- **Chemisorption:** chemical bond is formed between the analyte and graphene. This interaction require longer time.

In general the energy involved in the two cases is quite different. As a result, the adsorption time is different, making the two processes distinguishable.

In 2015 Lee et al. found that the amount of defects on graphene influence the gas sensing properties. They intentionally induced defects on graphene using oxygen plasma reactive ion etching (RIE) in order to understand the mechanism governing the sensing of gas molecules in defective graphene. The Raman spectroscopy proved that the ion bombardment creates defects on the graphene, the greater is the bombardment the more defects are in the graphene. They found that sensitivity of different gases exhibited a similar tendency toward the defect density regardless of the type of gas. Moreover they found that sensitivity doesn't increase indefinitely with the density of defects, the decrease of sensitivity after a certain amount of damages can be attributed to the extremely low carrier mobility due to defects. The response curves are represented in Figure 2.6. They also found that the presence of defects increased the contribution of slow response, suggesting that defects in graphene concur to the chemisorption. They also made some ab-initio simulations that confirm the experimental results [34].

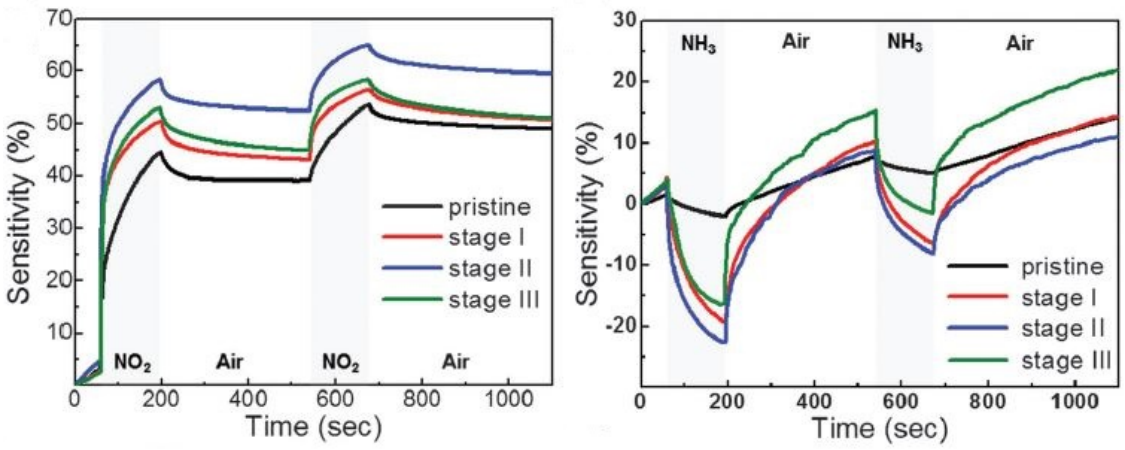

Figure 2.6: Sensor responses for NO_2 and NH_3 [34]

In 2019 Mastrapa et al. tested CVD graphene gas sensing performance inducing defects with air plasma. They found an increase of sensitivity with the increase of density defects without limit. They also found that total recovery of the sensor was not achieved,

meaning that full desorption might require further treatment. However, no clear relation has been found between recovery time and plasma exposure times, this could suggest that the energy needed for desorption is not related to the amount of gas that interact with graphene but only on its chemical structure. If this hypotheses is correct this means that increasing the density of defects we can increase sensitivity without affecting recovery time [35].

In 2017 Ricciardella et al. after demonstrating the effectiveness of CVD graphene as gas sensor [36], even if grown at low temperature to save energy [37]. They investigated the morphology of graphene obtained by three different production processes: ME, CVD and LPE. Both SEM and AFM analyses (Figure 2.8) attest that ME-Gr presents a flat surface having continuous flakes with a mean lateral size in the range of a few tens of microns, whereas CVD-Gr and LPE-Gr are mostly composed of flakes with a mean lateral size around one order of magnitude lower. In both CVD-Gr and LPE-Gr, the rise of these defects is intrinsically associated with the synthesizing routes, for example CVD-Gr replicates the catalyst structure as explained in the previous chapter. In Figure 2.7 the different sensor responses to NO_2 are represented. LPE-Gr show no recovery, ME-Gr has a good recovery whereas CVD-Gr has an intermediate behaviour. These outstanding results denote the first significant proof of concept that the graphene structure can affect the sensing properties. The slopes of current response are also different, ME-Gr has the fastest response whereas LPE-Gr has the slowest. The diverse regimes and slopes in the response curves during the exposure towards NO_2 are due to different interaction mechanisms between the sensing layer and the gas molecules. In particular, fast responses, corresponding to steeper lines, are mainly attributed to sites with low binding energy, such as the sp_2-carbon localized on the plane. On the other hand, binding sites having high-energy, such as defects, are responsible for slow responses. ME-Gr is better for gas sensing, but even CVD-Gr is a good candidate especially for the large scale production it can achieve. It make sense to make more studies on CVD graphene defects [38].

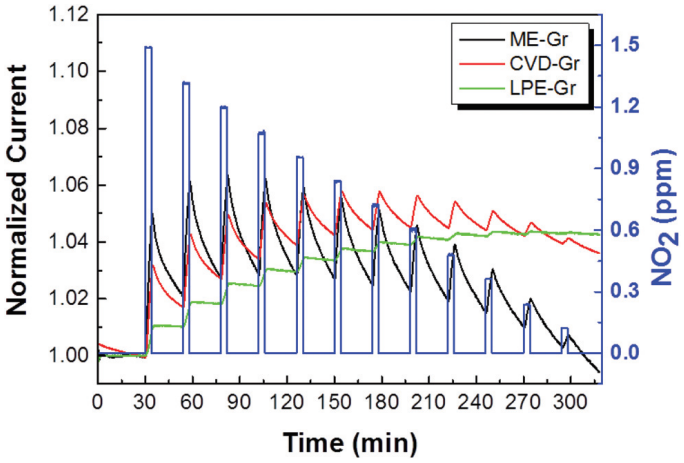

Figure 2.7: Real-time current behaviour of ME-Gr (black line), CVD-Gr (red line) and LPE-Gr (green line) based chemo-resistors upon exposure to sequential NO2 pulses (blue rectangles) at decreasing concentrations from 1.5 down to 0.12 ppm. [38]

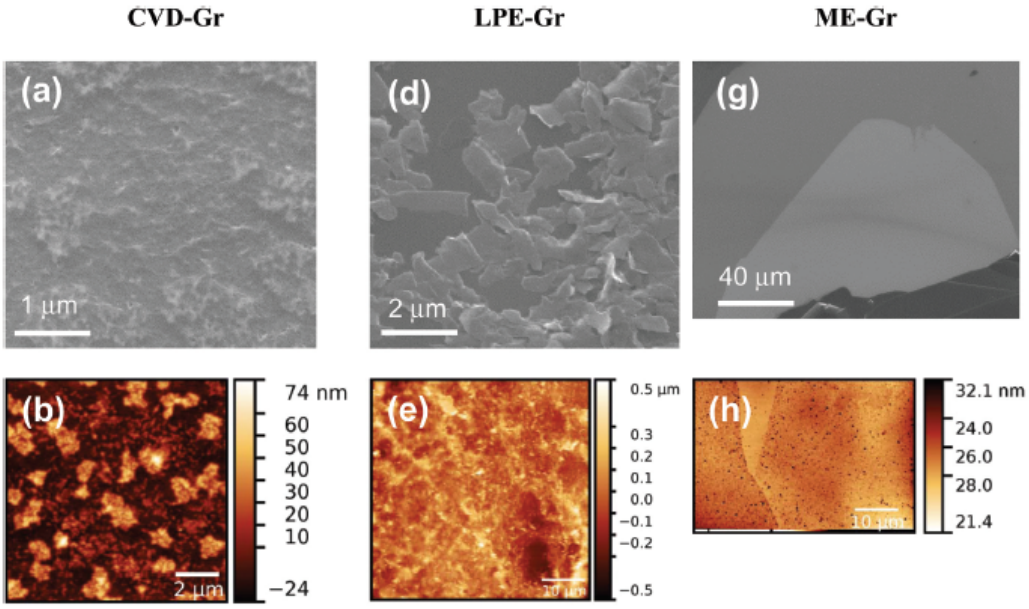

Figure 2.8: SEM and AFM images of CVD-Gr (panels a–c), LPE-Gr (panels d–f) and ME-Gr (panels g–i). The last two rows show the topography and the phase of the samples, respectively. The scale bar of the SEM images proves that the mean lateral size of ME-Gr flakes is around one order of magnitude higher compared to the LPE-Gr and CVD-Gr one [38]

In conclusion, graphene could be a good sensing material for gases, it can be easily produced in large scale using CVD and transfer free process [19]. Moreover defects on graphene that are caused by the CVD growth seems to not influence sensing performance in bad way. Some drawback still remains before making graphene the state of the art for gas sensing: the need of an external energy source for a complete recovery and the scarce selectivity between different gases. The first problem could be solved by placing a micro-heater under the sensor or by illuminating it with UV light whereas the second problem could be solved by functionalizing graphene with other materials. Introducing new elements on the graphene surface and tuning the density of defects seems a good way to improve sensitivity towards a particular species of gas and decrease or even prevent affinity towards others [30]. For this reason in the next chapter we will investigate the effect of functionalizing graphene.

2.1.2 Functionalized graphene

The introduction of dopants on graphene surface to enhance the graphene/molecule interaction for sensing purposes seems to be one of the most promising method to achieve higher sensitivity and selectivity. Faster response and recovery, which are the ability of the sensor to react upon the gas interaction and to return to the initial condition after the end of exposure, could also be obtained. Graphene doping was extensively studied in the past in order to modify its band structure for electronics application. In 2009

McCreary et al. doped a graphene layer with adatoms of different transition metals and different concentrations. In particular three different metals with different work function (Ti, Fe and Pt). They found that the different properties of the metals resulted in three different doping efficiency. So for low metal concentration, different metals with different work-function influence only the doping efficiency and not the doping type [39].

In 2010 also Ren et al. evaporate gold, silver and copper on a graphene sheet finding that the characteristic electronic structure of graphene is not significantly altered by the deposition of these metals; however, the deposited metal does cause the Fermi level to move away from the conical Dirac points in graphene, resulting in an effective increasing of carrier density of electrons or holes. They also discovered that the bigger is the metal coverage the less are the electrons that goes into graphene [40].

In 2011 Huh et al. doped graphene selectively using patternable gold nanoparticles functionalized with photoreactive cinnamate moieties. The gold nanoparticles were patterned on the graphene by UV-induced cross-linking of cinnamate (Ci-AuNPs). The patterning procedure is described in Figure 2.9.

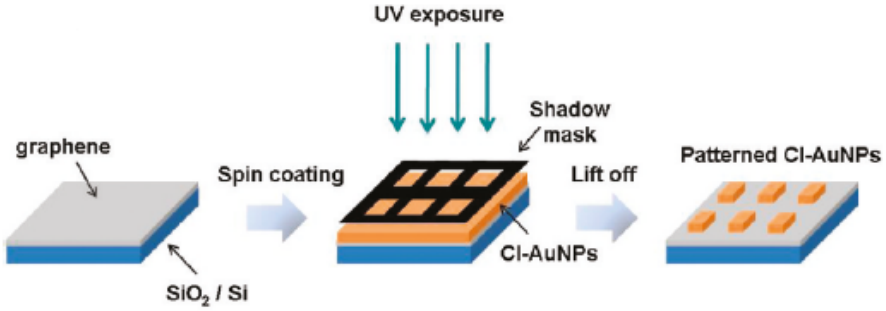

Figure 2.9: Patterning procedure of Ci-AuNPs on graphene [41]

The resulting data showed a tendency toward negative shift of the Dirac voltages as the concentration of Ci-AuNPs solution treated on the graphene was increased indicating a n-type doping of gold nanoparticles on graphene [41].

Another study about graphene doping with gold has been carried out by Wu et al. in 2012. A first-principle approach has been used to simulate interactions between graphene and different gold (Au) configurations, ranging from small isolated nanoparticles to continuous film. By varying the Au deposition time they noted different shifts of Raman peaks, meaning that we can have p or n type doping respectively. From raman we can see that Au doping change the peak position and shape meaning that the formation of a metal–graphene interface not only results in a redistribution of the electrons, but also to a metal-graphene chemical interaction. From 10 to 30 seconds of deposition time they have spare nanoparticles resulting in n-type doping. After 40 seconds particles start to coalesce and form a thin layer that results in opposite p-type doping. The particle distribution on graphene can be appreciated in Figure 2.10.

Graphene has stronger chemical interactions with the Au particles with respect to thin film. This doping phenomenon is shown in Figure 2.11. Qualitatively these experimental results confirm what was found in [40] and could be interpreted as graphene being n-doped by isolated Au nanoparticles and p-doped by a continuous film, proving that gold nanoparticles acts as dopants on graphene [42].

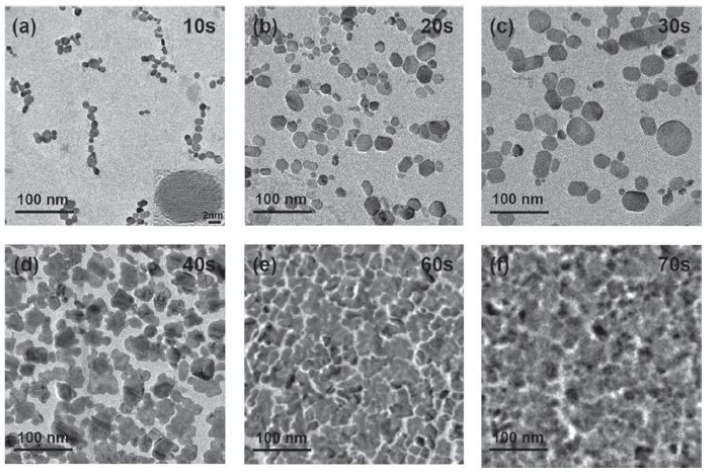

Figure 2.10: a–f) Bright-field TEM images of Au nanoparticles and films on graphene for the deposition times of 10, 20, 30, 40, 60, and 70 seconds [42]

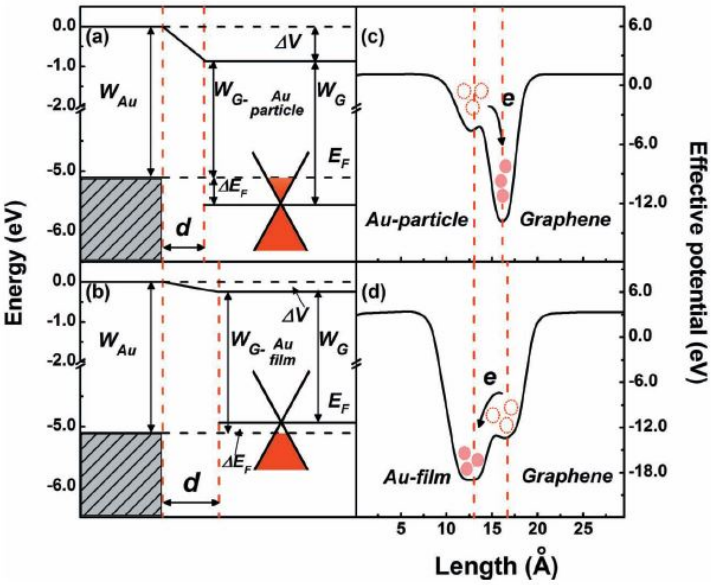

Figure 2.11: a,b) The band alignment illustrations of graphene–Au nanoparticle (a) and graphene–Au fi lm (b) systems [42]

Graphene doping has also been investigated to enhance its sensing properties. In 2012 Gautam et al. doped graphene with colloidal gold and platinum nanoparticle using spin coating, a SEM image of the graphene substrate after particle deposition can be appreciated in Figure 2.12. They tested graphene chemo-resistor towards three organic vapours: ethanol, acetone and acetic acid. They demonstrate the sensing mechanism of graphene based gas sensors towards organic vapours and found that graphene surface functionalized with catalytic metals in sensor devices can be greatly appreciated due to its ability to dissociate organic/inorganic molecules at room temperature with the aid of adsorbed oxygen species [43].

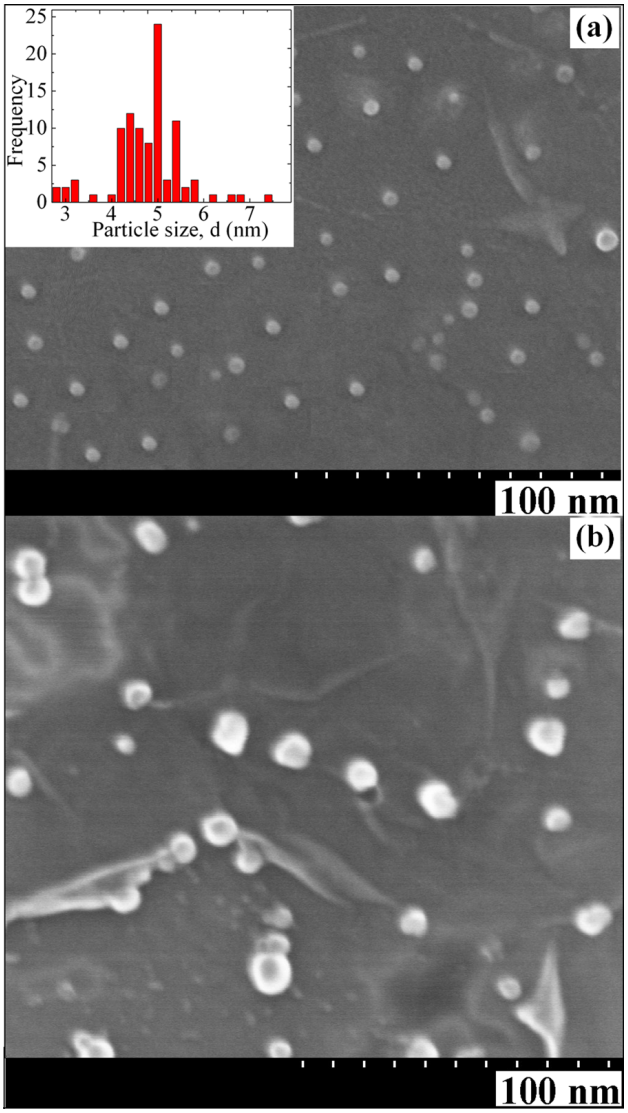

Figure 2.12: SEM images of graphene surface decorated with (a) gold (Au) and (b) platinum (Pt) nanoparticles. Inset is the distribution of gold nanoparticles on graphene surface (in terms of diameter) [43]

Another important study about doped graphene chemo-resistor was carried out by Eriksson et al. in 2014. They fabricate graphene by sublimation of SiC and decorated it with nanostructured thin layers of gold and platinum by magnetron sputtering. They found that both gold and platinum acts as n-type dopants in the rage of 10^3 cm^{-2}. The type of metal and pattern can be optimized to achieve the desired carrier concentration, in particular, the Fermi energy shift due to charge transfer from the deposited metal depends on thickness of metal layer: the thicker is the metal the more is the doping according also to what [40] and [42] found. The substrate decoration with 5 nm of Au results in a faster response to NO_2 with respect to as-grown graphene and a significantly larger response with respect to the 5 nm Pt doped graphene. Temperature doesn't affect selectivity but it is directly proportional to the response magnitude and recovery time. High temperatures (100 °C) are needed to let the sensor work properly. The faster response of doped sensor is more evident in the recovery time with respect to the response time. The different gas response toward NO_2 of doped and undoped sensors can be seen in Figure 2.14. Focusing on gold doped sensors they found that no response to H_2 and CO (as growth graphene had a small response toward both), NH_3 response is in the same range as for as-growth graphene and finally NO_2 sensitivity is two order of magnitude higher that NH_3. The gold doped sensor response can be seen in Figure 2.13. They concluded that the changes in sensor response (sensitivity, speed of response, and selectivity) upon metallization may be due to the generation of different reaction paths or new adsorption sites created by the metal decoration, this could suggest that changing the decoration technique the doping effect would have different results [44].

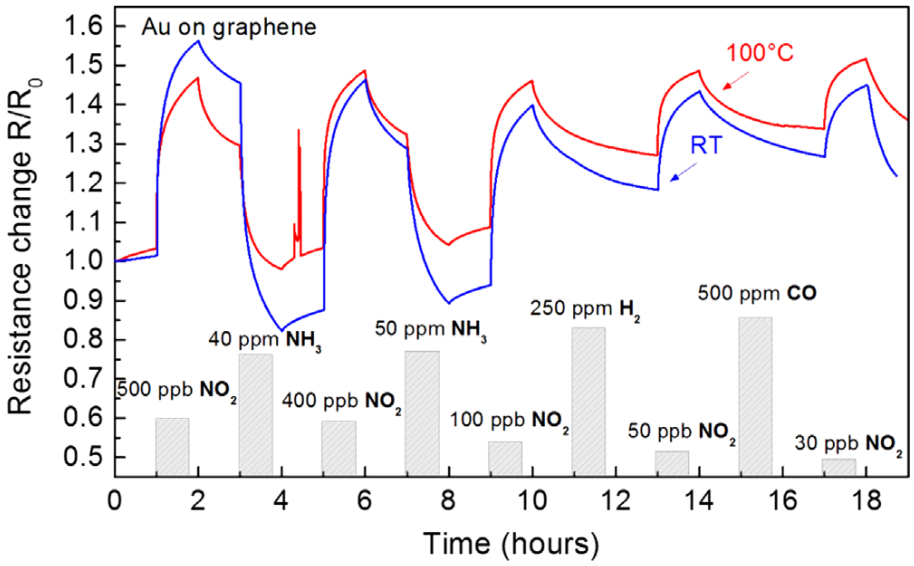

Figure 2.13: Gas selectivity. Response of Au-decorated graphene towards NO_2, NH_3, H_2 and CO at room temperature and at 100 °C. [44]

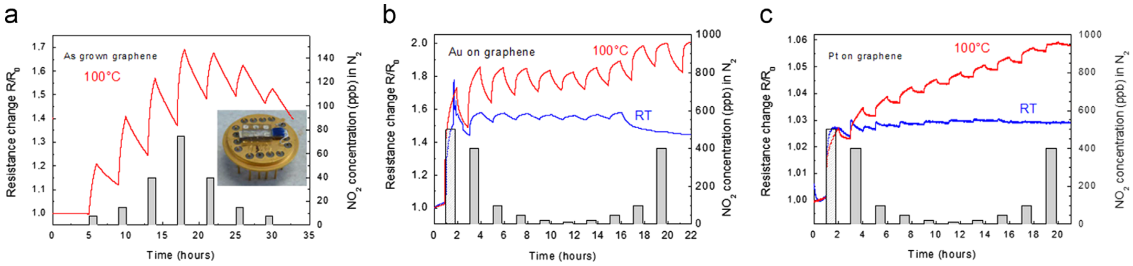

Figure 2.14: Gas sensor response to ppb concentrations of NO_2. Response at room temperature (RT) and 100 °C to NO_2 concentrations ranging from 10 ppb to 500 ppb for as-grown graphene (a), graphene decorated with 5 nm of Au (b) and with 5 nm of Pt (c). Due to very small response, the sensor signal at RT for the as-grown graphene is not shown. [44]

The enhancing of the sensitivity properties of graphene due to doping materials has been also proven with DFT simulations by Zhang et al. in 2010 that simulate the interaction between graphene and organic molecules such as benzene. They found that by introducing a metal atom between the molecules and graphene, the sensitivity of the graphene based sensors could be dramatically improved [45]. It was proved by Zou et al. in 2011 by doping graphene with silicon (SiG) and finding that that SiG could be a good gas sensor for CO, O_2, NO_2 and H_2O [46]. Finally Singh et al. in 2017 by simulating aluminium doped graphene found that graphene with aluminium has a higher chemical reactivity towards all gas molecules and shows higher adsorption energy with NO_2, NH_3 and CO_2 with respect to pristine graphene. Also these results reveal that the sensitivity of graphene-based gas sensor could be drastically improved by introducing the appropriate dopant or defect [47].

Chapter 3

Capillary assembly of nanoparticles

Capillary assembly is a powerful and flexible method for fabricating complex and programmable micro- and nanoparticle assemblies. In recent years it emerged as a good alternative to top-down methods that make exclusive use of lithography, such as optical or electron-beam lithography that are so far the most successful strategies for device fabrication [48]. Top-down methods are intrinsically limited to the patterning of preformed metallic, oxide and polymeric films and layers. As alternatives, bottom-up approaches have been proposed to integrate multiple functional materials via directed assembly [49]. In particular, in capillary assembly particles are positioned by capillary forces so the deposition process is invariant with respect to chemistry and materials under specific conditions (see next sections). This bottom-up approach, integrated with lithography has been proved to be able to place nanoparticles with nanometric precision exploiting capillary forces that arises from liquid surface tension.

Surface tension and contact angle

Surface tension is the tendency of liquid surfaces to shrink into the minimum surface area possible. Intuitively, surface tension arises from an unbalance of the forces acting on molecules at a liquid interface. For instance, a water molecule at the air interface is experiencing a strong cohesion force from other water molecules in the bulk liquid, and a much weaker interaction with air. This creates an inward pressure on the liquid, and is responsible for shaping water in droplets, or other configurations with a minimal surface area. Surface tension has the dimension of an energy by surface unit (J/m) and from a mechanical point of view it can be considered also as a tensile force by length unit (N/m). The surface tension is denoted by γ and its numerical value depends on the molecular interactions: in most oils, the molecular interaction is Van der Waals interaction, leading to quite low surface tensions. For example, in water due to the hydrogen bonding, the molecular attraction is larger ($\gamma = 72$ mN/m).

The situation is more complex at a liquid-solid-gas interface. For instance, at the interface with a container water typically rises up to wet the container or depreciates to

avoid contact. This behaviour arises from the unbalance between the liquid and solid energies, and is quantified by the contact angle. Energetically favourable wetting leads to the well-known fluid rise in capillary tubes. Importantly, the contact angle is not characteristic of the liquid as such, but depends the specific material combination. And to make things worse, it is also influenced by the surface topography, wetting direction, and dynamics. When liquids are in contact with solids, the total surface energy must also include the energy of the solid/vapour interface, and of the solid/liquid interface. These two additional surface energies are also represented by a surface tension γ_{SL} and γ_{SV} respectively. The result of this minimal energy state is indicated by the slope of the air/liquid interface with respect to the liquid/solid interface. This slope create a certain angle that is called *contact angle* (θ). Contact angle on the triple line at equilibrium is given by the Young (or Young-Dupré) equation:

$$\gamma_{LV} \cos\theta + \gamma_{SL} = \gamma_{SV} \tag{3.1}$$

At equilibrium, this angle is called the *static contact angle* θ_S and this value is usually not exactly fixed and presents hysteresis. A schematic representation of the contact angle at a liquid-solid-vapour interface is shown in Figure 3.1. If $\theta < \pi/2$, the liquid wets the surface because of its relatively low surface tension, in this case the substrate is called liophilic. If $\theta > \pi/2$, the surface is called liophobic [50].

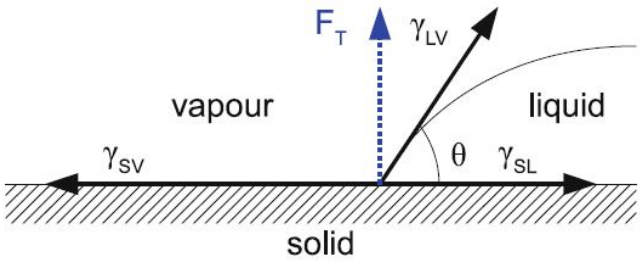

Figure 3.1: Contact angle at liquid-solid-vapour interface [50]

Capillary assembly is essentially a controlled de-wetting process in which the meniscus of an evaporating droplet containing nano/micro scale objects like particles, moves over a predefined topographical template. Capillary forces at the meniscus act as the driving force to assemble the particles into the predefined sites. A convective flux due to evaporation increase the nanoparticles concentration at the contact line creating a so-called accumulation zone (AZ). The process is represented in Figure 3.3. Flux inside evaporating liquid drops was firstly investigated by Deegan et al. in 1997 in order to explain the coffee ring effect [51]. They discovered that due to evaporation the drop volume would shrink, but the radius of the drop cannot shrink when its contact line is pinned. To prevent the shrinkage, liquid must flow outwards from the centre to maintain the height profile and the spherical cap shape dictated by surface tension. In this way we have a convective flux from the centre of the drop towards the external perimeter. This has been also proved by suspending in the liquid drop some nanoparticles . In Figure 3.2 the flux of liquid that prevent the drop shrinkage is represented.

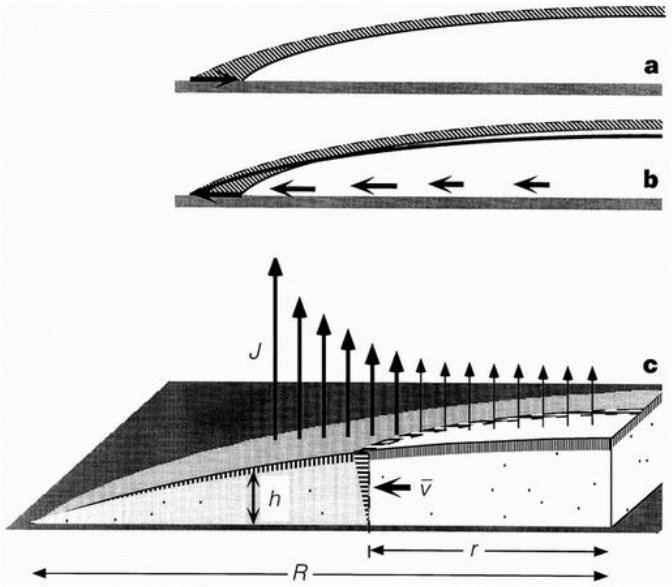

Figure 3.2: Explanation of the coffee ring effect according to Deegan et al. [51]

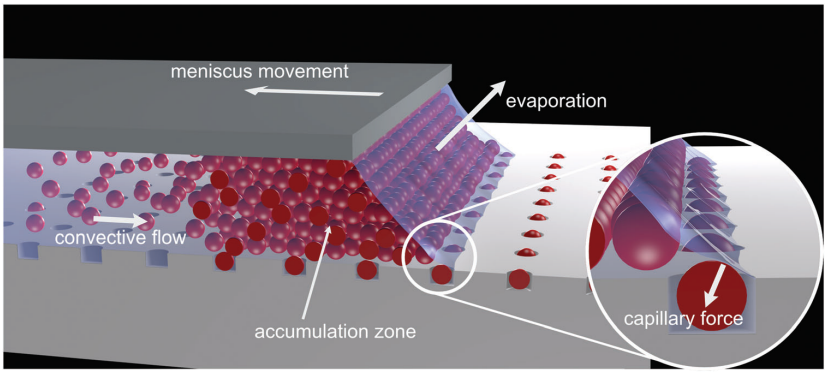

Figure 3.3: Working principle of capillary assembly [48]

In capillarity-assisted particle assembly, this convective flow towards the contact line is opposed by a diffusive particle flux and a recirculation flow. The diffusive flux is fuelled by the concentration gradient of particles between the meniscus and the bulk solution, whereas the recirculation flow is mainly created by the movement of meniscus in the opposite direction of the convective flow, when the droplet is being swept over the template. If the evaporation-driven (i.e., convective) flow overcomes the sum of the other flows, particles will accumulate and densely pack in the front of the meniscus near the contact line, creating AZ. In capillary assembly, the AZ moves over the non-wetting template, and its stability is essential for a successful deposition. Therefore, a proper accumulation zone of particles is a prerequisite for successful capillary assembly [48].

Capillary assembly is influenced by the following parameters:

- Wetting conditions: surface energy of involved materials
- Substrate temperature and relative humidity: to regulate the particle flux inside the drop
- Stability of particle suspension
- Meniscus velocity
- Trap design and geometry

Active research in recent years has highlighted the properties and potentiality of capillary particle assembly.

In 2007 Kraus et al. used surfactant systems to tune the drop wetting behaviour with more flexibility and change particle–surface interactions. A surfactant system for particle inking has to change the contact angle of the colloidal suspension with the substrate. They found a highest assembly yield with a receding contact angle during deposition between 50° and 60°. The surfactants should not destabilize the colloidal particles and it should only leave a very thin film on the inked plate. They found that some surfactants hinder the assembly, possibly by creating a repulsive force between substrate and particles, whereas others (such as polyvinylpyrrolidone) form deposits that embed the particles on the substrate. A mixture of a non-ionic, rather hydrophobic surfactant appears to avoid all these issues, leaving the colloid stable even at high concentrations. The surfactant system ensures a proper receding contact angle on an unstructured surface, but the local contact angle during assembly also depends on the pinning caused by the structures on the template surface. To achieve high yields without unspecific deposition, both an appropriate geometry and a sufficient depth of the capture sites have to be chosen. They also found that substrate temperature influence the evaporation rate. As the evaporation rate increases, the recirculation zone moves away from the meniscus. Higher colloid temperature and lower outside humidity increase particle flux to the assembly region both by increasing flow rates from the bulk and by decreasing the particle recirculation. They were able to fabricate lines, arrays and complex arrangements of nanoparticles with high accuracy and single-particle resolution that retains individual particle functionality [52].

In 2007 Malaquin et al. investigate two complementary methods to create particle assemblies ranging from full layers to sparse arrays of single particles starting from colloidal suspensions of gold and polystyrene particles using the setup illustrated in Figure 3.4. These two methods are named *convective assembly* and *capillary assembly*. Both are based on the confinement of particles induced at the three-phase contact line of a droplet that is dragged over a substrate. *Convective assembly* mechanism is based on the convective flow of a solvent induced by evaporation of the droplet that drags the particles toward the contact line and can be obtained on wetting substrates for contact angle values below 20° (Figure 3.5 a). The profile of the liquid meniscus close to the contact line leads to a vertical confinement of the suspended particles into a thin film of solvent. The assembly process starts when the thickness of the solvent layer becomes equal to the particle diameter.

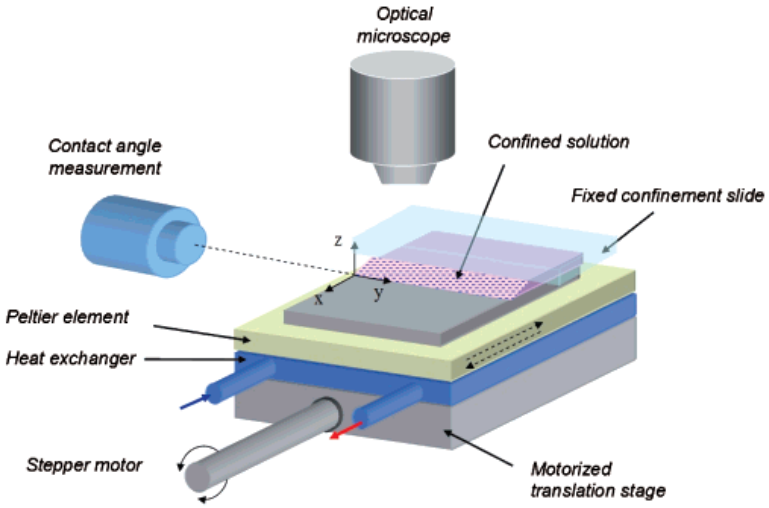

Figure 3.4: Illustration of the experimental setup developed for controlled convective and capillary assembly of particles on surfaces. [53]

When the contact angle of the liquid suspension increases, however, the confinement effect induced by the meniscus decreases. Above a critical contact angle value, the horizontal force exerted by the liquid meniscus becomes high enough to prevent particles from depositing onto a flat substrate (Figure 3.5 b). If the surface is patterned appropriately, this force component can be countered by a vertical structure. While the contact line is being dragged over the patterned substrate, the liquid meniscus is pinned and deforms around the structure. The combination of geometrical trapping at the substrate features and capillary forces exerted during film breakage leads to one particle or a small number of particles being confined close to the obstacle, in this case we have *capillary assembly* (Figure 3.5 d). The mechanism leading to particle deposition in this case is not yet fully understood, particularly at the instance when the film breaks up over the structures. Their experiments suggest that these capillary forces are important for, but not sufficient to explain particle trapping. They also investigated the combination of convective assembly with patterned substrates (Figure 3.5 c). The flows created by evaporation of the solvent predominate the mechanisms responsible for particle motion during the assembly and also their experiments suggest that the resulting accumulation region is essential to trigger the assembly process. Adjusting the evaporation by means of the substrate temperature allows them to control both the yield and the speed of assembly and even to reverse the assembly process. Controlling the substrate temperature is the most efficient way of controlling the evaporation rate, better then controlling humidity that is usually a slow process requiring a cumbersome experimental setup. They also found that for a substrate temperature lower than dew-point the flux stops and the convective assembly is no more possible, this could be exploited to remove particle previously deposited on the substrate and it is represented in Figure 3.6.

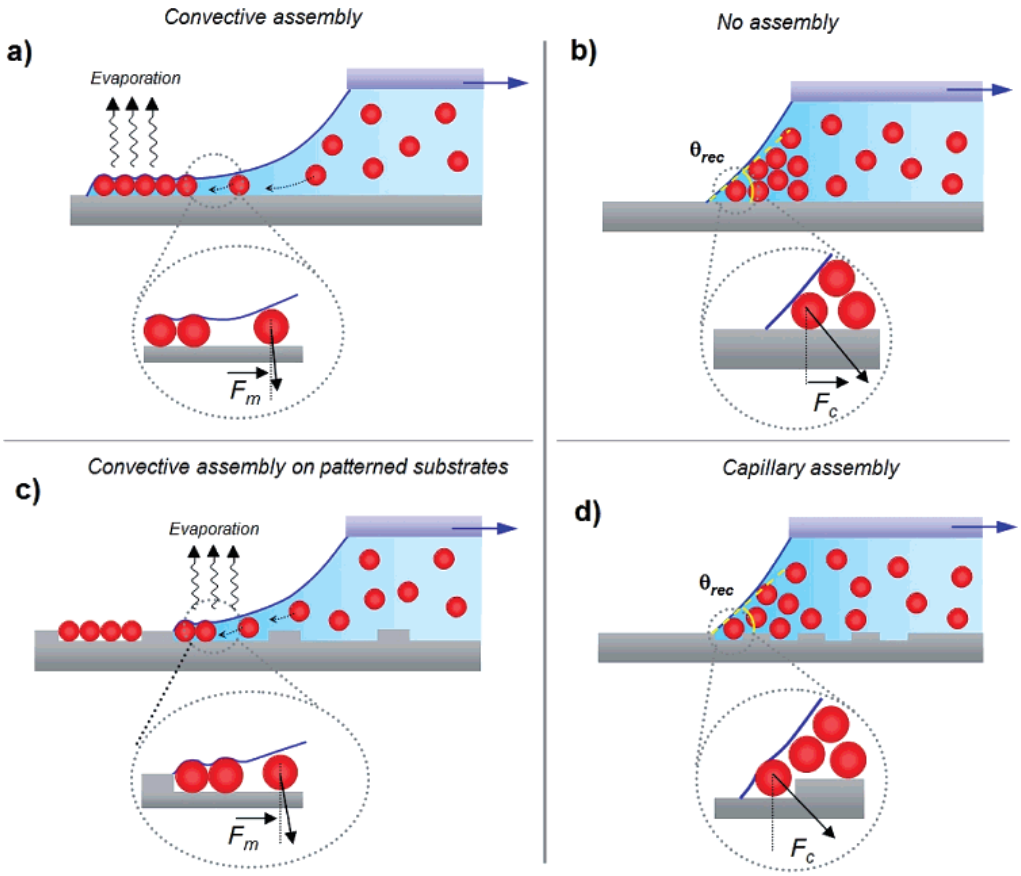

Figure 3.5: Various assembly mechanisms based on particle confinement at the contact line of a droplet can be distinguished depending on the wetting properties and topographical patterning of the substrate [53]

To guarantee a correct deposition rate, the nanoparticle influx toward the drying region must compensates for the particle consumption due to the layer growth. In order to investigate the temperature influence in the formation of AZ, they did deposition with two different substrate temperatures: 27 °C and 32 °C. In the experiment performed at 27 °C, in situ observations did not show any particle immobilization on the substrate. When increasing the temperature to 32 °C, particles were selectively trapped in the structures as shown in Figure 3.6 b) with a yield of 99%. Experimental results reveal that there is a threshold temperature and the existence of this threshold confirms the importance of the hydrodynamic flows created by evaporation on the assembly. This threshold corresponds to a situation in which the particle influx induced by evaporation overcomes the depletion due to diffusion, recirculation, and the deposition of particles on the surface and form the accumulation zone.

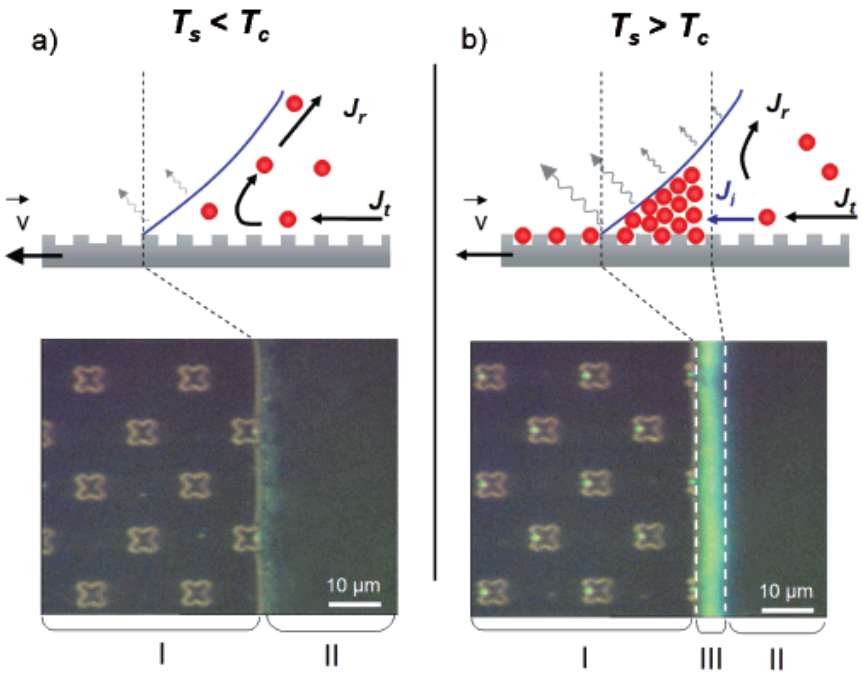

Figure 3.6: Illustration of the influence of temperature on the motion of particles during capillary assembly. (a) At low temperatures, evaporation does not compensate for the recirculation flow, and no particle deposition is observed. (b) As the substrate temperature increases above the dew point, evaporation induces a particle flow toward the contact line. [53]

They found that the accumulation process assists the confinement of the particles in the structures in two ways:

1. The local increase of the particle concentration due to their accumulation close to the contact line helps to increase the probability of trapping one particle in a structure.

2. The accumulation of particles close to the contact line contributes to the reduction of the mobility and fluctuations of particles in the substrate that is due to Brownian motion.

Deposition angle is a crucial parameter for a good assembly and it can be tuned by using surfactants. Increasing the surfactant concentration resulted in a decrease in the contact angle, which eventually led to a change from capillary to convective assembly for contact angle values of less than 15°. At this contact angle, the horizontal component of the capillary forces exerted by the meniscus becomes too weak to prevent particle deposition. For what concerns the deposition angle they found that the best angle at constant speed of 1 μm/s was found to be 60 $\pm$ 4 °. Above this value, no deposition could be observed, even if an accumulation region was established close to the contact line. Particle assembly was successfully achieved for contact angle values between 30° and 60° [53].

In 2011 Born et al. exploited convective assembly process in a meniscus at the edge of a suspension reservoir. They did an extensive work of modelling of the phenomenons that are involved in capillary assembly. They found macroscopic defects of the deposited films caused by contact line pinning. These mechanisms depend on contact line dynamics, the particle flux and the space available for assembly, all of which are connected to the meniscus shape. They modelled the pinning on defects by evaluating the spring constant of a deformed meniscus. Their model expresses the dependence of the spring constant on the contact angle, the smaller is the contact angle the lower is the spring constant, the less is the energy added to the meniscus. These ruptures are mainly caused by substrate dis-homogeneity and can be seen in Figure 3.7. They found that the meniscus shape depends on the setup and influences film deposition. Contact angle and meniscus curvature together govern the deformability of the meniscus. A deformable, slack meniscus can accommodate different deposition conditions, prevents defects from spreading and has a low tendency to pin and form holes in the particle film. The deposition thus becomes robust against the ubiquitous perturbations of process conditions [54].

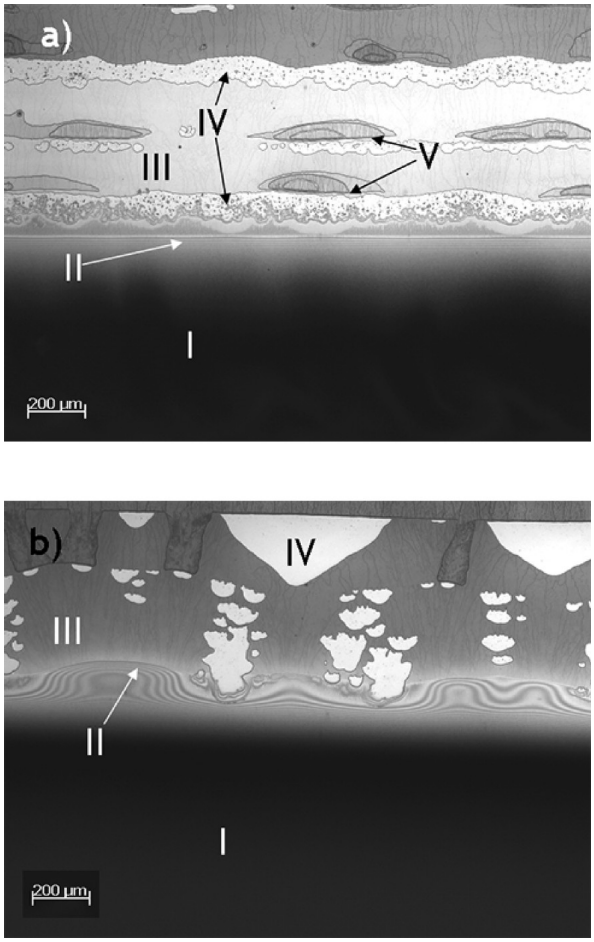

Figure 3.7: Ruptures in assembly homogeneity found by Born et al. Pinning phenomenon can be appreciated [54]

In 2012 Kuemin et al. employed top-down fabricated nanostructured templates for the oriented assembly of bottom-up synthesized, colloidal gold nanorods suspended in cetyl trimethyl ammonium bromide (CTAB) solution. They used a deposition speed of 0.5-1 μm/s and a concentration of CTAB of 0.9 mM, resulting in an initial contact angle of 50° ± 3° when hydrophobic poly dimethyl siloxane (PDMS) templates was used. They found that pre-alignment of the nanorods in the solid domains is not a prerequisite for successful assembly whereas the dense packing is essential. In terms of the resulting assembly yield, it is critical to have sufficiently large traps in order to induce contact line pinning, moreover the assembly yield increased for an increased extension of the accumulation zone. They demonstrated that short, shape-anisotropic gold nanorods can be assembled in an oriented fashion by combining top-down surface patterning with a bottom-up directed self-assembly process [55].

In 2014 Ni et al. found that trap depth is a key parameter in controlling the capillary assembly of single and multiple particles in predefined templates [56]. The moving meniscus is pinned, and thus deformed, by the topographical traps. This meniscus deformation will create an elastic restoring force, which can act upon particles protruding from the traps (F_c in Figure 3.8) and thus hold them in the trap. This force relates to the amount of protrusion and the tension of the elastic meniscus, and therefore depends on the trap depth relative to the particle size and on the surface tension of the moving droplet.

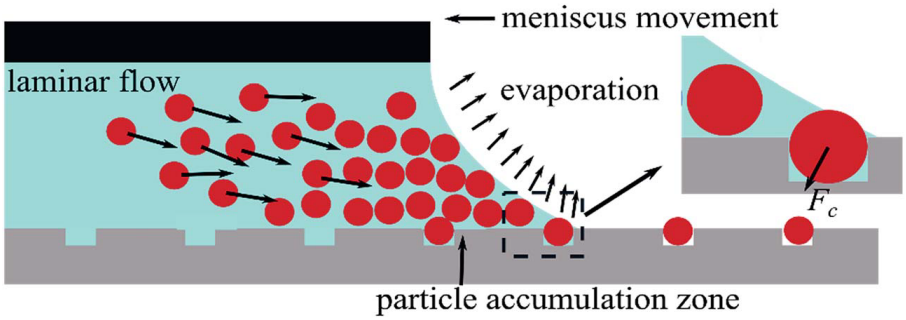

Figure 3.8: Schematic of the working principle of capillary assembly [56]

They carried out the assembly at a speed of 2 μm/s and the temperature was set 15–25 °C above the dew-point to have a sufficient AZ. They also created a model like [54] for the spring constant of the meniscus on the trap pinning. Surface tension effect was investigated by using three solvents with three different surfactants concentration. In conclusion, they have demonstrated that an accurate design of the template geometry and precise control of the assembly conditions make capillary assembly an ideal tool to direct and program the assembly of complex particle patterns [56].

In 2015 Asbahi et al. demonstrated single particle positioning of sub-10 nm particles from liquid suspensions using a moving macroscopic meniscus over a pre-patterned template. At these length scales, particle dynamics is less influenced by the capillary force of the macro-meniscus, as the latter exhibits a large capillary length compared to the particle size. Instead, at such small length scales Brownian motion and pair poten-

tial forces strongly dominate thus creating the undesirable random assembly of particles. They create conditions suitable for a thin film of hexane to form and confine a single layer of 8 nm diameter Au nanoparticles (AuNPs) on the substrate surface relying only on topographical features of the template, thus avoiding surface functionalization processes that could be sensitive to contamination. They used in particular the spreading mediated directed self-assembly of nanoparticles (SMDSA-n), the patterned sample was put in contact with the hexane nanoparticles suspension and get covered by capillary, the thickness of the climbing film was estimated by ellipsometry to be 100 nm. The sample was then raised above the suspension bath and left to dry for 30 min in the hexane rich environment. During this process, the evaporation of hexane results in a thin but uniform film. Nano-menisci, that is, receding drying fronts of this thin film, form at the top of the sample and spread throughout the sample to finally push the particles into the template cavities. Since particles are too small for optical microscopy for tracking during the assembly process, they obtain insight on the mechanism that leads to successful assembly through Brownian dynamics (BD) simulations. They simulated two different film thickness: 10 and 30 nm and found that 30 nm thick film increases vacancy defects and lowers filling yield. Since contact angle plays a significant role in DSA-n performance. A series of systematic BD simulations for contact angles of 10°, 30°, and 50° at different liquid thicknesses (15 and 30 nm) suggest that large liquid thickness and contact angles lead to large vacancy defects. However, small fluid thickness and contact angle confine the particles to the least possible nearest neighbour interactions, facilitating deposition by the nano-meniscus, which further enhances DSA-n coverage [57].

In 2016 Flauraud et al. deposited gold nanorods on a patterned and silanized substrate for functional optical and electro-optical nano devices. They identified and investigated three distinct sequential stages in the dynamics of the capillary assembly of nanoparticles namely: 1)Insertion, 2)Resilience and 3)Drying that encompass the trajectory of single nanoparticles from the initial colloidal suspension to the final placement onto topographical substrates. The three stages are also represented in Figure 3.9 They demonstrated that each stage significantly and distinctively affects the cumulative yield of the assembly process and designed effective traps geometrically tailored in all three dimensions to achieve an optimal assembly performance. They found that accumulation zone extension has the biggest impact on deposition yields, relative orientation of nano-traps and receding contact line angle not influence assembly yield if the accumulation zone is extended enough. An entropy-driven phase transition orders the thin hard nanorods within the accumulation zone. The nanorods closest to the receding contact line orient their main axis parallel to the contact line across several adjacent rows. Under such tight confinement, loss of translational entropy excludes that nanorods rotate to fit into an underlying trap not parallel to the contact line [58].

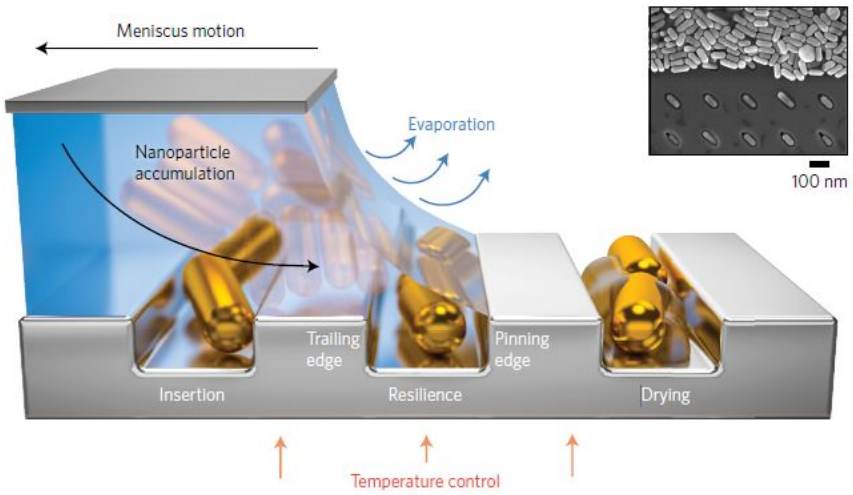

Figure 3.9: Schematic of the capillary assembly of nanoparticles onto topographical traps of a low-wetting substrate (dimensions not to scale) [59]

Pinning of the receding contact line along solid edges transiently lowers the contact angle. Consequently, the local rate of solvent evaporation increases and the vertical component of the solvent/vapour interfacial tension pushes the nanoparticles closest to the contact line onto the recessed traps. They consider 4 types of traps:

- straight-edged
- funnelled
- straight-edged with auxiliary sidewall
- funnelled with auxiliary sidewall

The traps are represented in Figure 3.10. Independently of trap width, trap depth improves the assembly yield by providing a higher barrier against removal. Nanorods assembled into straight-edged traps of width tightly accommodating the effective nanorod diameter in solution end up only loosely confined after drying, because of their reduced interaction diameter in the dry state. This issue limits the placement accuracy achieved to date by using straight-edged traps. On the other hand, sidewall-biased solvent evaporation can be exploited for predictable post-insertion orientation of nanorods within traps. A bottom trench narrower than the effective particle diameter mechanically locks the nanorod during solvent evaporation precisely at the centre of the trap. Assembly yield enhanced from 15% without the funnel to 98% in the case of 50-nm wide funnelled traps parallel to the contact line. To further enhance the assembly performance through a more effective counteraction of nanoparticle removal, they placed an additional vertical barrier along a single edge of the traps, a 30-nm-thick hydrogen silsesquioxane (HSQ) sidewall lithographically defined within 10 nm of a trap edge.

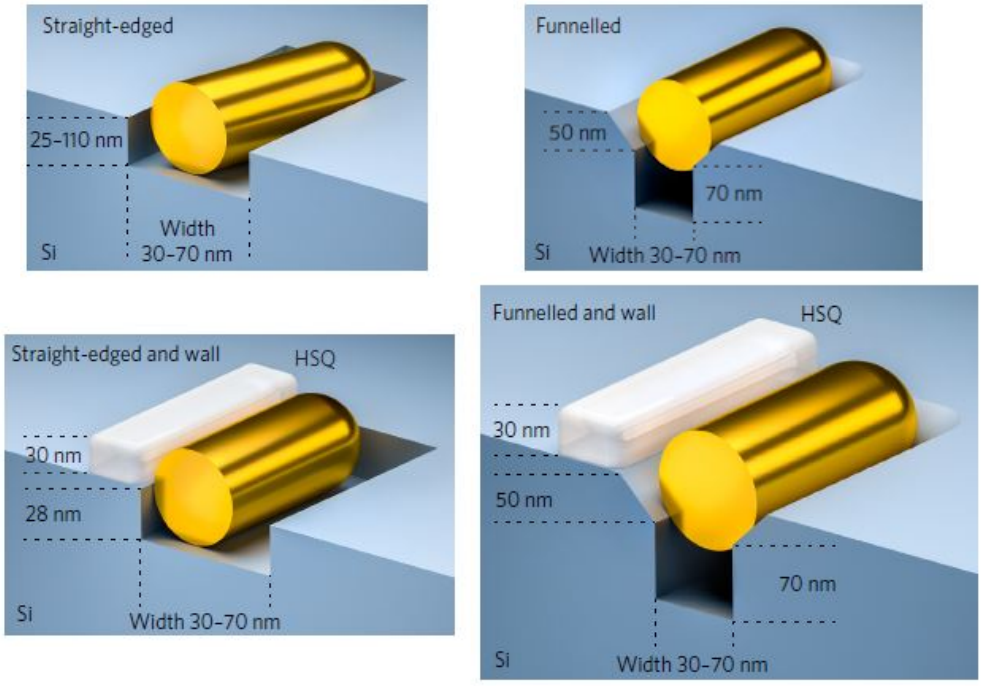

Figure 3.10: Three-dimensional design of trapping sites for nanoparticles in capillary assembly [59]

They have shown how specific topographic patterning of solid substrates can fully determine the capillary assembly of Au nanorods with 1 nm resolution. They point out that this method is largely independent of substrate and nanoparticle composition, as it can be extended to arbitrary surface patterns and to out-of-plane orientation as well as to other types of nanoparticle [59].

In 2017 Virganavicius et al. demonstrated the successful high area deposition of nanoparticles into highly ordered arrays by capillary forces on patterned templates using a custom-built capillary force assisted particle assembly setup. Experiments with different patterns were carried out at different temperature and velocity regimes. Temperature control was performed using a thermoelectric cooling controller, employing a Peltier element with water cooled back side and Pt100 thermoresistance sensor. Particle assembly experiments were carried out at ambient temperatures of 21–22 °C and relative humidity of 36–40%. The dew point for these conditions was estimated to be in the range of 6–7 °C. Once the temperature settled, receding angle of the prepared suspension at the contact line (three phase liquid-solid-vapor interface) was measured to be 45° ± 2°. They found that high yield assembly can only occur when the AZ is formed in the front of the droplet meniscus. Increased speed of the translator enables to perform faster deposition but also results in a quick depletion of particles in the accumulation zone and a drop in the deposition efficiency. An increase of substrate temperature increases the particle influx from

the bulk of droplet into the accumulation zone enabling a sustained deposition at higher speeds, but this stops eventually when certain temperature is reached and the particles start to deposit into agglomerates. Some results are reported in Figure 3.11. Particle density in the assembly pattern directly translates into selection of optimal process conditions. Their findings reveal that the highest deposition velocity at which successful, high yield assembly can be performed is directly related to the pattern density [60].

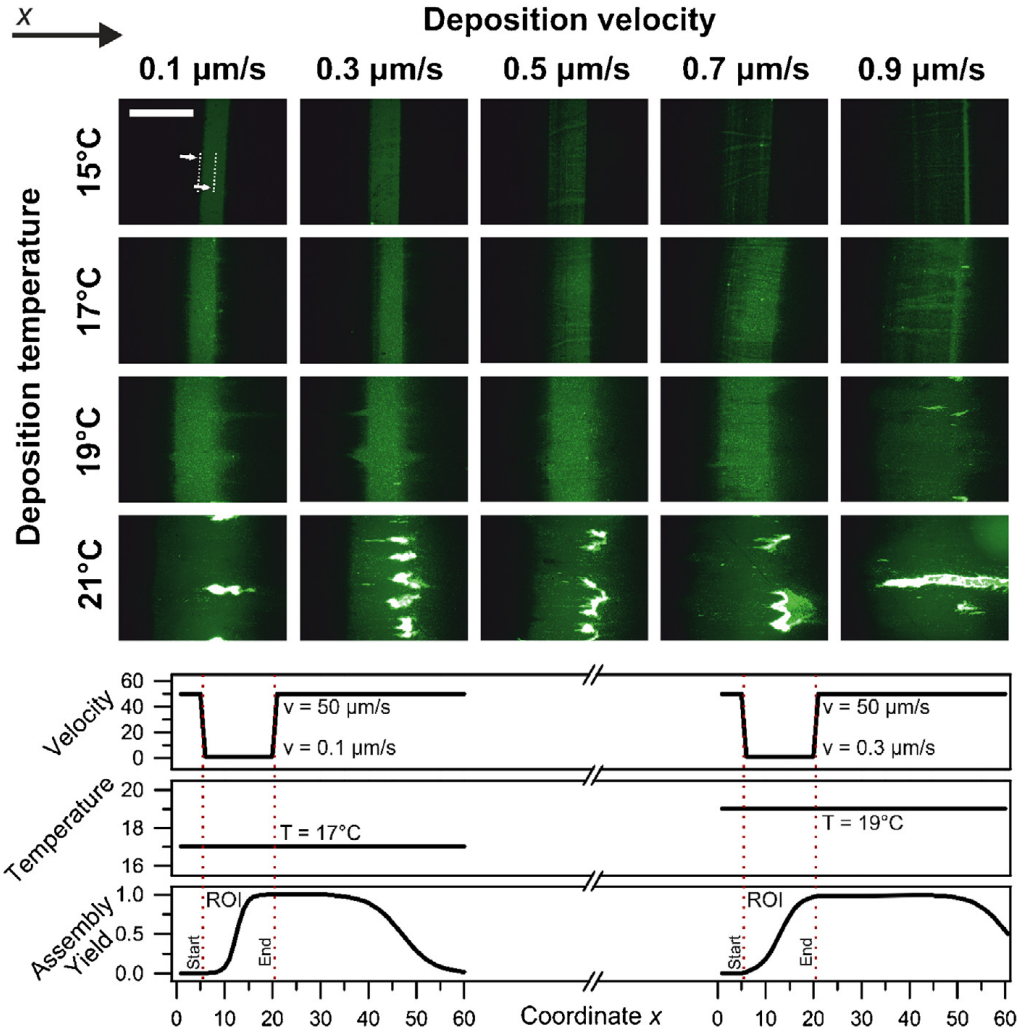

Figure 3.11: Stack of micrographs depicting a macroscopic view of particle deposition areas at different deposition conditions. Deposition direction is along the x axis. Scale bar is 200 μm and applies for all cases. Schematic graphs illustrating production of the transition zone (assembly yield curves) produced at two different velocities and different temperatures during the experiments are also presented [60]

Finally, in 2018 Ni et al. in their review article summarized that typical deposition angles of the droplet on the templates range between 30° and 75°. The angle can be tuned

by the addition of varying amounts of surfactants to the suspension, with trapping being more favourable at the lower end of the range. Lowering the contact angles even further eventually results in convective assembly of continuous layers. In capillary assembly, the template defines the locations at which the particles will ultimately be placed. The moving speeds reported typically range from 0.2 μm/s to 5 μm/s, depending on whether a stable AZ of particles can be maintained. A high speed will induce a strong recirculation flow, which damages the AZ of particles near the contact line, and prevents assembly. The processing temperature is another critical parameter that determines the convective flow in the droplet as well as the establishment and maintenance of the AZ. A heating element is often integrated to adjust the processing temperature. Typically, processing temperatures of 10–20 °C and 30–50 °C above the dew-point temperature are selected for micro-particles and nano-particles, respectively [48].

As a conclusion of this review of recent literature, capillary assembly seems a good candidate technique to precisely functionalize graphene by filling defects with nanoparticles. This approach will be described and developed in the rest of this work.

Part III

Experimental results

Chapter 4

Graphene fabrication

4.1 Else Kooi Laboratory

All the work presented in this thesis has been carried out at Else Kooi Laboratory (EKL), the in-house cleanroom facility of Delft University of Technology. The Else Kooi Lab (entitled to the Dutch chemist inventor of LOCOS technique [61]), is specialized in IC production, photonic devices, organs on chip and MEMS technology. It comprises class 100 (ISO 5) and class 10'000 (ISO 7) areas, MEMS Laboratory with dedicated sections for measurements and special applications. It is mainly used by the ECTM research group, the group which I join in to develop the present work.

Figure 4.1: Else Kooi Laboratory logo.

4.1.1 Equipment

As previously said, EKL laboratory is composed by 3 main areas, the class 100 area is a CMOS-compatible cleanroom and all the machines can perform batch fabrication on 4-inch silicon wafers with up to 25 silicon wafer per carrier . This is a brief list of equipment and technology that is possible to use inside the cleanroom:

- High temperature furnaces for dry and wet oxidation, annealing, diffusion, LPCVD, silicidation and alloying.
- Plasma machine for RIE/DRIE of metals, polymers, ceramics and oxides, PECVD, plasma treatments with oxygen.
- Bonding and packaging, dicing, wire and wedge bonders and pick and place.
- Lithography machines, spinners and hotplates, automatic coating/developing station, contact aligner and wafer stepper.

- Optical, laser and electron microscopes, ellipsometer, contact angle and thin layer thickness measurement
- Ion implanter for CMOS production, magnetron sputtering PVD, ALD, epitaxy, graphene CVD and much more.
- Wet benches and fume hoods: chemicals for wet etching of metals and oxides, cleaning lines and polymer technology lines

4.1.2 Behavioural rules

Inside the cleanroom a lot of dangerous chemicals are stored, moreover all the machines work with high voltages and hazardous gases. A list of behavioural rules must be followed in order to minimize the risk of hurting yourself and the other users. First of all, it is necessary for everybody who wants to work inside EKL to follow a safety course, which comprises of a cleanroom tour to learn the gowning procedure and to locate the position of all the emergency exits, extinguishers, emergency/calamity buttons, and diphoterine/hexafluorine kits for seriously emergency accidents. Then the user must be trained for every machine he is planning to use, every machine has a person in charge for the training. Here is a brief list of behavioural rules that must be respected inside the EKL laboratory:

- When working at wet benches with acids and basis we need to always use the *buddy system*. It requires that a minimum of two people are inside the EKL labs at all time. A buddy is another knowledgeable user within the facility, such as a staff member or a good experienced user, who can and will watch over you and care for you in case of trouble.
- When working at wet benches always wear protective glass and gloves. Moreover it is forbidden to put acid (like HNO_3 next to organics compound like Acetone or IPA)
- When we need help or we are not 100% sure about what we are going to do, always ask to the engineer on duty (EOD) before. His/her name is written at the cleanroom entrance.
- It is not allowed to start your process without an approved flowchart and run number. A run number can be obtained from the process coordinator.
- The last person in the cleanroom 100 or SAL must check if no other persons are left behind or are in trouble, if water taps are closed, hotplates are switched off, etc. Every person working after 18:00 in the cleanroom 100 or SAL is considered to be the last person in the lab.
- All users of equipment must fill in the equipment log book, and record all process runs and results. Recent logbook notes from previous users can be used to calculate process times.
- Understand the difference between red and green metals, this is crucial to avoid contamination. Contaminant materials must be stored is their special coloured boxes.

4.2 Graphene growth

Graphene has been produced in cleanroom 10'000 using the Axitron BlackMagic pro CVD reactor. In 2018 Dong et al. [21] found that synthesizing graphene with metal catalyst, sputtered on different silicon oxide layer thicknesses lead to two different defects concentration on graphene surface. For this reason, we decided to work with two different SiO_2 thicknesses: 90 nm (sample W1) and 600 nm (sample W4). Silicon wafers were oxidized in the furnace to create the SiO_2 desired thickness with both dry/wet oxidation, the exact recipe used to oxidize the wafers is reported in Appendix B.

On top of the oxidized wafer, 50 nm of 3N5 pure molybdenum is sputtered at 50 °C using a SPTS Sigma DC magnetron sputter coater. Then, MLG was grown in Ar and H_2 mixture at 25 mbar pressure and 915 °C temperature for 20 min, using 25 sccm of methane as carbon precursor.

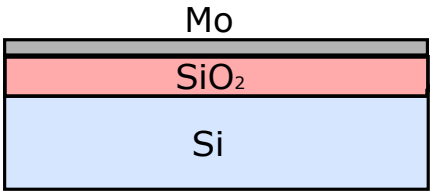

Figure 4.2: Materials stack on the silicon wafer before graphene growth

The temperature profile starts with a three stages slow ramp up to 915 °C in order to reduce thermal stress in the Si and Mo layers. The first stage is the fastest one with a rate of 125°C/min, rising from room temperature to 550°C. It is followed by a slower ramp rate (50°C/min) till 725°C. For the third stage, the ramp up rate is 30°C/min and lasts until the final temperature (915°C) is reached. A 1 min interval for temperature stabilization is included between the different ramp up stages. When the temperature is reached, methane is inserted inside the chamber for 20 minutes at 25 sccm (with an hydrogen flow of 40 sccm). After this 20 minutes, heaters are switched off and the chamber is left cooling passively until ambient temperature with 960 sccm argon flux. When the temperature is below 150°C the reactor could be opened. The temperature and gas profile for the process is illustrated in Figure 4.5.

Figure 4.3: Axitron BlackMagic pro

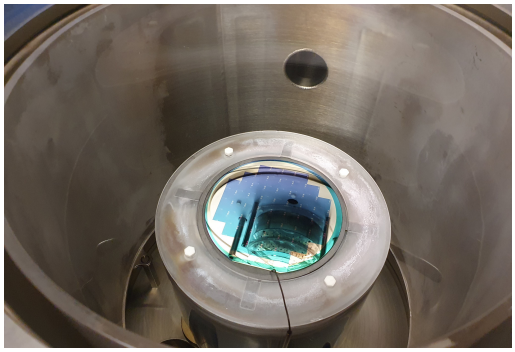

Figure 4.4: BlackMagic chamber

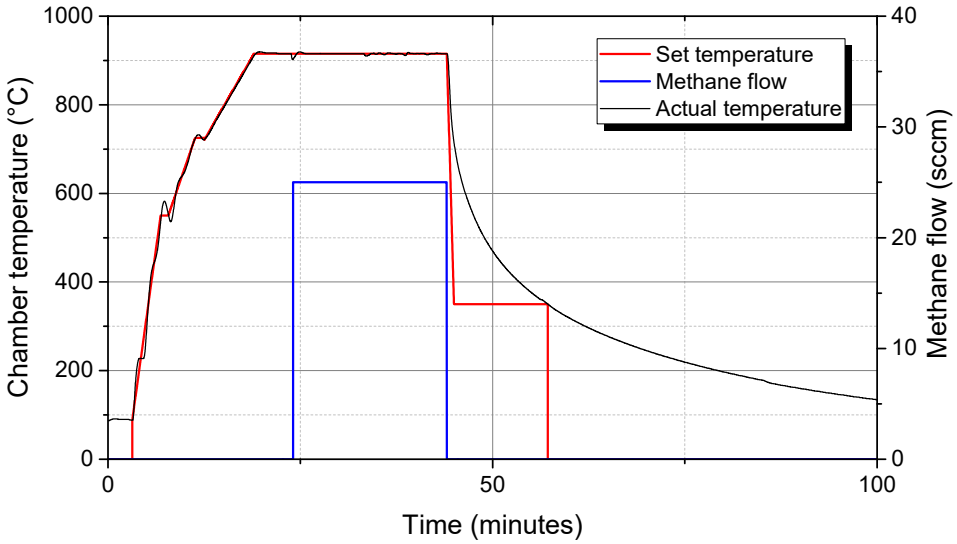

Figure 4.5: Axitron BlackMagic pro temperature and gas profile

4.3 Substrate transfer

After the growth process, wafers were analysed with a Raman spectrometer in order to check the quality and prove the growth of graphene layer on the thin metal layer. The next step was to transfer the graphitic material on a different substrate, and this was done in MEMSLab, substrate transfer is needed to remove the conducting metal catalyst and exploit the graphene properties. The target substrate to transfer graphene was silicon oxide, 100 nm silicon oxide was grown in the furnace using dry oxidation at 800 °C for 4 hours. Graphene was transferred also on a glass substrate in order to be inspected with the UV/Vis spectroscopy. All the studies on these samples will be reported in the next chapter.

Graphene scooping

The scooping technique is a really easy transfer process used to rapidly fabricate samples. It allows us to transfer graphene from metal catalyst to an insulating substrate without requiring any support materials (like PMMA), it exploits the surface tension of water in order to transfer graphene to the new substrate using dip coating-like mechanism. The adopted process was the following:

1. Sample with as grown graphene on top is cut in small rectangular pieces of about 1 by 2 cm^2 by hand, this size is chosen according to the following steps. The piece is then placed in a small beaker and a small amount of Hydrogen Peroxide 31% VLSI Selectipur® by BASF is introduced with a pipette on the beaker side in order to be sure to not cover the metal surface (20ml). As soon as the peroxide level is higher than the silicon die, it start flooding and we can stop to pour hydrogen peroxide.

2. Hydrogen peroxide starts etching molybdenum from the edges, after 10 minutes the oxidizing process is already started and this can be clearly seen in picture 4.6b.

3. When molybdenum is completely etched the graphene detaches from the substrate and starts floating on the liquid surface. We sometimes found that graphene could be damaged in the centre due to a non uniform etching of the metal. Graphene is kept stretched by the surface tension of the air/hydrogen peroxide interface.

4. A that point we can start pouring deionised water with a pipette inside the beaker to dilute the hydrogen peroxide and increase the water level. This operation must be carried out very carefully in order to minimize the turbulent flow on the surface that could brake or damage the fragile graphene.

5. We can stop pouring water when the water is higher enough to scoop the graphene.

6. Then we can submerge the target substrate in the water under the graphene and pull it up.

7. The graphene will adhere to the silicon oxide and will gently deposit on the substrate. When the water will be evaporated, the graphene will adhere to the substrate.

This transfer technique offers several advantages with respect to the one that involve a polymer sacrificial layer. It require less materials, and less steps leading to a faster process. Moreover it doesn't leave any polymer residues on the graphene. All these steps are represented in Figure 4.6, numbers under images are referred to the numbered list presented on top. In the next chapter when we will exanimate the graphene surface morphology after scooping, we will discuss about the possible influence that this transfer process had on samples.

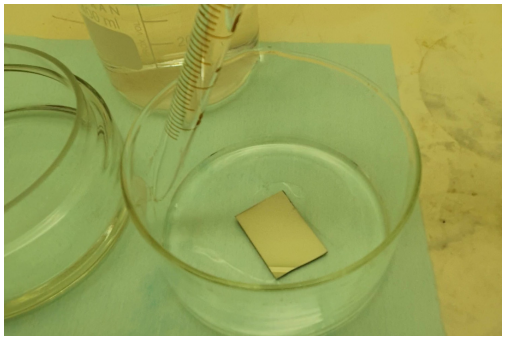

(a) scooping step 1

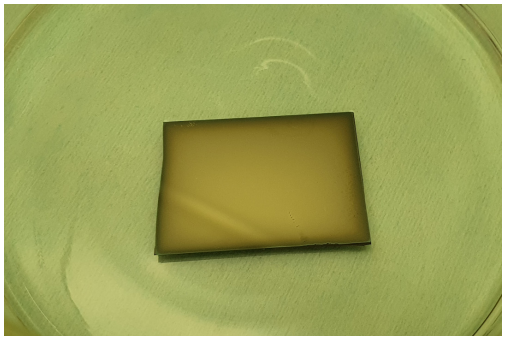

(b) scooping step 2

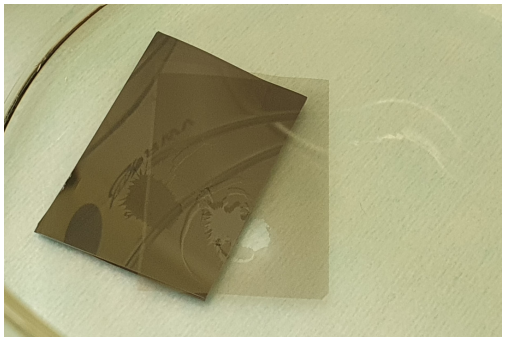

(c) scooping step 3

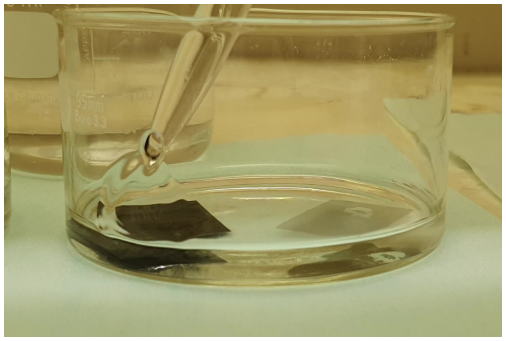

(d) scooping step 4

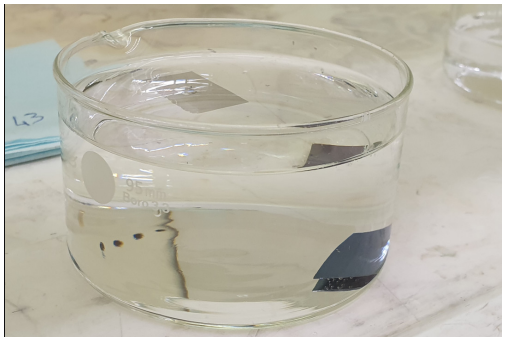

(e) scooping step 5

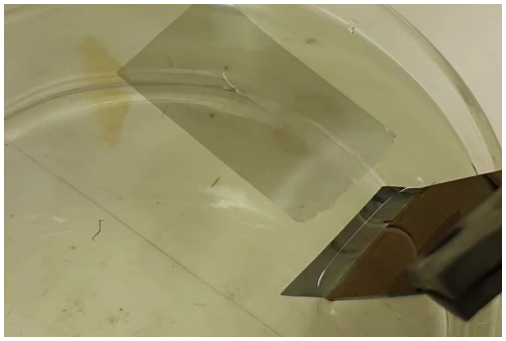

(f) scooping step 6

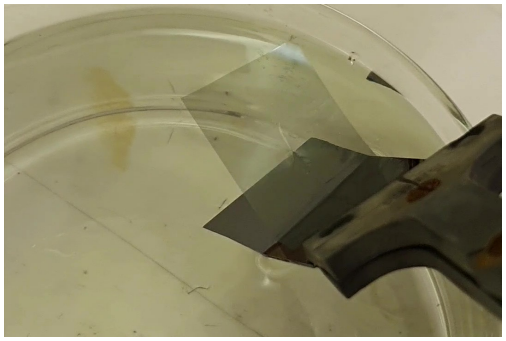

(g) Step 7

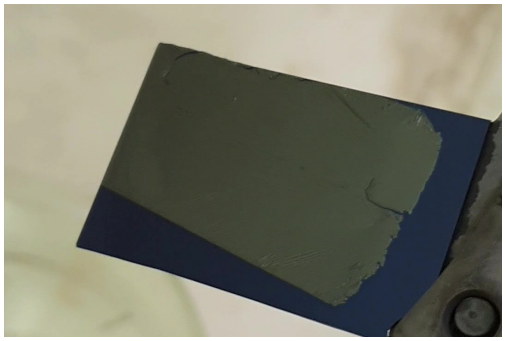

(h) Step 8

Figure 4.6: Graphene scooping, the silicon oxide substrate is 1 by 2 cm^2

The final result of scoping after the water evaporated can be seen in Figure 4.7 on SiO_2 substrates and in Figure 4.8 on a glass substrate.

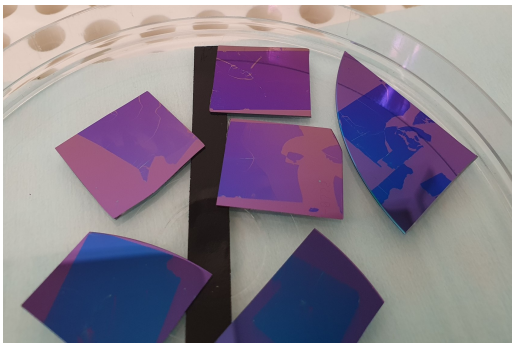

Figure 4.7: Graphene transferred on silicon oxide substrate after scooping

Figure 4.8: Graphene transferred on a glass substrate after scooping

PMMA transfer process

We investigated also the PMMA transfer and compare it with the scooping. We decided to try drop casting of the PMMA instead of spin coating to obtain a thicker layer of polymer that could result in a better support for graphene. Here is the used recipe:

1. PMMA is dissolved in chlorobenzene with a concentration of 46 mg/mL.
2. PMMA is drop casted on the sample.
3. The sample is soft baked at 150°C for 5 minutes on a hotplate.
4. The sample is put into a 31% H_2O_2 solution in order to etch the molybdenum. When the metal is completely etched the graphene + PMMA layer is released from the substrate.
5. The sample is dried overnight.
6. The sample is put on a silicon oxide substrate and then the PMMA is removed using acetone.
7. The sample is then dried

All these steps are represented in Figure 4.9, numbers under images are referred to the numbered list presented on top. Analysis of the transfered graphene using PMMA will be reported in the next chapter.

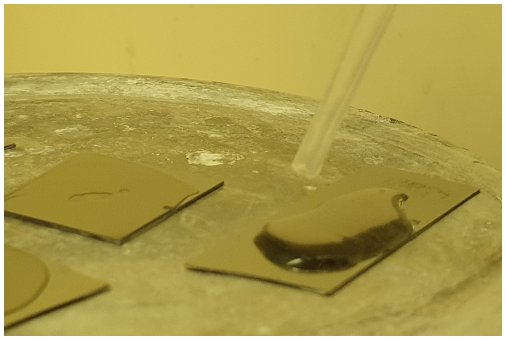

(a) PMMA transfer step 2

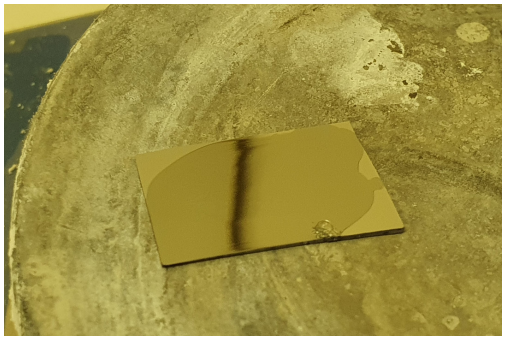

(b) PMMA transfer step 3

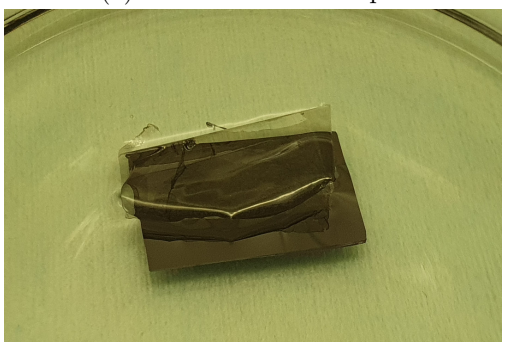

(c) PMMA transfer step 4

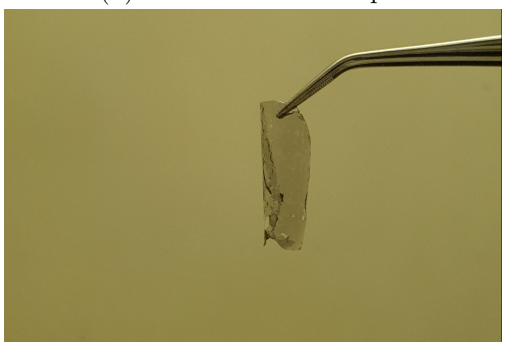

(d) PMMA transfer step 5

Figure 4.9: Graphene transfer using PMMA, the silicon oxide substrate is 1 by 2 cm^2

Chapter 5

Graphene characterization

In this chapter we will characterize the previously made samples. In particular we will evaluate if this synthesized graphene is a good substrate for nanoparticle doping exploiting the capillary assembly technique.

5.1 Raman spectroscopy

Raman spectroscopy was performed on samples using a Renishaw inVia Raman microscope with 633 nm laser. The laser power was set to 5 mW to avoid damage to the samples. The Raman spectra were acquired in the 1100-3200 cm^{-1} Raman shift interval which is the interval where carbon materials present the common features. For each sample 5 spectra were acquired on different points of the surface. The acquired spectrum was successfully analysed with an automated script that removed the baseline, normalized the spectrum intensity with respect to the G peak, and fitted the D, G and 2D peaks with lorentzian function returning for each peak: position, intensity (I) and FWHM. These figures of merit are useful to compare different samples. In Figure 5.1 a normalized Raman spectra of graphene growth on molybdenum is shown. The presence of a marked G peak prove that graphitic material was formed. In Tables 5.1 and 5.2 the aforementioned figures of merit are reported for graphene of sample W1 and W4.

Substrate	I(D)/I(G)	I(2D)/I(G)	FWHM(2D)
Molybdenum	0.23 ± 0.05	0.72 ± 0.15	62.3 ± 5.8
Silicon Oxide (Scooping)	0.27 ± 0.02	0.93 ± 0.07	56.0 ± 2.9
Silicon Oxide (PMMA)	0.52 ± 0.02	1.20 ± 0.07	54.8 ± 1.2

Table 5.1: Raman figures of merit for graphene of sample W1 (90nm SiO_2 thickness) before and after transfer on silicon oxide using scooping and PMMA transfer

Substrate	I(D)/I(G)	I(2D)/I(G)	FWHM(2D)
Molybdenum	0.25 ± 0.03	0.95 ± 0.10	64.0 ± 2.9
Silicon Oxide (Scooping)	0.29 ± 0.02	1.00 ± 0.08	53.8 ± 2.5

Table 5.2: Raman figures of merit for graphene of sample W4 (600nm SiO_2 thickness) before and after scooping

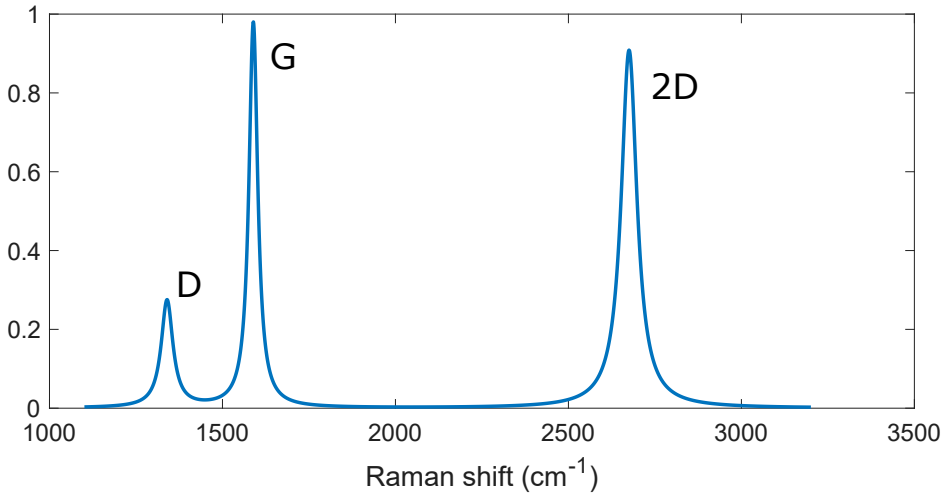

Figure 5.1: Raman spectra of graphene on molybdenum growth with the recipe described in the previous section. Intensity is normalized with respect to the G peak

From these Raman results we can conclude that:

- the presence of a marked G peak prove the existence of graphitic material.
- since the I(2D)/I(G) ratio is < 2 the grown graphene is multilayer (MLG).
- the presence of D peak proves the indicates the presence of defects.
- No significant difference can be found from Raman analysis between sample W1 and W4 leading to the results that silicon oxide thickness under the metal catalyst doesn't influence the overall growth process.
- Transfer with scooping doesn't introduce significant defects on graphene since the I(D)/I(G) ratio doesn't increase much after scooping.
- Transfer with PMMA seems to alter the MLG, in particular, the higher I(D)/I(G) ratio indicate an increase of defects in the hexagonal carbon lattice, defects are probably caused by polymer/graphene interaction.

5.2 Optical transmittance

In order to have an estimation of the graphene thickness, we evaluated the optical transmittance of MLG using a PerkinElmer UV/Vis spectrometer Lamda 1050+. After transferring the graphene on a transparent substrate (Figure 4.8) we found that at a wavelength of 550 nm the transmittance T was 76.4% for graphene of sample W1 and 64.5% for graphene sample W4. By using the empirical formula of Zhu et al. [62] we estimated the number of graphene layers. The optical transmittance T(ω) of graphene films as a function of incident light frequency ω can be written as:

$$T(\omega) = \left[1 + \frac{2\pi}{c} G(\omega)\right]^{-2} \tag{5.1}$$

where G(ω) is the optical conductivity of the graphene film, and c is the speed of light. In the visible region, by neglecting the interlayer interaction, the optical conductivity of multilayer is linearly proportional to the layer number N as G(ω) = N·G$_1$(ω), where G$_1$(ω) is the optical conductivity of single-layer graphene at frequency ω. G$_1$(ω) only becomes equal to the universal optical conductance G$_0$ = e^2/(4$\hbar$) in the limit of a massless Dirac fermion band structure, where e is the elementary charge, and $\hbar$ is the reduced Planck constant. The optical transmittance of multilayer graphene can be simplified to:

$$T(\omega) = \left[1 + \frac{2\pi}{c} N G_1(\omega)\right]^{-2} \tag{5.2}$$

where G$_1$(ω) = f(ω)G$_0$. f(ω) is a correction coefficient to compensate the deviation between G$_1$(ω) and G$_0$. Equation 5.2 can be further revised including the well defined value G$_0$ as:

$$T(\omega) = (1 + f(\omega)\pi\alpha N/2)^{-2} \tag{5.3}$$

Here, α = e^2/($\hbar$c) $\approx$ 1/137 is the fine-structure constant [5] whereas f(ω) was found to be 1.13 at 550 nm wavelength from both numerical simulations and transmittance measurements by Zhu et al. [62]. By using 5.3 we found that sample W1 was composed by 11 layers whereas sample W4 was composed by 19 layers. The results are reported in Table 5.3. In order to estimate the thickness from the known number of layers, we found from Siyu et al. that a graphene layer is 0.34 nm thick [63], so we found an estimated thickness of MLG of 3.7 nm for sample W1 and 6.5 nm for sample W4. Worth to remember that according also to Wu et al. the growth mechanism of graphene on Mo is both surface adsorption and diffusion and precipitation process, so the cooling rate is a parameter to tune graphene thickness. Faster cooling leads to thinner films [13].

Sample	T @550 nm	Number of layer	Estimated thickness
W1	76.4%	11	3.7 nm
W4	64.5%	19	6.5 nm

Table 5.3: Graphene number of layers and estimated thicknesses

5.3 SEM

Graphene samples after scooping on silicon dioxide substrate were inspected with the Philips XL50 scanning electrons microscope (SEM). We tried also to image graphene on molybdenum but detector was not able to capture any significant signal. Images were taken at different magnitude (25000x, 50000x, 100000x and 200000x) show that graphene surface is not homogeneous. The brighter regions in the images can be attributed to spots of material with different conductivity, in particular the brighter colour means that the material has lower conductivity so it can be identified as silicon dioxide, graphene edges are typically also brighter. The brighter spots seems to be holes on the graphene layer and they represent a good candidate sites for particle trapping in capillary assembly.

Multiple pictures was taken for every samples in different locations. They confirmed that the defects distribution on graphene is homogeneous. In Figure 5.2 sample W1 is shown, whereas in Figure 5.3 sample W4 is shown. In order to characterize the density of defects and compare the two different samples we used the ImageJ software to evaluate a figure of merit. This figure of merit is the ratio between the defects area and the total picture area, the analysis was carried out on 25000x and 50000x magnitude pictures and the defects area was evaluated by applying a brightness threshold filter to the images respectively of 120/255 and 160/255. The results are listed in Tables 5.4 and 5.5. In contrast to what Dong et al. found [21], the density of defect on the two samples is almost the same, according also to Raman analysis no density defects difference can be highlighted between sample W1 and sample W4.

Sample	Defects area
W1	4.19 %
W4	4.33 %

Table 5.4: Defects area in 25000x magnitude SEM picture

Sample	Defects area
W1	2.54 %
W4	2.23 %

Table 5.5: Defects area in 50000x magnitude SEM picture

Sample W1

In Figure 5.2d we can see sample W1 imaged with 200000x magnification. The image is not very clear because the SEM microscope is working at its operating limits but holes and wrinkles can be clearly seen. Wrinkles are small regions in the order of nanometre where graphene is folded. This folding phenomenon probably happen in the scooping phase when MLG is floating on the water meniscus and they also concur to the hole formation.

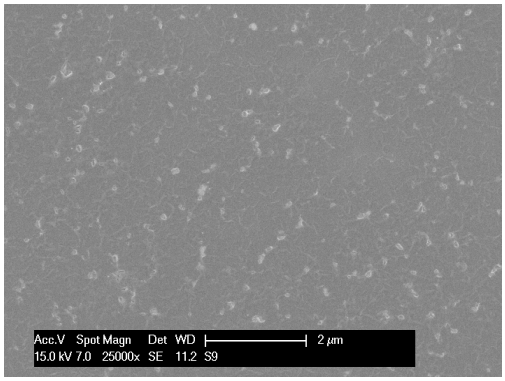

(a) SEM image of sample W1 25000x magnification

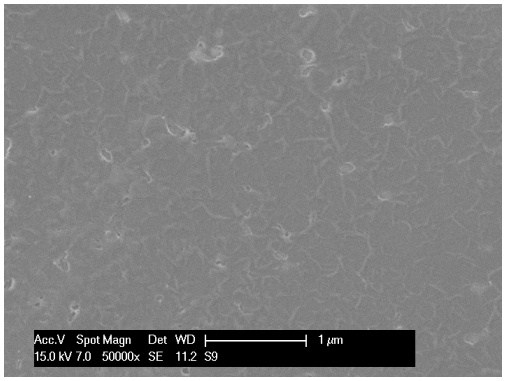

(b) SEM image of sample W1 50000x magnification

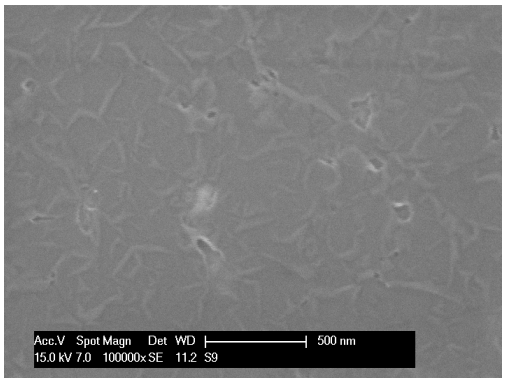

(c) SEM image of sample W1 100000x magnification

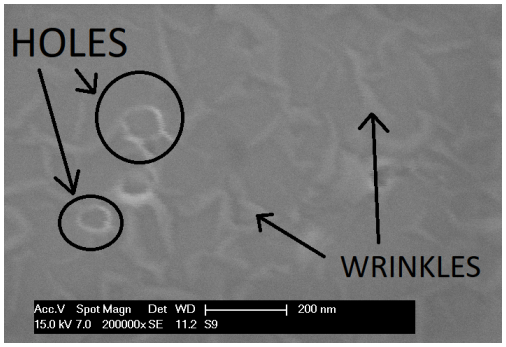

(d) SEM image of sample W1 200000x magnification

Figure 5.2: SEM images of sample W1

Sample W4

As previously said no difference can be highlighted from sample W1. Also in sample W4 we can point out wrinkles and holes in Figure 5.3d imaged with 200000x magnification.

PMMA transfer

In Figures 5.4 and 5.5 we also report the SEM images of graphene scooped using PMMA and drop casting technique. As can be seen, this sample presents big cracks probably caused by an incorrect temperature management in the transfer recipe. The cracks are uniformly distributed on the graphene and are present at different scales. In Figures 5.4 and 5.5 we can see the bigger one that are hundreds of micrometre long and of few micrometre width. Since also Raman analysis revealed a lot of defects in this sample from now on we will consider only samples obtained by scooping transfer technique.

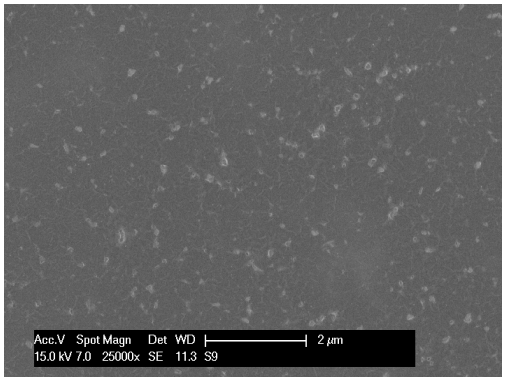

(a) SEM image of sample W4 25000x magnification

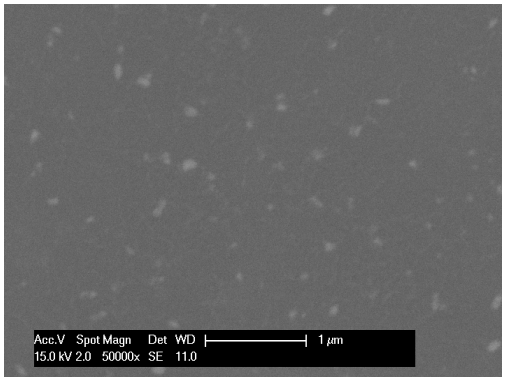

(b) SEM image of sample W4 50000x magnification

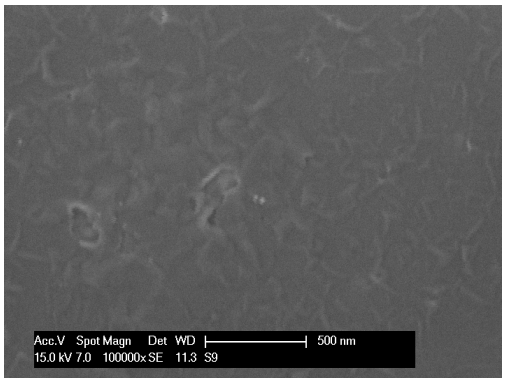

(c) SEM image of sample W4 100000x magnification

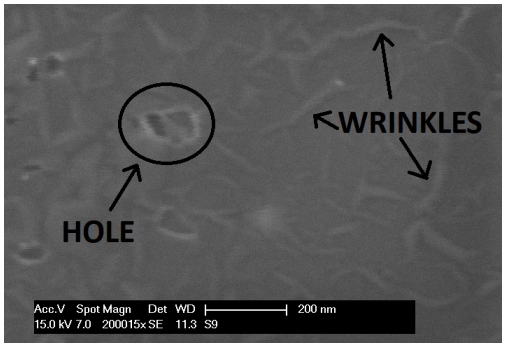

(d) SEM image of sample W4 200000x magnification

Figure 5.3: SEM images of sample W4

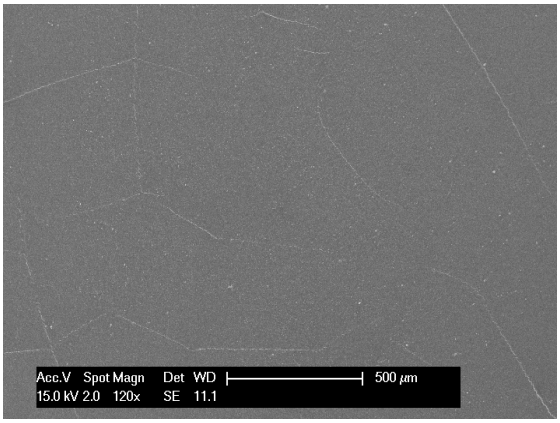

Figure 5.4: SEM image of graphene PMMA transfer

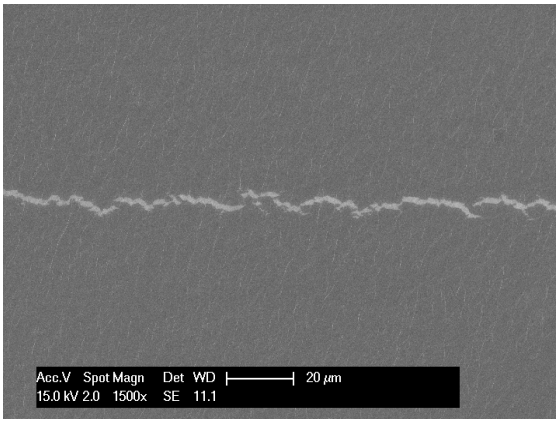

Figure 5.5: SEM image of graphene PMMA transfer

5.4 AFM

Samples were successively analysed with AFM to have a better understanding about the surface morphology, in particular to better investigate wrinkles and defects. AFM measurements were carried out employing a NT-MDT NTEGRA setup, with a gold tip having a radius of 10 nm and a Bruker FastScan setup with a silicon tip both operating in semi-contact mode.

Sample W1

Graphene was firstly inspected on molybdenum substrate immediately after growth. The graphene morphology on molybdenum is reported in Figure 5.6. As confirmed by Vasic et al. [64] roughness of graphene originates from patches with slightly increased height and from the grain structure of the underlying substrate. The graphene mean roughness in this case is 4.16 nm and it could be reduced by using molybdenum foils as substrates [18], it woth mentioning that mean roughness of as sputtered molybdenum was less that 1 nm, so during growth surface roughness increased. Rutkov et al. in 1994 [65] found that molybdenum turns into Mo_2C upon exposure to carbon, before the graphene formation and due to this recrystallization into Mo_2C the substrate roughness increases [20]. Mo_2C grains can be clearly seen as lighter and darker areas in Figure 5.6.

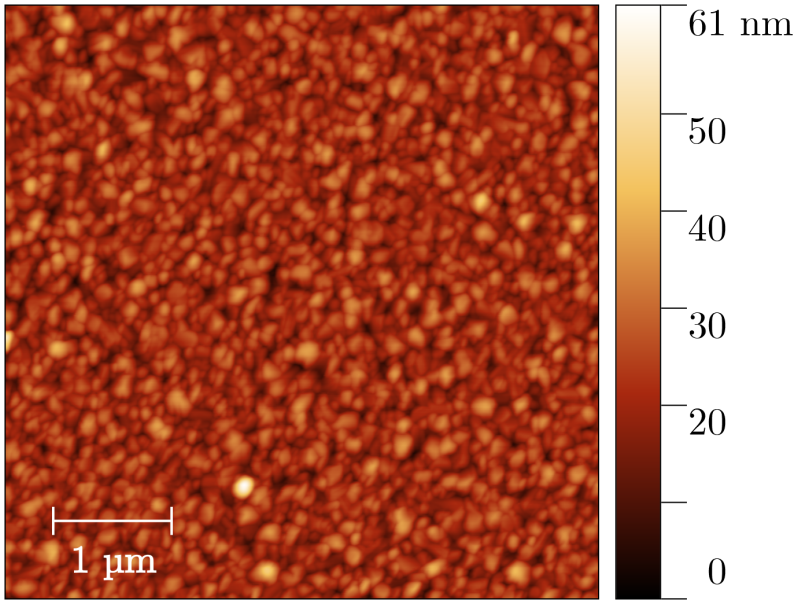

Figure 5.6: AFM scanning of graphene on molybdenum

Figures from 5.7 to 5.12 represents graphene of sample W1 on silicon oxide substrate after scooping at different scales. Figure 5.13 show the height profile number 1 of Figure 5.7. We can see that graphene surface is not completely flat, it has a mean roughness of 4.23 nm and presents some abrupt non-uniformity. Since mean roughness is not increased during the scooping process we can conclude that it doesn't influence surface roughness. In picture 5.14 we can see the height profile number 2 of Figure 5.6. The black areas in

the picture can be clearly identified as holes in the graphene film according also to what was found with the SEM images. Finally in Figure 5.15 the height profile number 3 of picture 5.12. In this case we highlight the cross section of a small wrinkle, we can see that the height profile almost doubles when graphene is folded. Wrinkles don't contribute so much to surface roughness and as previously said they are likely caused by the scooping transfer process. Surface roughness is mainly caused by the metal catalyst during the growth process.

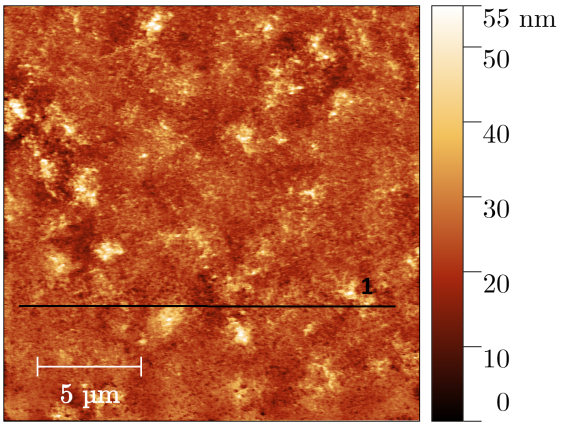

Figure 5.7: AFM scan of sample W1 5um with scale

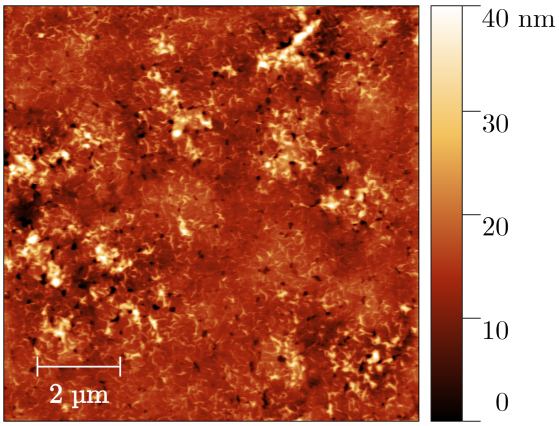

Figure 5.8: AFM scan of sample W1 with 2um scale

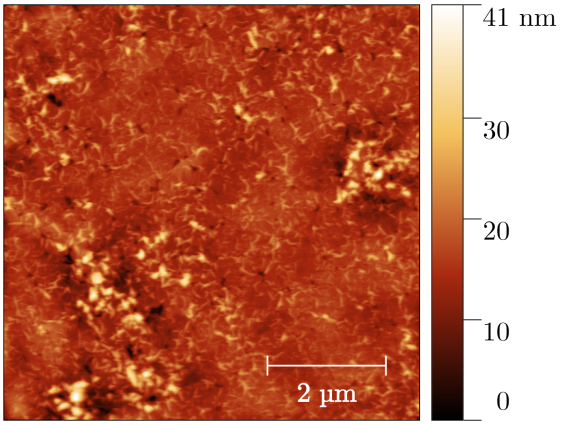

Figure 5.9: AFM scan of sample W1 500um scale

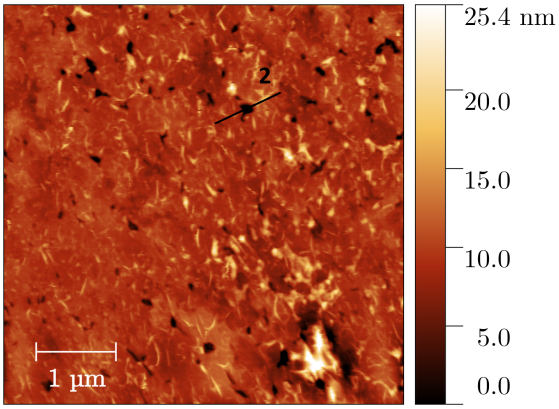

Figure 5.10: AFM scan of sample W1 1um scale

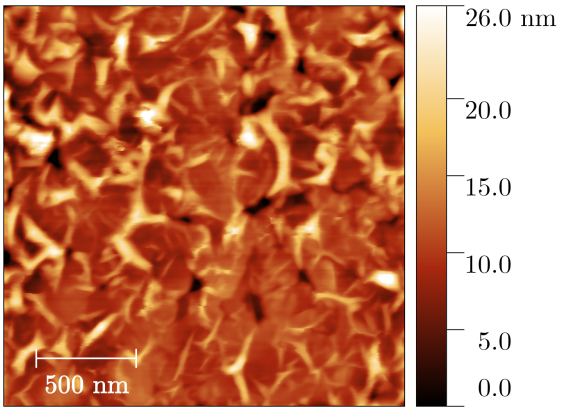

Figure 5.11: AFM scan of sample W1 500nm scale

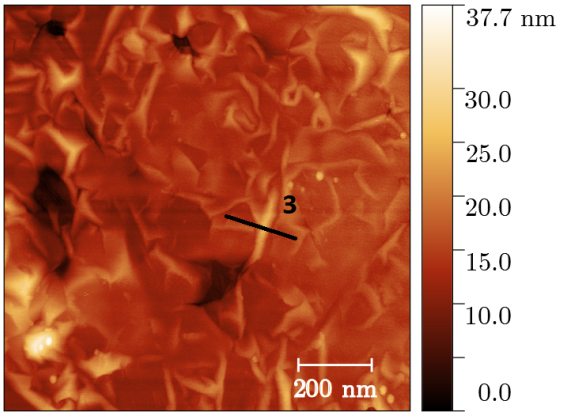

Figure 5.12: AFM scan of sample W1 500nm scale

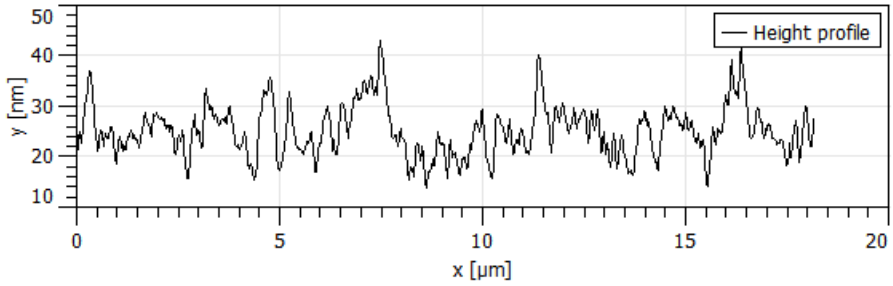

Figure 5.13: Profile height number 1 of sample W1

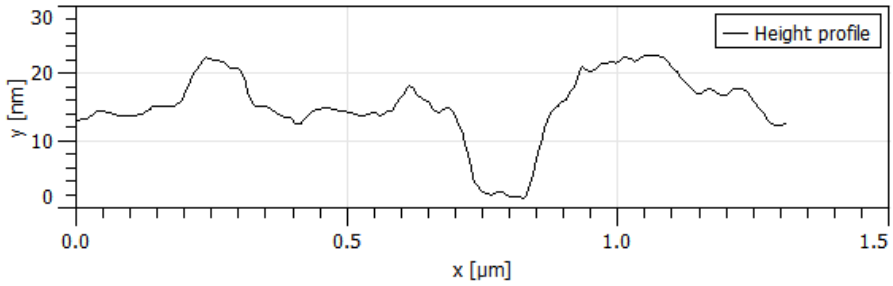

Figure 5.14: Profile height number 2 of sample W1

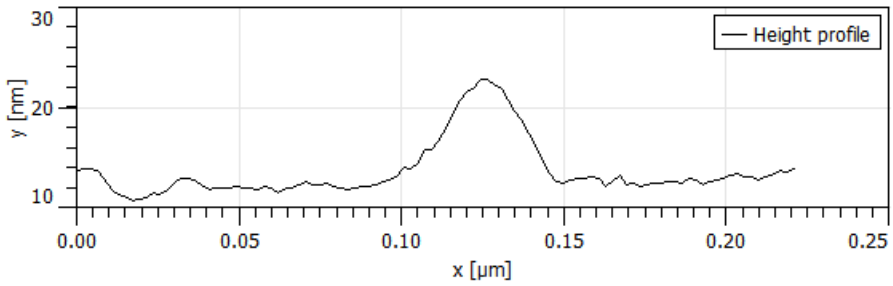

Figure 5.15: Profile height number 3 of sample W1

Sample W4

For what concerns sample W4, pictures at different scales are represented in Figures from 5.16 to 5.21. No significant difference with sample W1 can be pointed out, mean surface roughness of Figure 5.16 is 4.8 nm and also the height profile presents the same patterns. In Figure 5.22 and 5.23 we can see an edge of the graphene layer. From the height profile in Figures 5.24 and 5.25 we can appreciate that the average graphene thickness of sample W4 is around 7 nm, which is very similar to the thickness found using optical transmittance that was 6.5 nm.

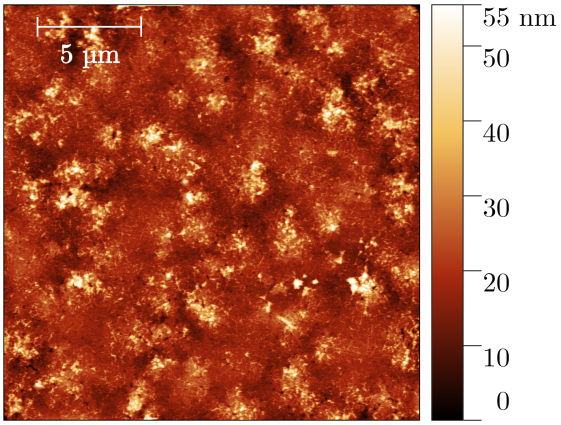

Figure 5.16: AFM scan of sample W4 5um scale

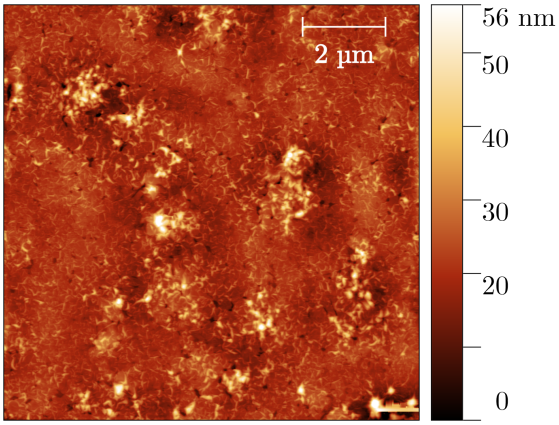

Figure 5.17: AFM scan of sample W4 2um scale

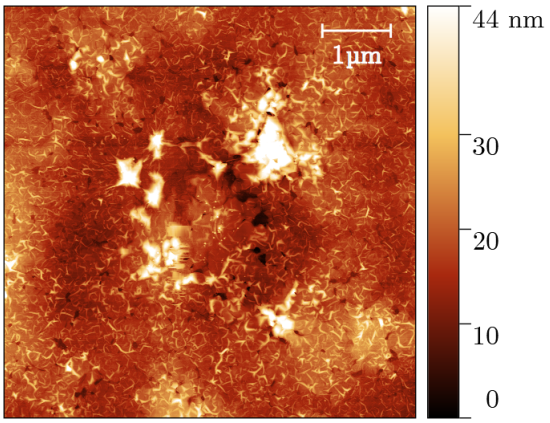

Figure 5.18: AFM scan of sample W4 1um scale

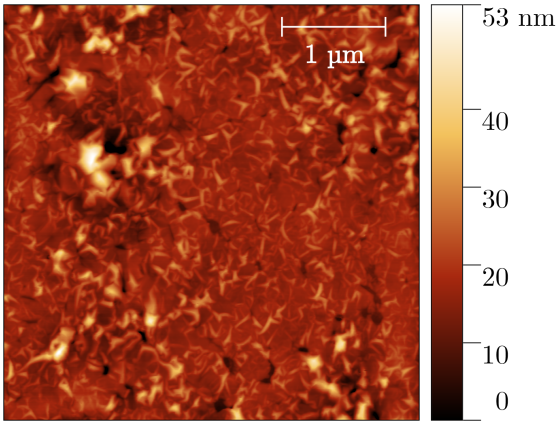

Figure 5.19: AFM scan of sample W4 500nm scale

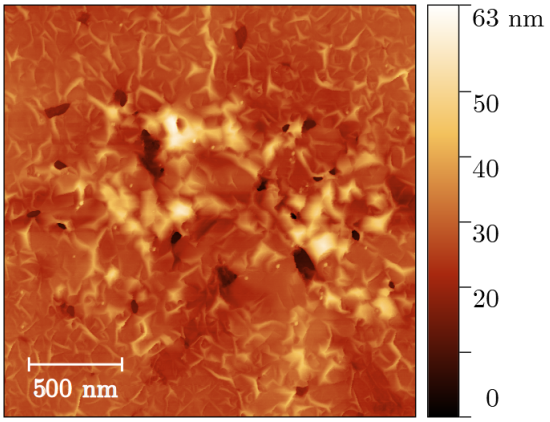

Figure 5.20: AFM scan of sample W4 1um scale

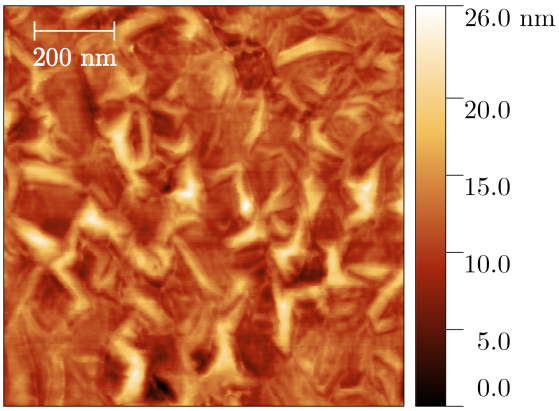

Figure 5.21: AFM scan of sample W4 500nm scale

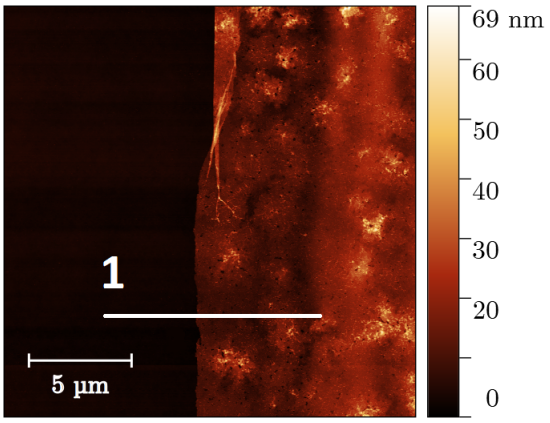

Figure 5.22: AFM scan of graphene edge on sample W4 5um scale

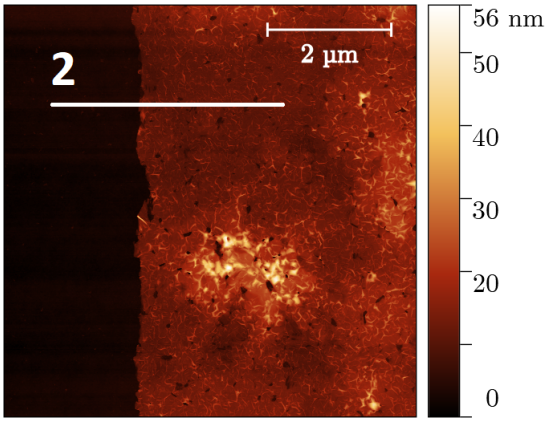

Figure 5.23: AFM scan of graphene edge on sample W4 2um scale

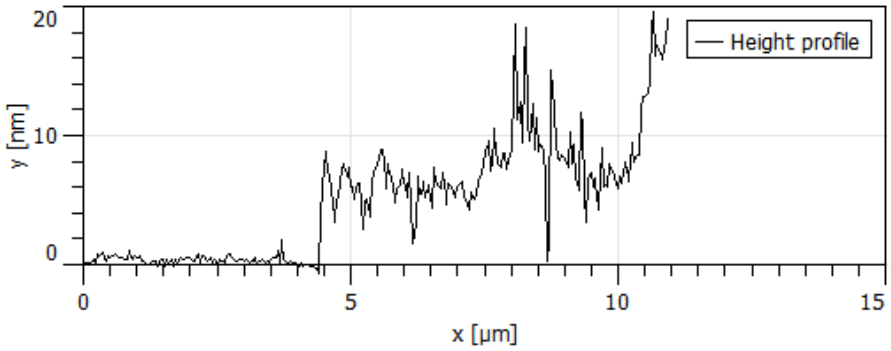

Figure 5.24: Profile height number 1 of sample W4

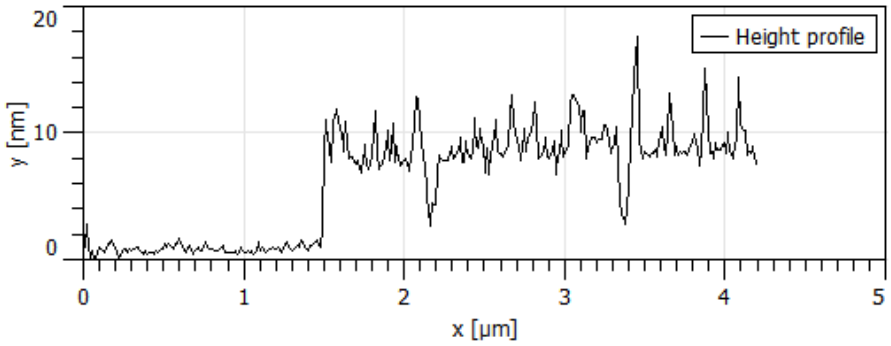

Figure 5.25: Profile height number 2 of sample W4

5.5 SiO_2/molybdenum interaction

In order to better investigate the growth process we also did an AFM characterization of the silicon oxide substrate after molybdenum etching and graphene scooping. The substrate is shown in Figure 5.27 and 5.28. In Figure 5.29 a silicon oxide film obtained by thermal oxidation is represented. In 2019 Veldhoven [66] investigated metal/dielectric interface interaction during the growth process. He found that significant deformation of the interface can occur due to surface and interface diffusion along the interface and capillary actions exerted on the substrate by the capping layer. At higher temperatures, atomic mass transport mechanisms such as surface or interface diffusion become sufficiently fast and the substrate can deform due to the vertical pull of the liquid-vapour interface. Small solid ridges can be develop at the edge of the liquid droplet, as illustrated in Figure 5.26.

Sample	Mean roughness
W1	2.28 nm
W4	1.72 nm
Native oxide	0.25 nm

Table 5.6: Silicon oxide roughness

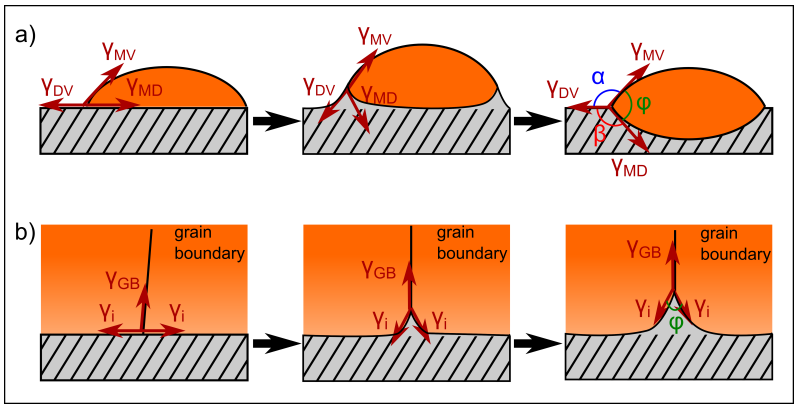

Figure 5.26: Substrate/metal interaction at high temperature during graphene grow [66]

We can point out that during out grow we had that Mo_2C interacted with the silicon oxide substrate. The silicon oxide mean roughness increases and the pattern reproduce the one of the Mo_2C grains. The silicon oxide thickness doesn't influence the process since no significant difference can be pointed out between silicon oxide substrate of sample W1 and sample W4. Surface roughness are summarized in table 5.6.

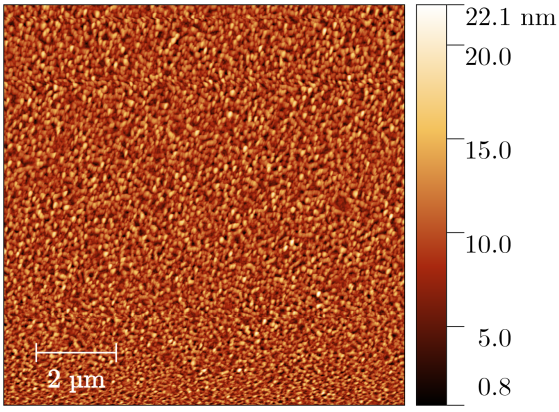

Figure 5.27: Silicon oxide substrate of W1

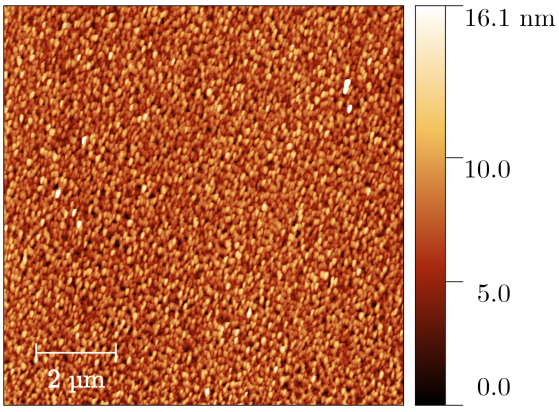

Figure 5.28: Silicon oxide substrate of W4

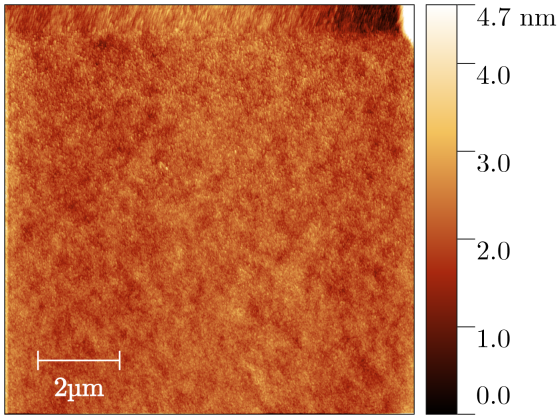

Figure 5.29: Silicon oxide by thermal oxidation

From the AFM analysis we can point out that:

- The morphology of the as-grown graphene replicate the underlying molybdenum pattern, in particular during the growth process excess carbon present in molybdenum form Mo_2C because it is thermodynamically preferred which has very small grains. Surface roughness in graphene is mainly due to metal catalyst grains.
- During the scooping process, small wrinkles are formed, they are in the order of some nanometre but since mean roughness after scooping didn't increase do not contribute much to surface roughness.
- Small holes are formed on the graphene film, and their density is almost constant all over the surface. Since their dimensions are comparable with the one of Mo_2C grains they are probably caused by a non uniform height profile of Mo_2C grains. Some grains are probably lower than the surrounding ones so in that point carbon cannot segregate causing a discontinuity in the graphene film. Alternatively, since holes are not visible when graphene is on molybdenum, holes are probably formed by grain braking during transfer.
- AFM data confirms that the estimated thickness in optical transmittance is a consistent measurement
- Graphene holes seems a good candidate to place nanoparticles, in any case the surface is very rough if compared to the graphene thickness. Using this substrate for capillary assembly could lead to a non precise deposition, particles will fill holes but will be likely also spread all around due to surface roughness. A good solution could be to increase hole depth and this could be done by etching the silicon substrate using graphene as a mask. This will be explained in the next chapter.

5.6 Optical inspection

A further inspection of sample W1 graphene on silicon oxide substrate was done using using a Zeiss optical light microscope Axioscope 5. In figure 5.30 sample W1 was imaged

with 10x magnification. Since the light come from the top, lighter areas are the one that reflects more light, so lighter regions are regions in which graphene is thicker, this is confirmed by Figure 5.31 that shows folded graphene. The white lines are probably folded graphene. These folding lines are some μm thick and they are probably caused by the scooping process. When the graphene is pulled out from the water it is no more stretched by the water surface tension, moreover gravitational force act on it while the the silicon oxide substrate is vertical and this could lead to folds. In this picture a trapped particle under graphene can also be seen. It is probably a silicon oxide particle generated during the substrate cutting.

Figures 5.32 and 5.33 show a graphene edge on silicon oxide substrate respectively with 10x and 50x magnification. From figure 5.32 we cannot see any difference with 5.30, we can see another trapped particle whereas in figure 5.33 we can point out that graphene has not an uniform colour. This means that its thickness is not uniform as also confirmed by AFM and so it reflects light differently. We can assume that the different thickness regions are related to different Mo_2C grains.

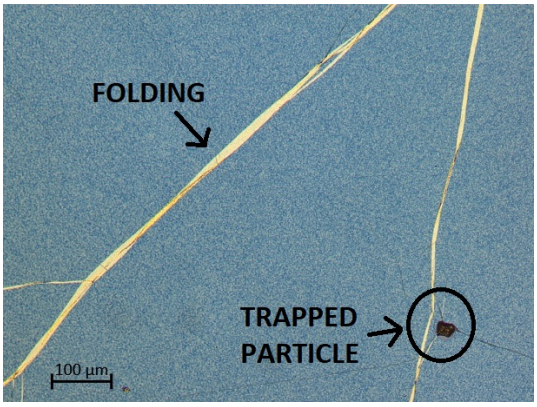

Figure 5.30: Optical image of graphene on silicon oxide

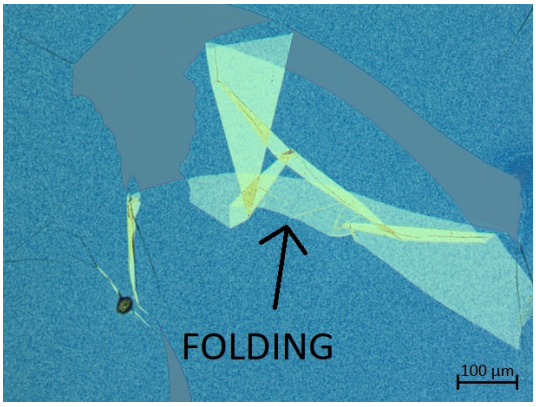

Figure 5.31: Optical image of folded graphene on silicon oxide

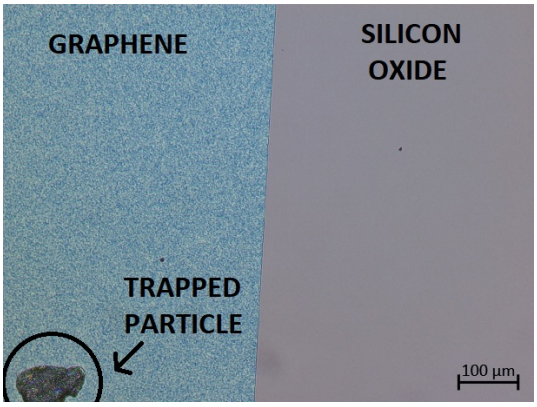

Figure 5.32: Optical image of graphene interface on silicon oxide

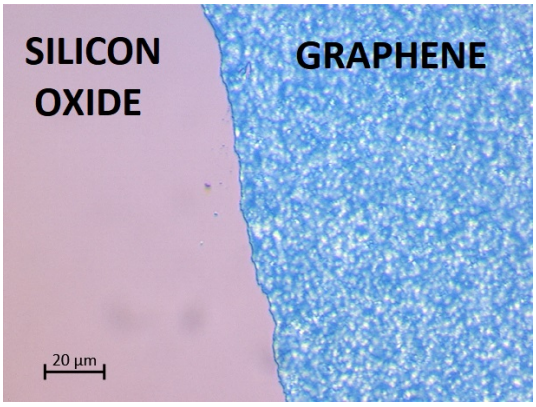

Figure 5.33: Optical image of graphene interface on silicon oxide magnified

Conclusions

In this graphene characterization chapter we confirmed the existence of graphene on metal catalyst after growth with Raman spectroscopy. We then estimate the graphene thickness using UV/visible spectroscopy and we found a thickness of several nanometre. We successively investigate the graphene using SEM, this analysis revealed holes and small wrinkles in graphene. In order to determine if holes are good candidate to place nanoparticles trough capillary assembly we did and AFM analysis of the surface morphology. This analysis revealed that graphene surface is very rough if compared to its thickness and this mainly related to the growth process. Moreover, graphene holes have not homogeneous shape or dimensions so it would be hard in this situation to obtain a selective deposition of particles with capillary assembly. In the next chapter we will try to exploit graphene as mask to etch the silicon oxide substrate. Our goal is to increase holes depth in order to guarantee a more selective deposition of particles. Finally we found that silicon oxide thickness under the metal catalyst don't influence the defects density in graphene contrarily to what Dong et al. [21] found.

Chapter 6

Graphene as etch mask

Holes and defects in the graphene film represent a good candidate to trap nanoparticles in direct assembly. Moreover their depth if compared to the lateral dimension is very low. Increasing the hole depth will allow us to trap bigger nanoparticles or to increase the trapping yield. In order to try to increase the hole depth we tried to exploit graphene as mask to locally etch away a few nm of substrate material. We cut sample W4 in different pieces and etched them using reactive ion etching (RIE). In particular we used a custom recipe made for silicon nitride that doesn't use any oxigen gases to increase selectivity against graphene, since O_2 etches it reactively. This recipe uses 25 sccm CHF_3 + 25 sccm Ar plasma @ 0.01 mbar pressure and 50 W of RF power. For silicon nitride this recipe was found to have a etch rate of 40 nm/minute. We etched four different samples respectively for: 90, 150, 180 and 300 seconds. After etching we investigated the samples using Raman spectroscopy and AFM, the results are explained in the following section.

Raman analysis

According to what Lee et al. [34] found, ion bombardment creates defects on graphene structure. This is confirmed by Raman analysis, we can see that after etching graphene is still present on the substrate and I(D)/I(G) ratio increases while I(2D)/I(G) ratio decreases for increasing etching time. Raman results are summarized in Table 6.1 and plotted in Figures 6.1 and 6.2.

Etching time	I(D)/I(G)	I(2D)/I(G)	FWHM(2D)
0 s	0.27 ± 0.02	0.93 ± 0.07	53.8 ± 2.5
90 s	1.60 ± 0.16	0.45 ± 0.12	93.9 ± 18.5
150 s	1.58 ± 0.07	0.26 ± 0.04	162.6 ± 33.4
180 s	1.50 ± 0.20	0.45 ± 0.27	103.4 ± 35.5
300 s	1.69 ± 0.37	0.29 ± 0.15	/

Table 6.1: Raman figures of merit for different etching time

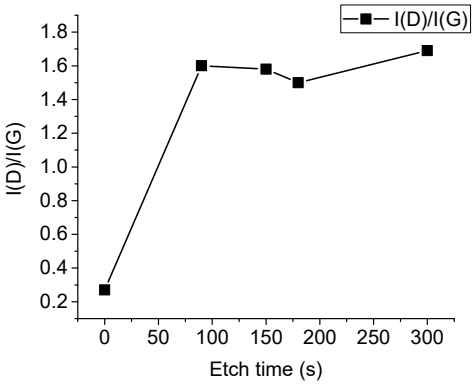

Figure 6.1: I(D)/I(G) ratio for different etching time

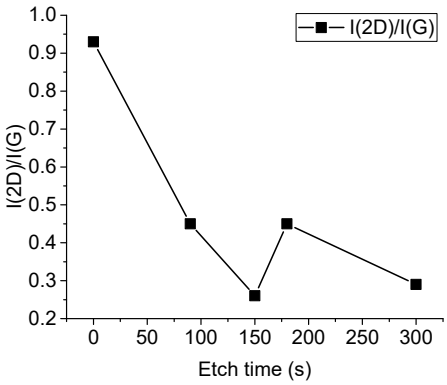

Figure 6.2: I(2D)/I(G) ratio for different etching time

AFM

From the AFM analysis we can see that mean roughness increase for increasing etch time. As example in Figure 6.4 graphene after 300 seconds etching is shown. The mean roughness is 9.8 nm, which is almost doubled with respect to the non etched sample. In Figure 6.3 graphene after 180 seconds etching is represented, whereas in Figures 6.5 and 6.6 height profile numbers 1 and 2 are shown. We can point out that the hole depth is around 20 nm, hence it has doubled with respect to the non bombarded graphene. From this measure we can estimate the etch rate of this recipe towards silicon oxide as 3.4 nm/min.

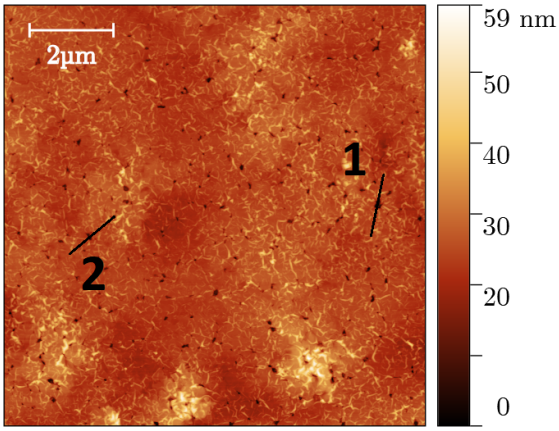

Figure 6.3: AFM scan of sample W4 after 180 s etching

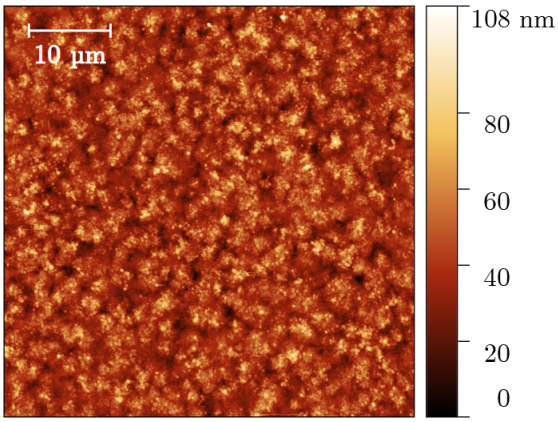

Figure 6.4: AFM scan of sample W4 after 300 s etching

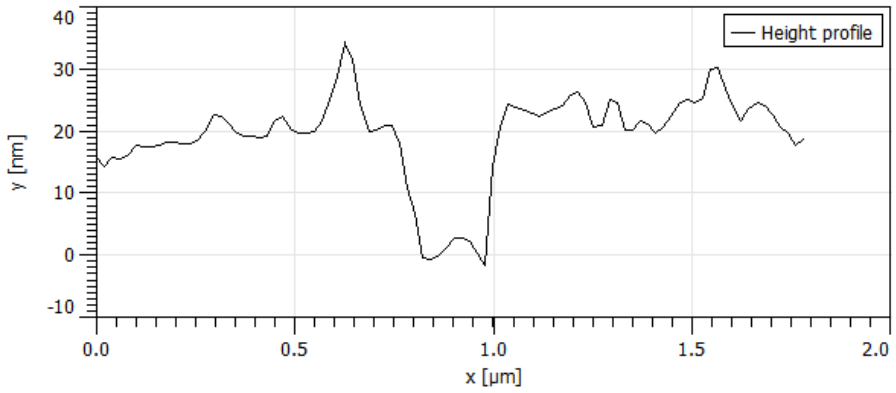

Figure 6.5: Profile height number 1 of figure 6.3

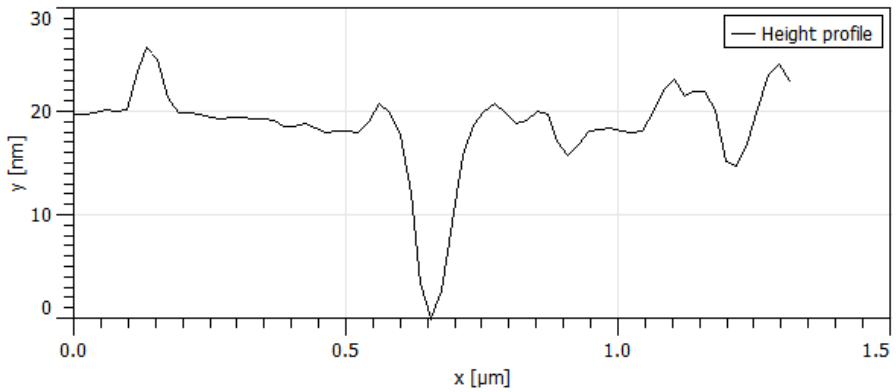

Figure 6.6: Profile height number 2 of figure 6.3

Using RIE to increase the hole depth exploiting graphene as a mask didn't improve the substrate for capillary assembly; the hole depth is increased but the surface roughness is increased even more leading to less control of the capillary assembly process. Graphene was also stripped off from each sample in order to analyse silicon oxide substrate and to check whether graphene actually acted as mask. We stripped graphene with oxygen plasma @ 1.33 mbar with 500 W RF power for 10 minutes. Raman analysis revealed that graphene was no more present on the surface but scanning the topography with AFM no particular traces of etching was revealed, Figures 6.7 and 6.8 show samples after graphene stripping after 90s and 300s of etch respectively. Probably residues from graphene stripping prevent us to see the holes. Concluding, we found that graphene can be exploited as a mask, however it's role in improving the yield of capillary nanoparticle assembly would need to be carefully assessed in future work.

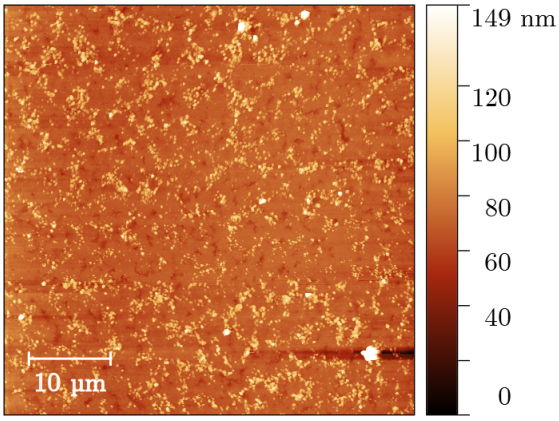

Figure 6.7: AFM scan of 90s etched substrate after graphene stripping

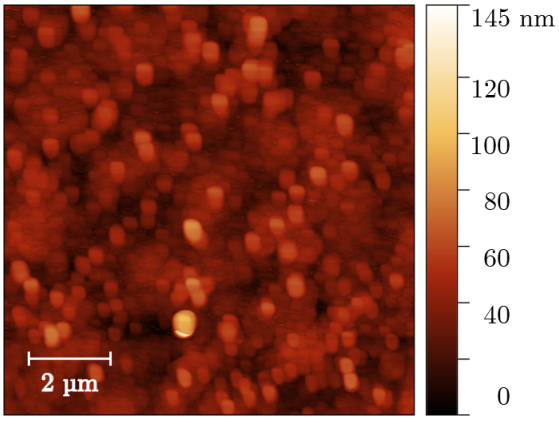

Figure 6.8: AFM scan of 300s etched substrate after graphene stripping

Chapter 7

Capillary assembly setup

The setup used for the capillary assembly is inspired by that presented in Figure 3.4. In Figure 7.1 the picture of the actual setup assembled at ECTM is reported. The main element that compose it are:

- Lateral microscope camera for contact angle measurement: used to measure the deposition angle during the experiment, a contrast light is generally used to better image the drop profile. In our case we used a Dino-Lite Capture Cam.
- Optical microscope: used to inspect the contact line and monitor the accumulation zone. In our case we used a Zeiss optical light microscope Axioscope 5 with Axiocam 105 colour and 10x and 50x magnification lenses.
- Glass slit: used to keep the particle suspension fixed and close to the substrate.
- Motorized translation stage: used to move the substrate, in our case we used PI compact line stage L-406 with a minimal incremental motion of 0.2 μm
- Peltier element: used to set the substrate temperature to precisely tune the drop evaporation rate. A brief explanation of the designed temperature controller will be done in the next section.

In Figures 7.2 and 7.3 the aforementioned parts are indicated with an arrow on the setup pictures.

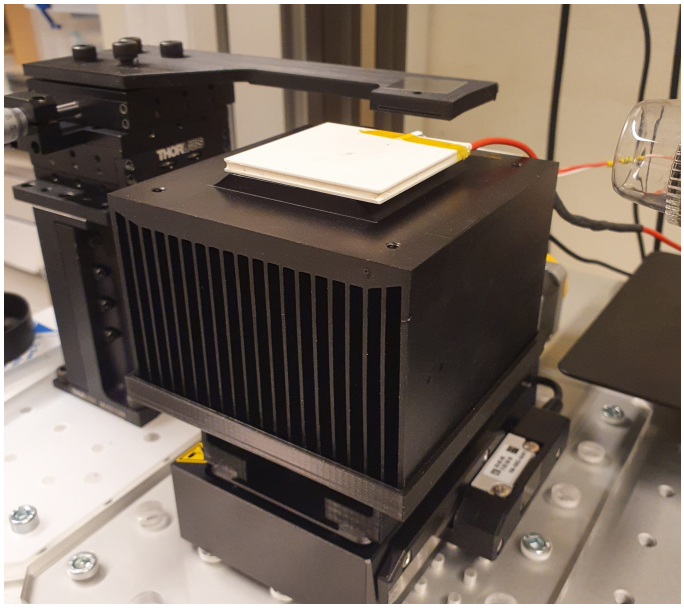

Figure 7.1: Final experimental setup

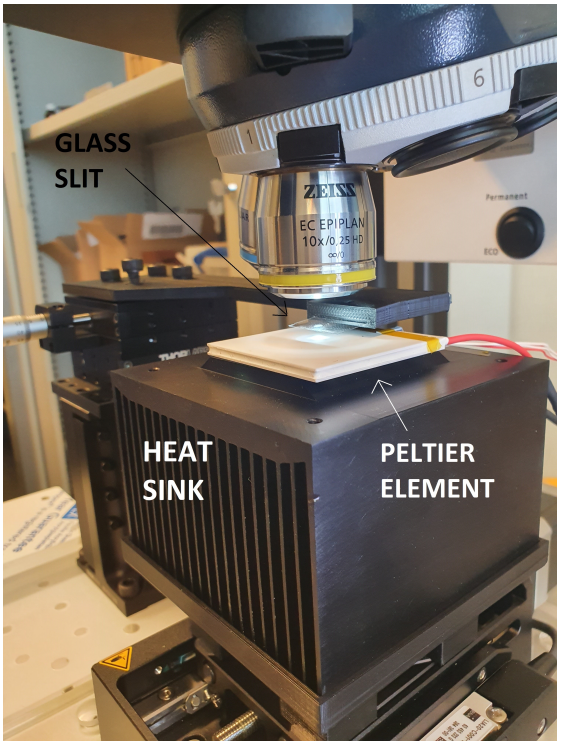

Figure 7.2: Final experimental setup

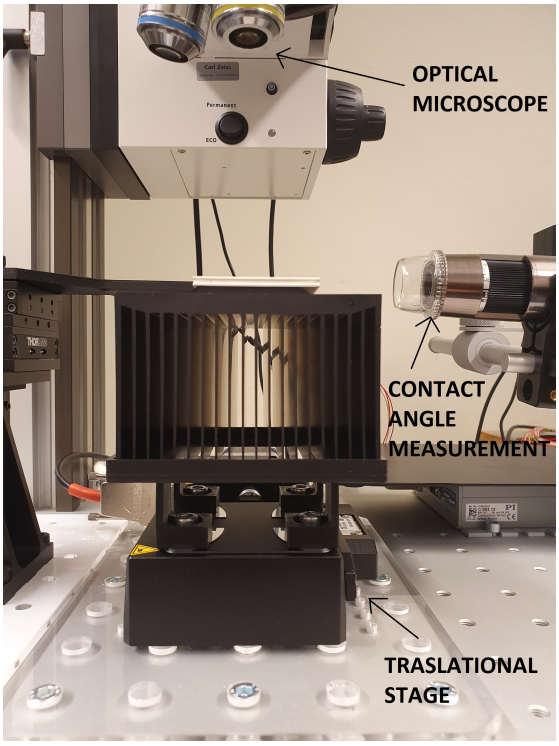

Figure 7.3: Final experimental setup

7.1 Temperature controller

Substrate temperature controller was designed and implemented in order to control the Peltier element. As explained in the literature review part, temperature is a key parameter to be controlled during assembly process to guarantee a correct evaporation rate of the solvent, and so a correct deposition rate for nanoparticles. In Figure 7.4 a schematic of the controller is represented whereas in Figure 7.5 the evaporation process is synthesized. We decided to use a Peltier cell as heating element and in order to speed up the design and fabrication process and minimize the complexity only prototype boards was used.

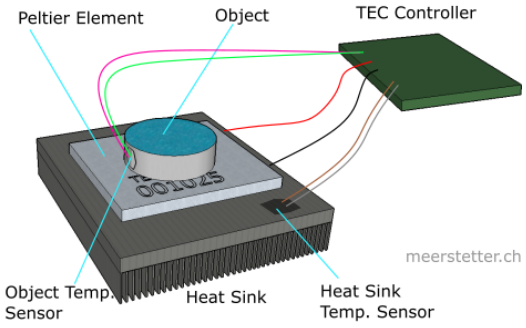

Figure 7.4: Schematic principle of the controller

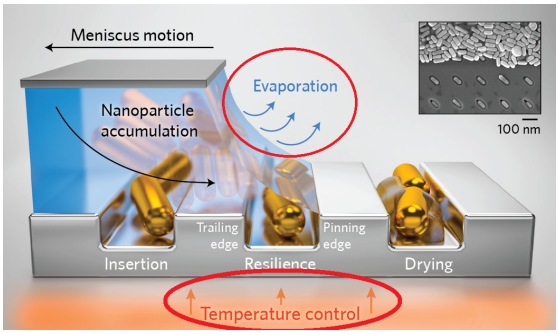

Figure 7.5: Representation of the evaporation process

The final board is depicted in Figures 7.6 and 7.7. The designed controller is able to set the substrate temperature with an accuracy of a tenth of degree. A detailed report of the temperature controller design and production is reported in Appendix A.

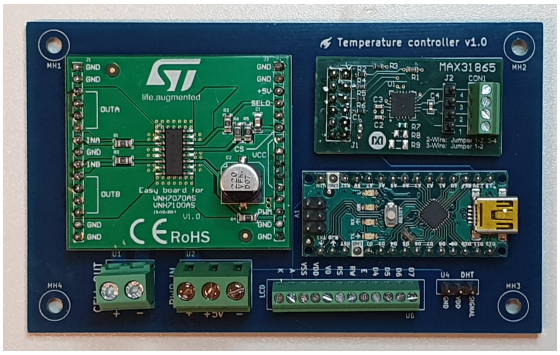

Figure 7.6: Board front

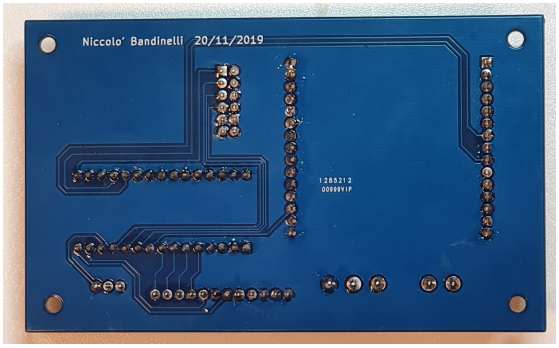

Figure 7.7: Board back

7.2 Contact angle measurement

In order to qualitatively investigate the wetting behaviour of our substrate we performed a contact angle measurement. We used two test liquids: water because it is a standard liquid for these kind of measurement and cetyl trimethyl ammonium bromide (CTAB) solution at its critical micelle concentration (CMC, 0.9 mM) that is the solution in which nanopar-

ticles will be suspended. CTAB is an ammonium surfactant used to stabilize nanoparticle in the colloidal suspension. We investigated three different substrates: standard thermal silicon oxide, graphene on silicon oxide after scooping and silanized graphene on silicon oxide. Silanisation is a surface coating process, in this case performed from vapour phase, whereby a self-assembled monolayer (SAM) composed of macromolecules containing siloxane groups is covalently and conformally deposited over the substrate. The goal of this process is to change the substrate wetting behaviour. In particular in our case we used trichloro(1H,1H,2H,2H-perfluorooctyl)silane which has CF_3 head group that make the surface more lyophobic. The silanization process was developed in a vacum chamber.

Water

In table 7.1 the different contact angle for water are reported. For each sample five measurements were taken and they are reported as mean value ± standard deviation. In Figures 7.8, 7.9 and 7.10 the picture of the aforementioned measurements are reported.

Substrate	**Contact angle**
SiO_2	46.0 ± 2.9
Unsilanized graphene	84.3 ± 3.3
Silanized graphene	108.1 ± 3.8

Table 7.1: Water contact angle on different substrates

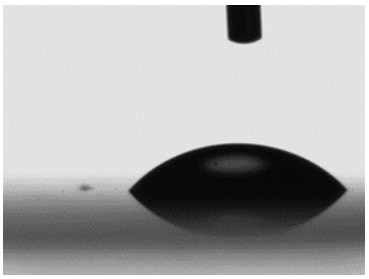

Figure 7.8: Water drop on silicon oxide

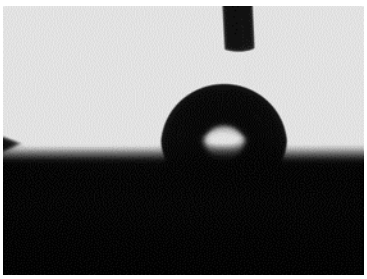

Figure 7.9: Water drop on graphene

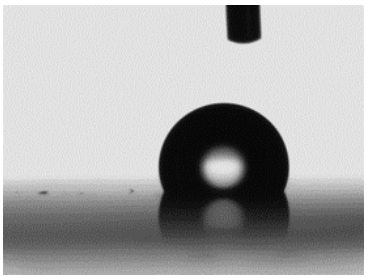

Figure 7.10: Water drop on silanized graphene

CTAB

In table 7.2 the different contact angle for CTAB are reported. Also in this case for each sample five measurements were taken and they are reported as mean value ± standard deviation. In Figures 7.11, 7.12 and 7.13 the picture of the aforementioned measurements are reported.

Substrate	Contact angle
SiO_2	51.6 ± 3.0
Unsilanized graphene	40.6 ± 1.1
Silanized graphene	102.1 ± 1.0

Table 7.2: CTAB contact angle on different substrates

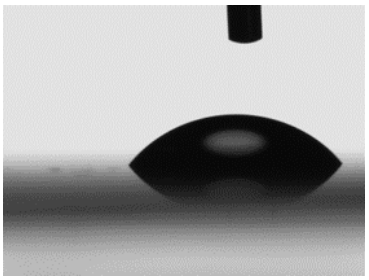

Figure 7.11: CTAB drop on silicon oxide

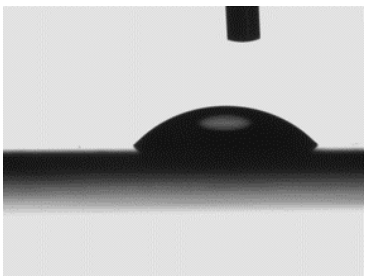

Figure 7.12: CTAB drop on graphene

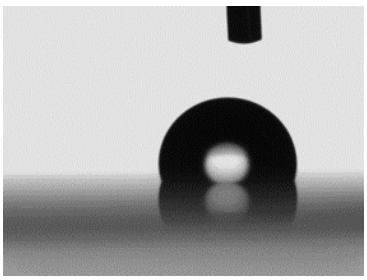

Figure 7.13: CTAB drop on silanized graphene

7.3 Setup test

After completing the setup preparation we simulated the assembly on graphene substrate using both water and CTAB. For both liquids we recorded the deposition angle in steady state and we highlight some phenomenon that happened in our experiments. The substrate temperature for all the next experiments was set to 30 °C.

Water

By simulating the assembly with a water drop we found that at a speed of 10 μm/s the deposition angle when the steady state is reached is 39°. Deposition angle for water is represented in Figure 7.14. During the assembly with water we also found pinning problems. This is represented in Figure 7.15, as can be seen the drop pins in a graphene discontinuity on the substrate and is stretched, its contact line stops receding stopping the deposition. This situation must be avoided. In Figure 7.16 we can see graphene detaching from the substrate, water penetrate between graphene and silicon oxide substrate detaching it. This is unwanted and it probably happens because of some moisture residues between graphene and silicon oxide after scooping. A baking process for 4 hours at 200 °C after scooping transfer was able to solve this problem. In Figure 7.17 we can see contact line pinning in a big dust particle. We found that scooping process leaves some dust particles trapped between graphene and the silicon oxide substrate. When the receding contact line meet one of these large particles, probably we have a big release of nanoparticle in that region with a temporary alteration of the accumulation zone.

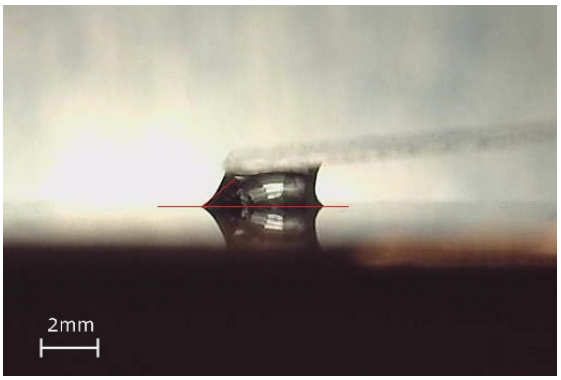

Figure 7.14: Water deposition angle in steady state condition

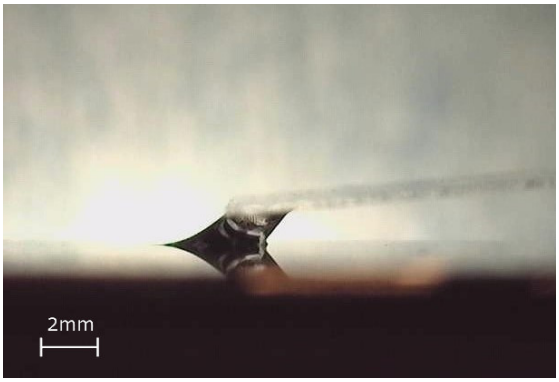

Figure 7.15: Water drop pinned on substrate

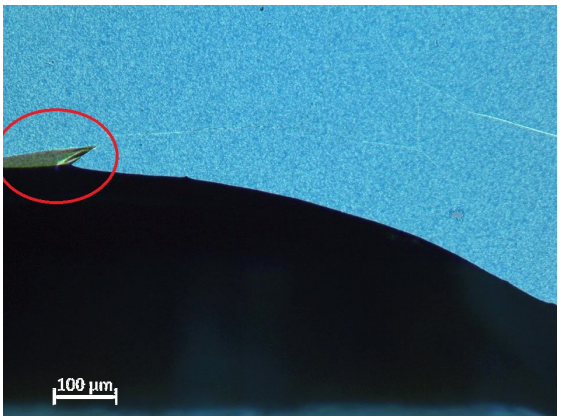

Figure 7.16: Graphene delamination with water drop

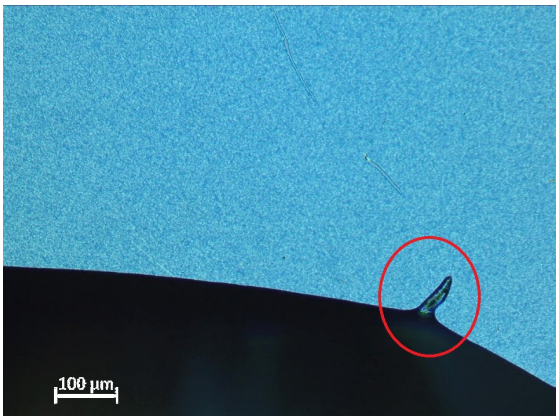

Figure 7.17: Dust particle pinning of water drop

CTAB

By simulating the assembly with CTAB drop we found that at a speed of 10 μm/s the deposition angle when the steady state is reached is 25°, from the contact angle measurements we expected a lower deposition angle with respect to water. Deposition angle for CTAB is represented in Figure 7.23, the lower deposition angle can be appreciated also from the microscope image, the receding contact line is thinner with respect to the one of water and so allow us to see the substrate. In Figure 7.18 we can see that when graphene is scratched and the CTAB is in contact with silicon dioxide the contact angle is lower according to the previous measurements. In Figure 7.19 we can see that the different coloured lines parallel to the contact line means that CTAB receding line has a non uniform height as expected. In Figures 7.20 and 7.21 we can see pinning on a dust particle with 50x magnification. As it also happened with water here the dark region in front of the dust particle confirm that we have a discontinuity in the accumulation zone with a consequent release of a big amount of particles. In this case the dark area is caused by a deposition of CTAB micelles. A small amount of CTAB is stacked on the substrate

by the dust particle, the fast evaporation of water leads to an increase of surfactant concentration that leads to the formation of micelles that precipitates on the substrate. The same phenomenon can be appreciated in Figure 7.22 when we deliberately increased te substrate temperature up to 35 °C. Due to the higher temperature the surfactant concentration in the accumulation zone increase, micelles are formed and then periodically released on the substrate.

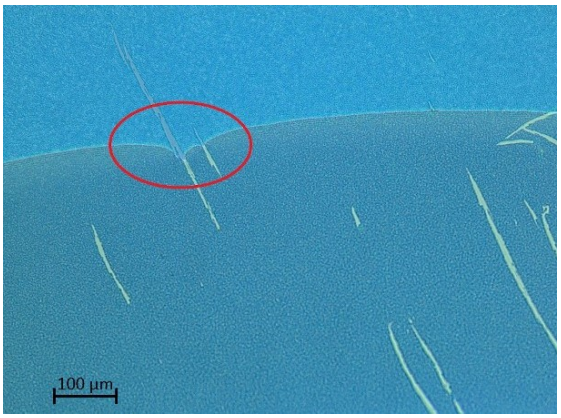

Figure 7.18: CTAB receding line present different angle

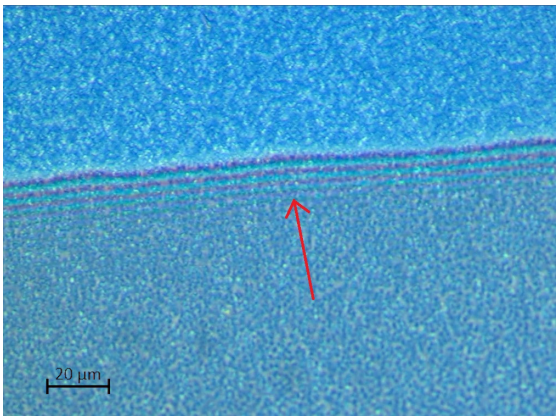

Figure 7.19: CTAB receding line presents different thickness

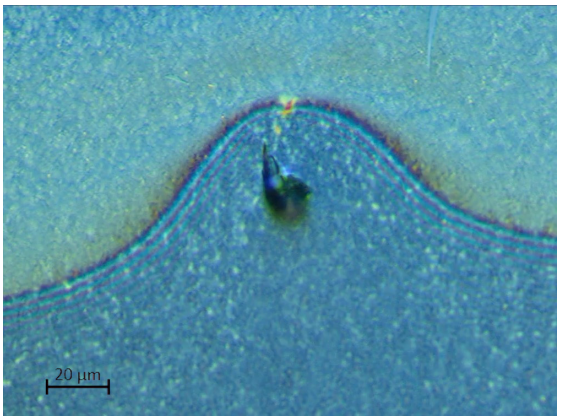

Figure 7.20: CTAB drop pin in particle 1

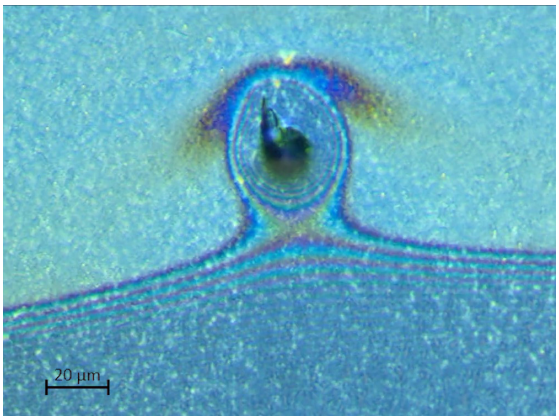

Figure 7.21: CTAB drop pin in particle 2

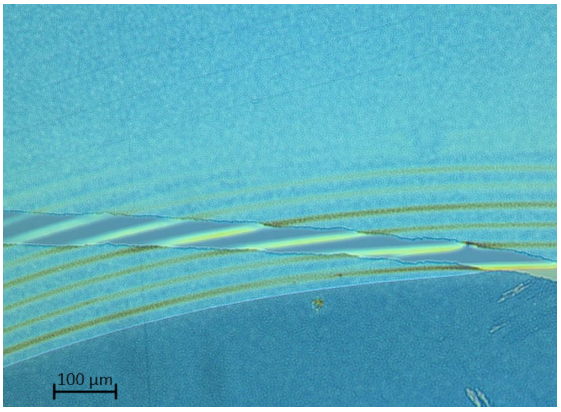

Figure 7.22: Micelles precipitation due to a substrate temperature increase

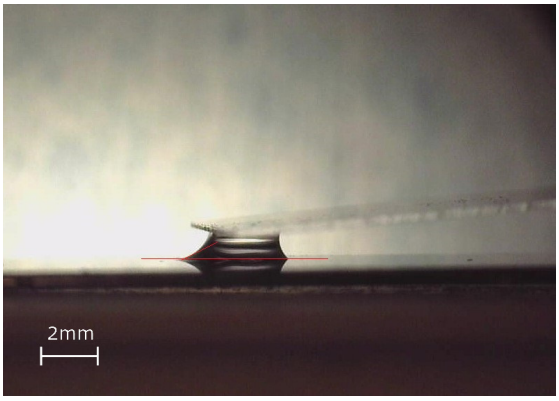

Figure 7.23: CTAB deposition angle in steady state condition

In order to exploit capillary assembly of nanoparticles we decided to buy gold nanoparticles from Nanopartz (USA), we choose particles with 15 nm of mean diameter. The particles were shipped in a stabilized solution of deionized water and CTAB with a particle concentration of 1.91 $\cdot 10^{12}$ nps/mL, the particles product code is A11-15-CTAB-DIH-1-10. Particles were processed before the assembly, the as-purchased suspension were centrifuged twice for 10 min at 15000 rpm in 2 ml of CTAB solution at its critical micelle concentration (CMC, 0.9 mM) to control the supernatant properties. Fifty microlitres of the resulting concentrated solution was sonicated for 10 min and used in assembly experiments immediately after preparation. The thickness of the adsorbed CTAB monolayer (3 nm) extends the effective interaction radius of the suspended nanoparticles, resulting in an actual diameter of around 20 nm. Some assembly tests with nanoparticles suspension were carried out on the setup, but due to covid19 outbreak I was not able to analyse the results. These samples are not conclusive and need to be further investigated.

Part IV

Conclusion

Chapter 8

Final comments and future perspectives

This thesis work started from the hypotheses that defects on graphene caused by CVD growth on molybdenum catalyst could be a good candidates to trap nanoparticles with capillary assembly. Trapping metal nanoparticles in graphene gas sensor defects could lead to increase their sensitivity and selectivity towards different gas species.

After graphene growth on molybdenum catalyst and transfer on another substrate, we characterized it with Raman spectroscopy, UV/Visible spectroscopy, SEM and AFM. From the Raman analysis we proved the existence of graphene, while from UV/Vis analysis we estimated the number of graphene layers. From SEM analysis we found out that graphene presents some small wrinkles and holes on its surface that could be good candidate to trap nanoparticles in capillary assembly, finally with AFM we investigated more in detail the surface morphology finding that graphene surface is very rough if compared to its thickness. We confirmed that roughness and holes are formed during the growth process on molybdenum, in particular they are due to the Mo_2C formation for the excess of carbon in the catalyst. We also found out that silicon oxide thickness under the molybdenum catalyst don't influence the density of defects.

We tried to increase the hole depth by using graphene as etch mask to etch the silicon oxide substrate. We found that graphene can be exploited as a mask, however it's role in improving the yield of capillary nanoparticle assembly would need to be carefully assessed in future work. Finally we set up and tested the capillary assembly instrumentation designing and building the temperature controller for the substrate. First assembly experiments on graphene confirm that the wetting behaviour of graphene and CTAB nanoparticle suspension is good and it worth to do some assembly to see where the nanoparticles will be trapped on the substrate. This was not done in this work due to covid19 outbreak.

Part V

APPENDIX A: Substrate temperature controller

Technical Univeristy of Delft

Substrate temperature controller for direct assembly setup v1.0

Niccolò Bandinelli
Delft, January 21, 2020

Contents

Chapter 1

Introduction

The aim of this project was to design and implement a temperature controller for a direct assembly setup. Temperature is a key parameter to be controlled during assembly process to guarantee a correct evaporation rate of the solvent, and so a correct deposition rate for nanoparticles. The design procedure has been carried out with the following steps:

1. Components selection
2. Controller design
3. PCB design
4. Final test

The **design specifications** are the following:

- Heating up to 50 °C
- Heating and cooling rate in the order of 20-30 °C/min
- Minimum area of 2x2 cm^2

In order to speed up the design and fabrication process and minimize the complexity, surface mount technology (SMT) components has not been used, only prototype boards has been used.

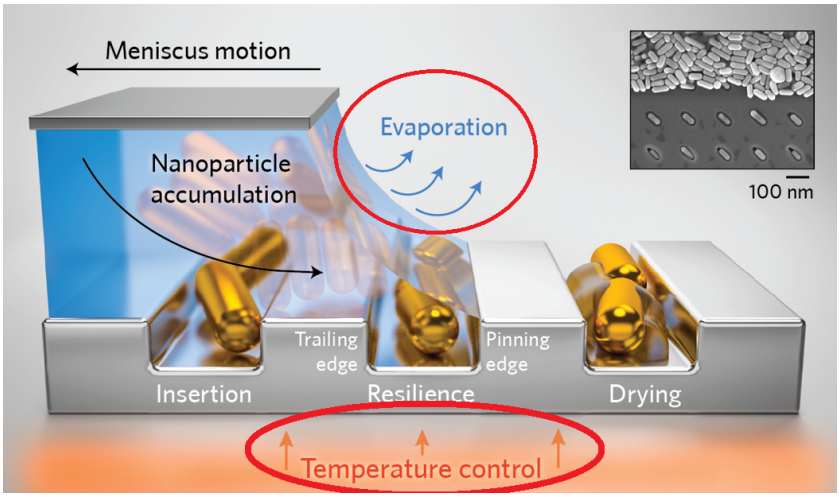

Figure 1.1: Direct assembly process illustration

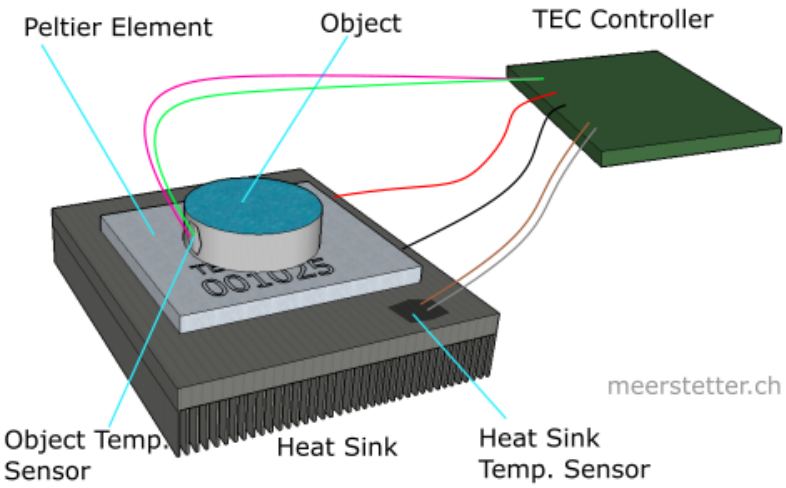

Figure 1.2: Scheme of the desired setup

Chapter 2

Components selection

All the components have been selected according to the specifics of the project and bought from Farnell NL. The parameters taken into account during the components selection are: performance, cost, market availability and delivery time.

2.1 Heating element

A Thermoelectric cooling cell (TEC) has been chosen as heating element. It is capable of both heating and cooling the substrate leading to a better and more precise control of the temperature. In particular the TEC MCTE1-19913L-S from Multicomp has been selected. It is 50x50mm and can transfer power up to 200W as shown in figures 2.1 and 2.2.

The cell will be directly powered by the PWM signal from microcontroller. This method is not the most efficient according to [3] but it is easiest to realize and it doesn't require filters nor expansive DC controllers.

Parameters		
Internal resistance	1.4Ω ±10%	
I max.	13A	
V max.	24.1V	
-	Th = 27°C	Th = 50°C
Q max.	200W	224W
ΔT max.	68°C	75°C
Solder melting point	138°C	
Maximum compress	98.07N / cm^2 (10kgf / cm^2)	

Figure 2.1: Maximum ratings for TEC cell

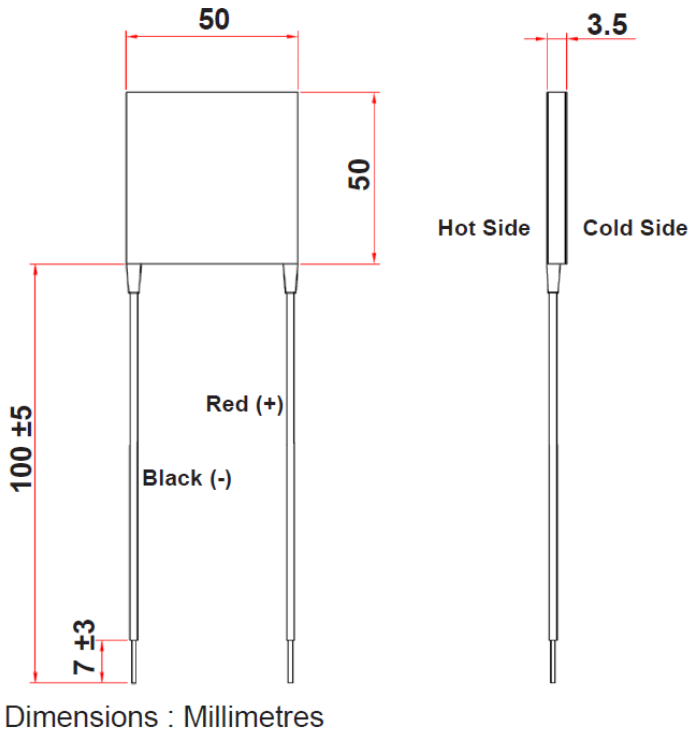

Figure 2.2: Mechanical specifications of TEC cell

2.2 Controller

Arduino Nano board has been chosen as controller because it is one of the best prototyping board. It is really small, easy to program and powerful enough to run our temperature controller. Arduino Nano board is based on an old Atmel328 microcontroller which provides:

- 8 analog input pins
- 10 bit adc
- 22 digital output (of which 6 are for PWM)
- 32kb of flash memory

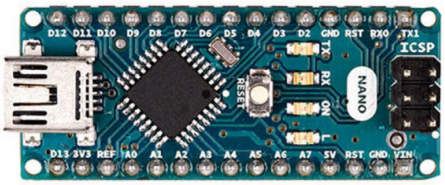

Figure 2.3: Arduino Nano

2.3 Power controller

The power controller is in charge to amplify the small current signal coming out from the digital microcontroller output pin (that is in the order of few mA) to a more higher current (few ampere) able to control the TEC element. A single MOS transistor is enough to amplify the digital output signal, but it can only control the current flow in one direction. In order to be able to both heat and cool the cell we should be able to control also the current flow direction. This could be easily done with 4 MOS transistors connected in a h-bridge structure like shown in figure 2.4. There are plenty of h-bridge IC available on the market designed for DC motors control, the EV-VNH7070AS evaluation board from ST microelectronics was chosen. It mounts a VNH7070AS IC which can receive a PWM signal as input between 0 and 20kHz frequency.

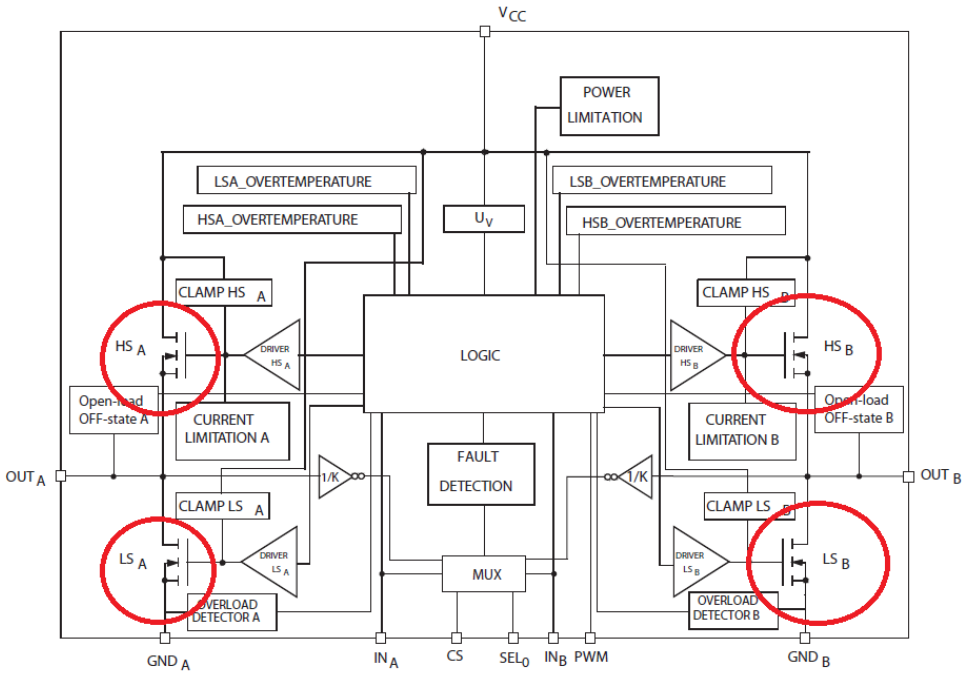

Figure 2.4: Block diagram of VNH7070AS IC

Figure 2.5: Picture of the VNH7070AS evaluation board

2.4 Temperature sensor

In order to detect the temperature in the range of [10-80]°C we decided to use a Resistance Temperature Detector (RTD), in particular a Pt100 resistor. A Wheastone bridge network with a precision amplifier is needed in order to read out the resistance value. Moreover the 10 bits of Arduino ADC are not enough to get high resolution measurements. For these reasons we decided to buy the MAX31865PMB1 prototype board that mount a Maxim MAX31865 IC specifically designed to read out Pt100/1000 resistance value. It integrate a 15bit ADC so can reliably communicate digitally (SPI) with our microcontroller. This IC is able to read both 2,3 or 4 wires sensors, we decided to buy a 4 wire thermocouple which is the best configuration to avoid measurements errors due to parasitic wires resistance. The total overall accuracy declared by the datasheet is 0.5 °C.

2.4.1 Read out

A platinum RTD transfer function is described by the Callendar–Van Dusen equation that consists in two distinct polynomial equations: one for temperatures below 0°C and another for temperatures above 0°C. These equations are:

$$R_{RTD}(t) = R_0[1 + At + Bt^2 + C(t-100)t^3] \quad \text{for} \quad t \leq 0°C \tag{2.1}$$

$$R_{RTD}(t) = R_0[1 + At + Bt^2] \quad \text{for} \quad t \geq 0°C \tag{2.2}$$

with:

- t = RTD temperature [°C]
- $R_{RTD}(t)$ = RTD resistance as a function of RTD temperature (t)
- R_0 = RTD resistance at 0°C (most often 100°C)
- $A = 3.9083 \cdot 10^{-3}[°C^{-1}]$
- $B = -5.775 \cdot 10^{-7}[°C^{-2}]$
- $C = -4.183 \cdot 10^{-12}[°C^{-4}]$

In figure 2.6 the block diagram of the interfacing circuit is represented. This configuration uses a voltage divider consisting in R_{REF} (a reference resistance with ±1% tolerance) and R_{RTD} connected to the reference voltage of the ADC. In this way we can measure the ratio between R_{RTD} and R_{REF} that is independent from voltage supply value and uncertainty. Using this configuration, the uncertainty of this measure mainly depend on R_{REF} uncertainty (±1%).

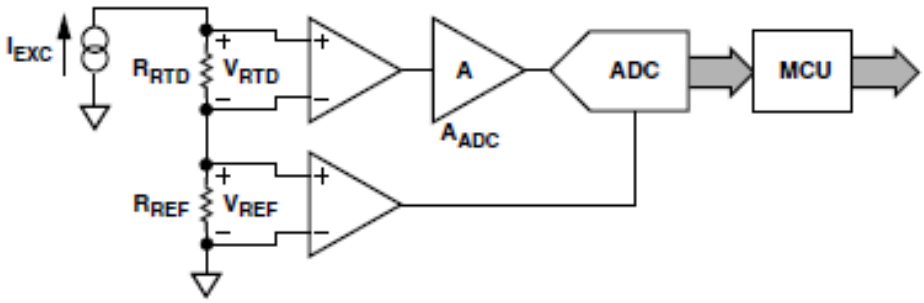

Figure 2.6: RTD Interfacing Hardware Configuration

In order to obtain the resistance value $R_{RTD}(t)$ from the ADC read out we apply the formula:

$$R_{RTD} = ADC_{norm} \cdot \frac{R_{REF}}{2^{15}} \tag{2.3}$$

Than the temperature is computed according to the direct mathematical method of [1] that is very accurate and doesn't require any look-up table.

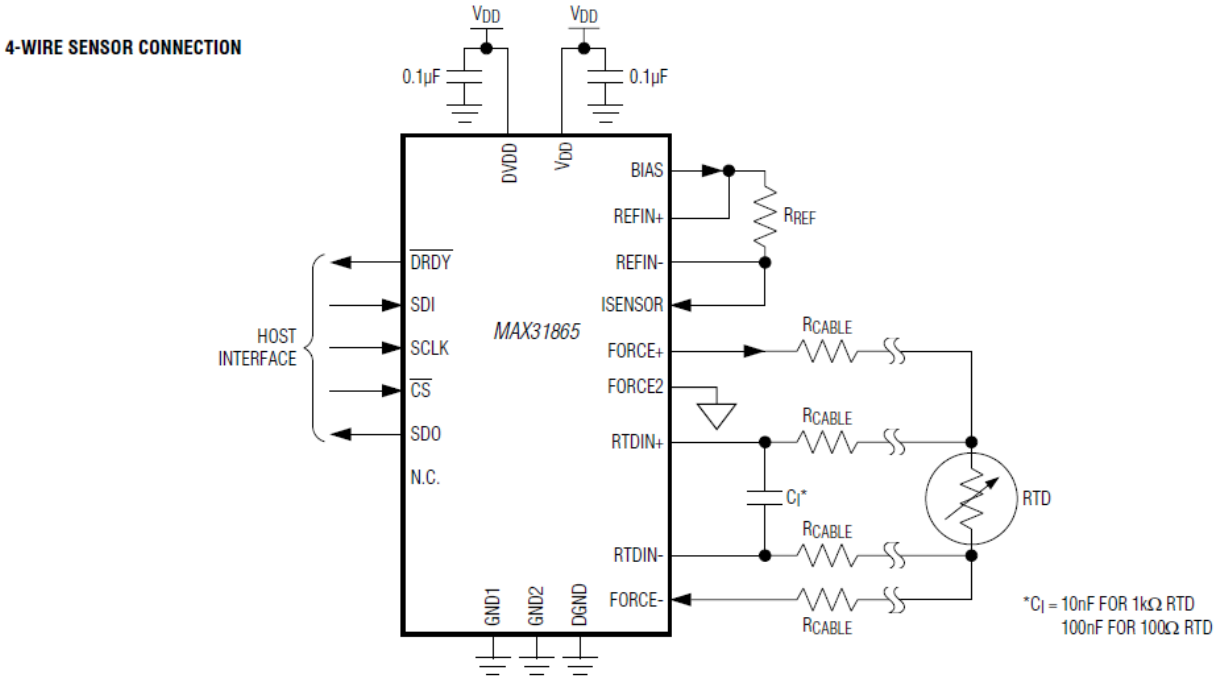

Figure 2.7: MAX31865 schematic with RTD probe

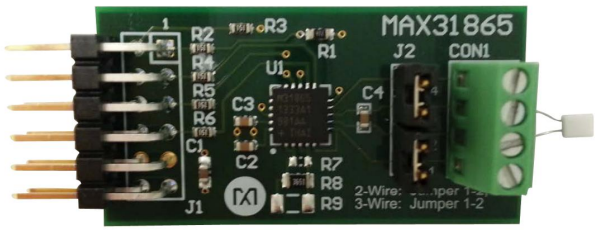

Figure 2.8: Picture of the MAX31865PMB1 board

2.5 LCD display

The LCD display is an external peripheral that allow us to know the system status and the system parameters like substrate temperature and set temperature when the controller is not connected to the computer trough the serial port. The MIDAS MC21605A6WD 16x2 characters has been chosen. In figure 5.4 the LCD displaying the parameters can be seen.

2.6 External T/H sensor

A external temperature and humidity sensor directly connected to the controller board has been added in order to evaluate the atmosphere dew point that is the temperature at which the flux between incoming and outcoming molecules form the water drop is balanced. The DFR0067 board has been chosen, it mounts a Sensirion DHT11, one of the most cheap and famous T/H digital sensor. The dew point inside the controller is evaluated with the Magnus-Tetens approximation:

$$T_d = \frac{b\ \alpha(T, RU)}{a - \alpha(T, RU)} \tag{2.4}$$

$$\alpha(T, RU) = \frac{a\ T}{b + T} + \ln(RU) \tag{2.5}$$

with: a = 17,27 e b = 237,7 °C, valid in the interval:

- T (measured temperature): 0 °C < T < 60 °C
- RU (relative humidity): 1 < RU < 1,00 %
- T_d (dew point): 0 °C < Td < 50 °C

Figure 2.9: DHT11 external sensor

2.7 Power supply

The power voltage has been chosen to be 5v. This voltage is enough to deliver the required power to the TEC element (according to the datasheet) and was the optimal choice because it allow us to power both the circuitry and the TEC with the same voltage without requiring expansive and bulky voltage regulators. A commercial 5v power supplier with 5 A of maximum current has been chosen to power the entire system.

Chapter 3

Controller design

A simple PID (proportional, integral, derivative) controller has been implemented in order to regulate the temperature. The block diagram of a PID controller is depicted in figure 3.1. It is a control loop mechanism employing feedback that is widely used in industrial control systems and a variety of other applications requiring continuously modulated control. A PID controller continuously calculates an error value e(t) as the difference between a desired setpoint and a measured process variable (the substrate temperature in our case) and applies a correction based on proportional, integral, and derivative terms. The PID parameters represent respectively:

- **P:** proportional control, apply a control signal proportional to the difference between the setpoint and the actual value (error function)
- **I:** integral control, apply a control signal that is proportional to the integral of the error function in the previous time intervals, it acts like a "memory".
- **D:** derivative control, apply a control signal proportional to the derivative of the control variable, it measure the changing rate of the control variable, in this way is possible to have fast response for fast variation of the controlled variable.

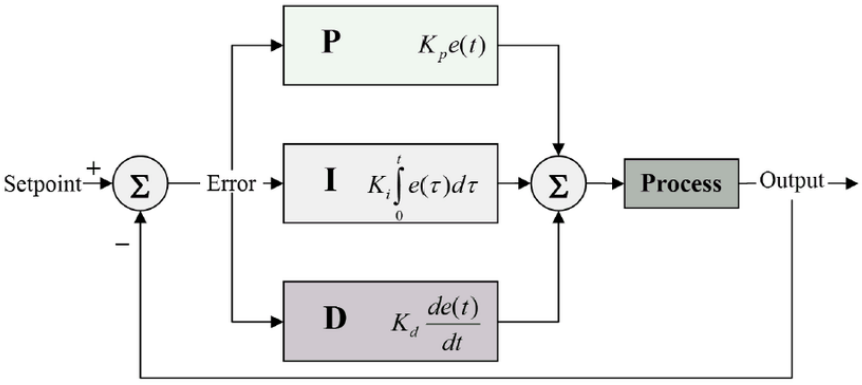

Figure 3.1: PID controller block diagram

The control variable is evaluated by the following formula:

$$u(t) = K_{\mathrm{p}} e(t) + K_{\mathrm{i}} \int_0^t e(\tau)\,d\tau + K_{\mathrm{d}} \frac{de(t)}{dt} \tag{3.1}$$

3.1 PID tuning

In order to obtain a stable control, optimal values for the P,I and D parameters must be found in order to:

- Minimize the time response
- Minimize the overshoot

There are several standard tuning procedures like the Ziegler–Nichols method. Since this process has a very fast response a try and error method has been adopted. The P parameter was tuned first with D = 0 and I = 0. Several values were tested and P = 40 was chosen as the optimal parameter according to the response. Than the I parameter was varied finding a minimal overshoot for I = 5. Finally varying the D parameter, no significant difference were found, so D = 0 was chosen. This is reasonable since the process to be controlled is slowly varying. In table 3.1 the final PID parameters are summarized.

P	**I**	**D**
40	5	0

Table 3.1: Summary of PID parameters

In this controller there are two control parameters:

- **Target temperature:** is the desired temperature for the substrate.
- **Set temperature:** is the temperature setpoint on the controller at time t.

As soon as a new *target temperature* is set by the user, the *set temperature* of the controller is gradually updated at 1 °C/s speed until it equals the *target temperature*. This minimize the overshoot errors. In figure 3.2 a test time response of the controller is shown for different values of the Target temperature.

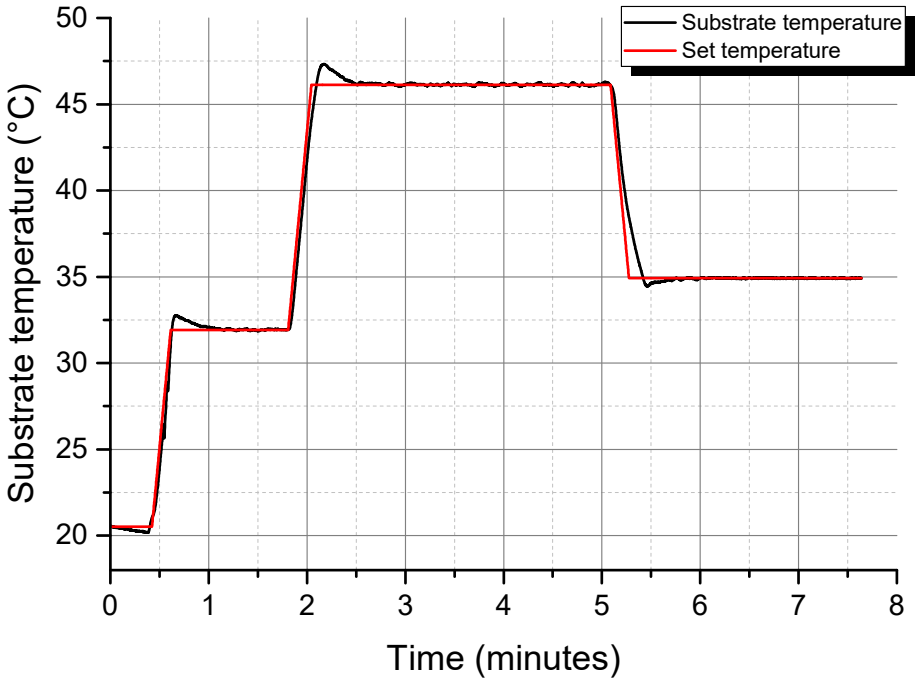

Figure 3.2: Controller test with ramps

Chapter 4

PCB Design

Once the controller has been designed and tested using a breadbord. We proceed to design a PCB. The design has been made using the open source software KiCad, the board has been designed in two different steps: schematic design and board layout.

4.1 Schematic design

In order to draw the schematic, a symbol for each component of the board is needed. KiCad library includes Arduino Nano symbol, whereas a custom symbol has been created for the: LCD connector, power controller, temperature sensor, power and cell connector.

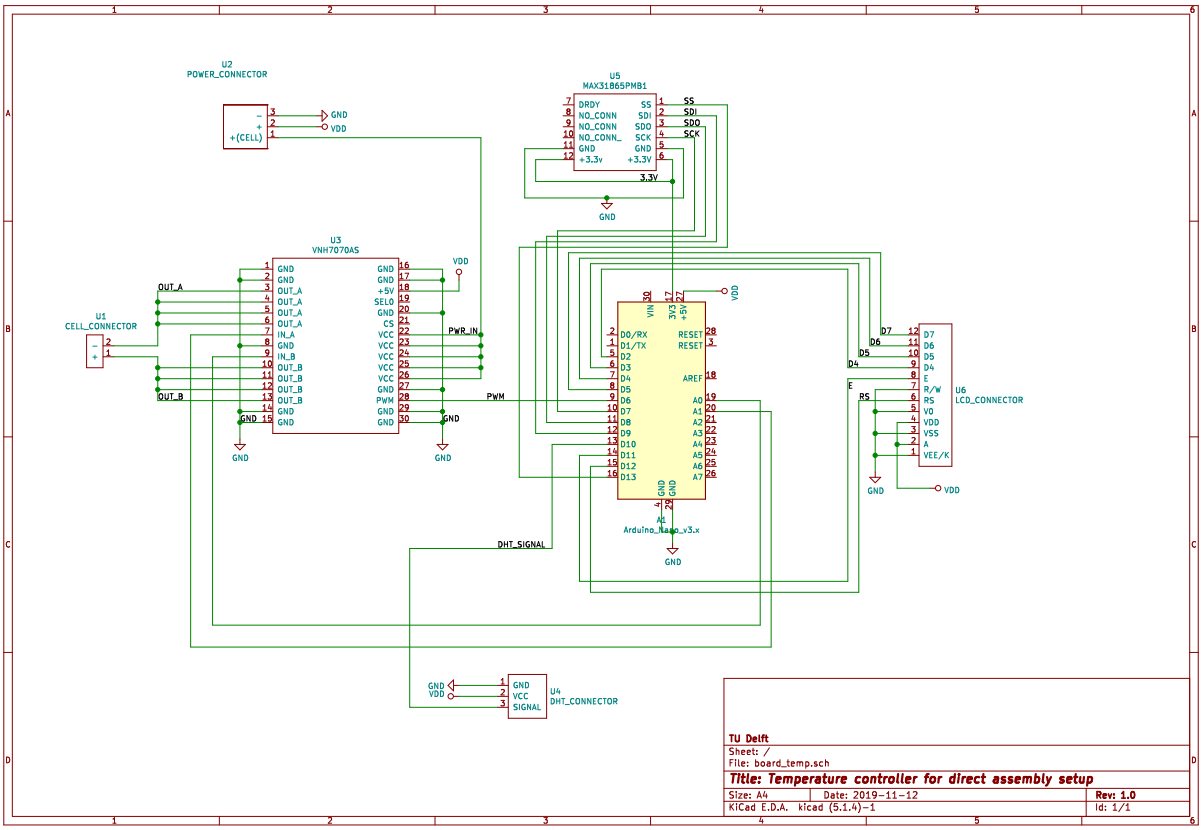

Figure 4.1: Board schematic

4.2 Board layout

Each symbol has an associated footprint: a footprint is the arrangement of pads (surface-mount technology or through-holes) used to physically attach and electrically connect a component to a printed circuit board. The footprint for Arduino Nano was already present is KiCad library while the footprint for the custom boards has been created manually with the *Footprint Editor* Tool. Finally all the footprints were positioned on the board to minimize the PCB dimensions and the nets were routed with traces of different width; the minimum trace width was imposed by the maximum current that would flow on them or according to the producer specifications (6 mill).
In figures 4.2 and 4.3 are shown the pictures o the final gerber files sent to the *Seed Studio* manufacturer. According to their requirements the sent file in order to process the board were:

- drill file (.drl)
- board edge cut gerber file
- front copper gerber file
- front silkscreen gerber file
- front soldermask gerber file
- back copper gerber file
- back silkscreen gerber file
- back soldermask gerber file

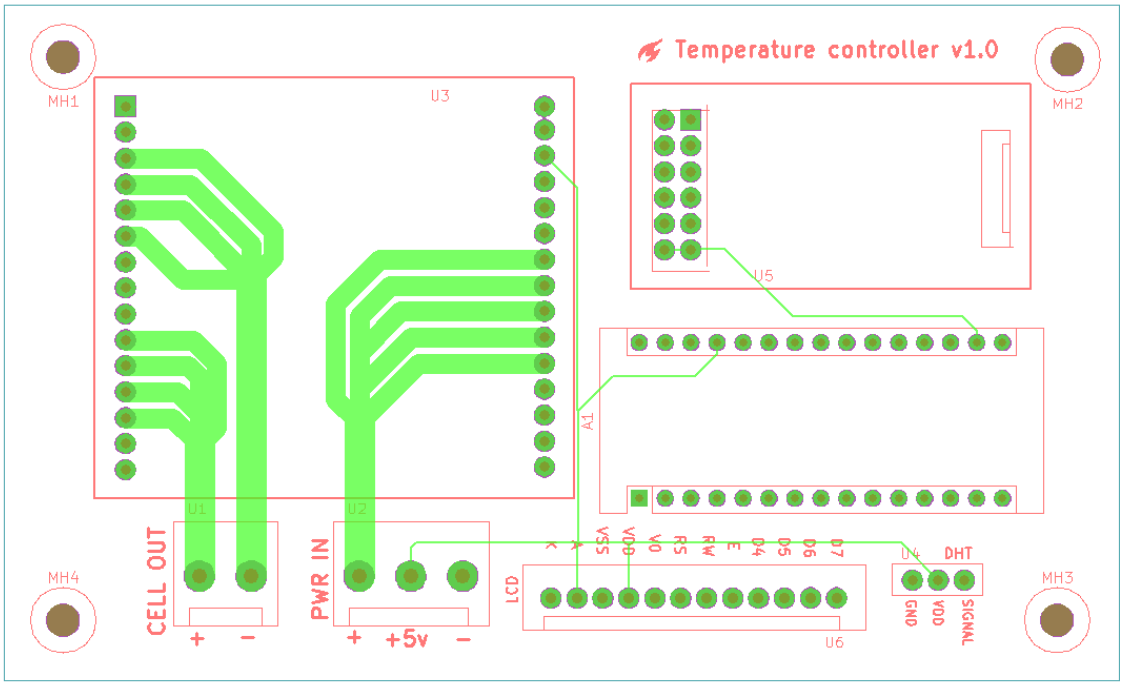

Figure 4.2: Front side of the board gerber files

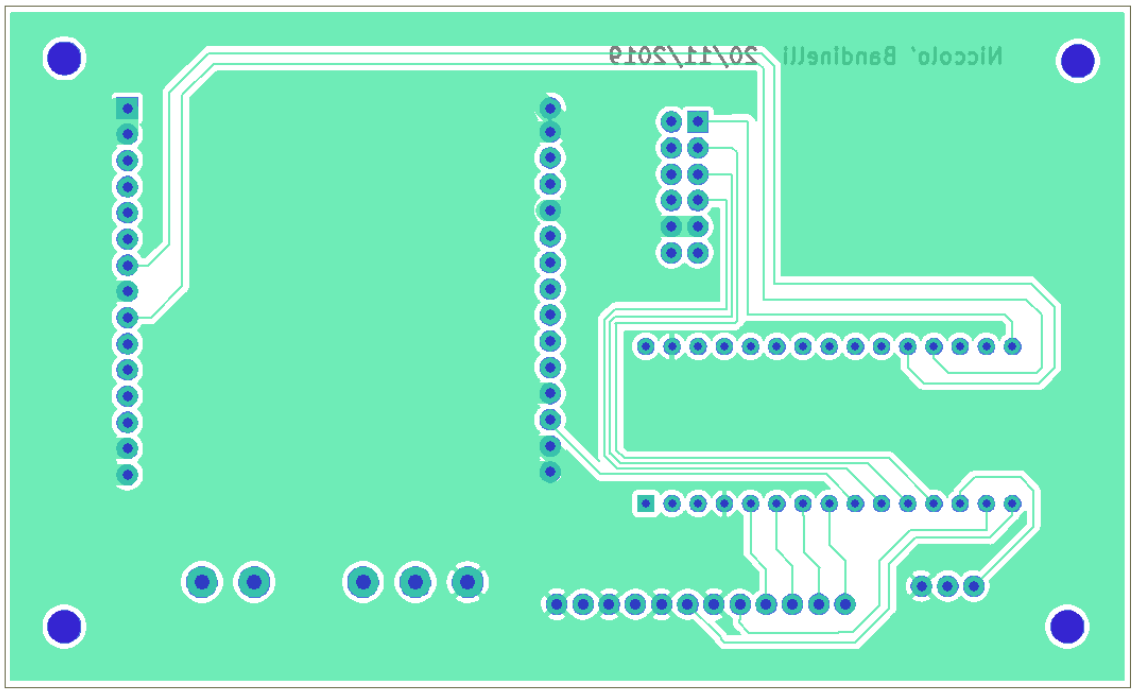

Figure 4.3: Back side of the board gerber files

Chapter 5

Board assembly and final test

Finally the board were assembled and tested. In figures 5.1 and 5.2 the final board assembly is shown, whereas in figure 3.2 the test response in time is represented.

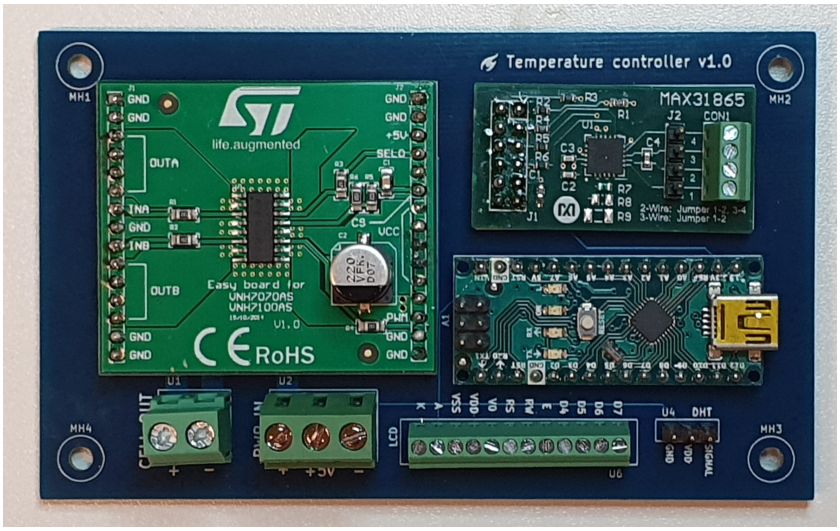

Figure 5.1: Picture of the final assembled board

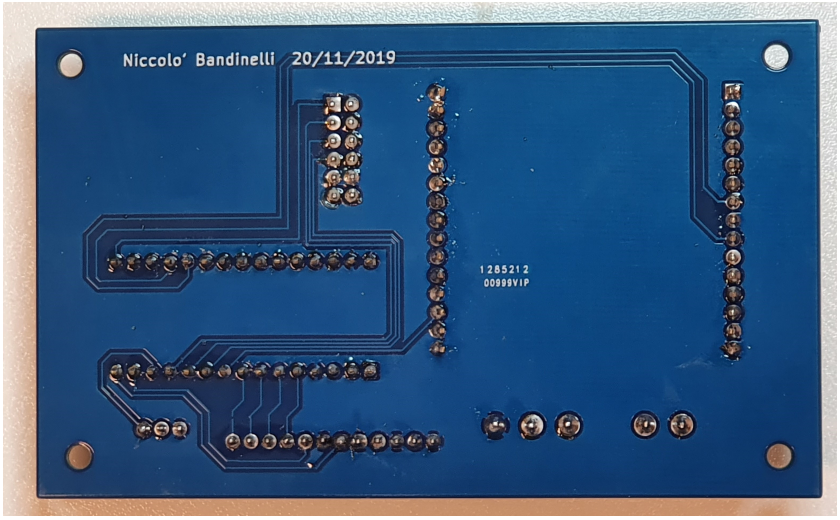

Figure 5.2: Picture of the back of the assembled board

The controller parameters can be easily set with a PC using a serial communication. The controller sends each 100ms the internal parameters to the computer and the user can update the target temperature by writing the desired temperature with the keyboard and pressing enter. The sent parameters are:

1. Substrate temperature
2. Set temperature
3. Target temperature
4. PWM output

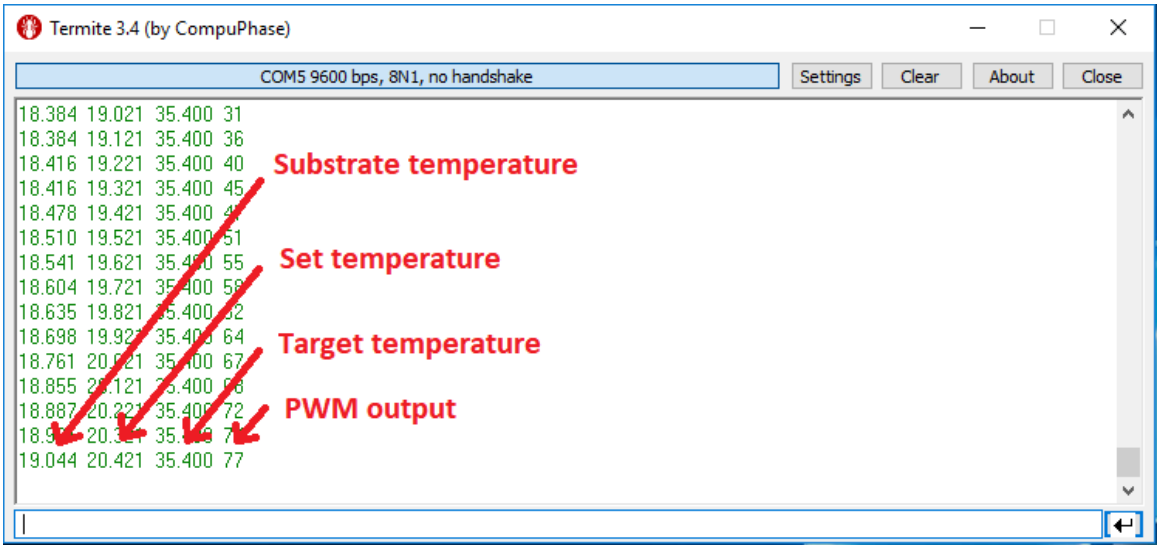

Figure 5.3: Serial interface for the controller

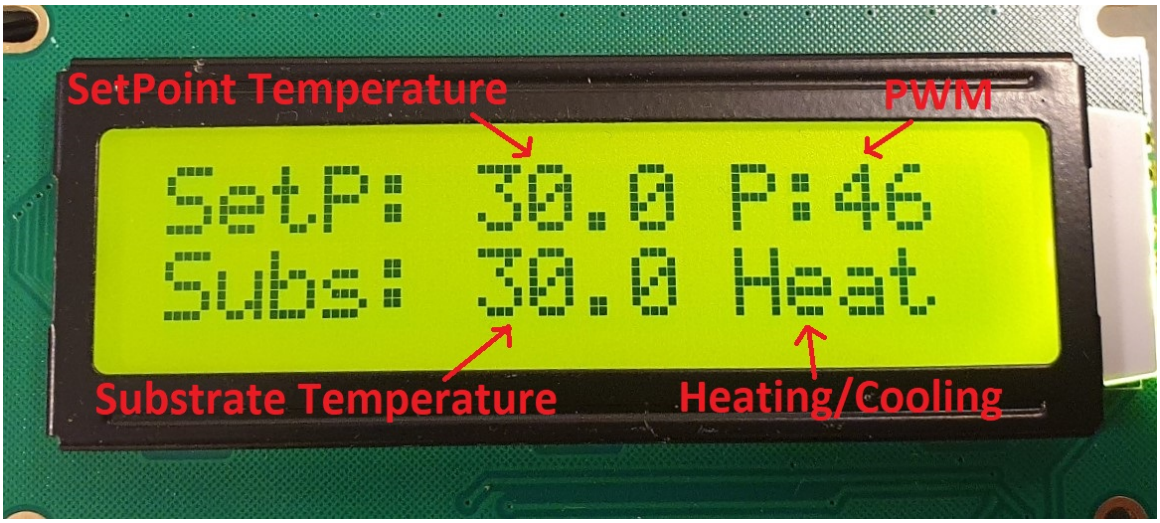

Figure 5.4: LCD display

5.1 Calibration

After the assembly, the controller temperature block composed by the RTD sensor and the MAX31865PMB readout circuitry has been tested using an external temperature sensor. The sensor used was the SENSIRION SHT31 reporting ±0.3°C accuracy and mounted on a Sensirion development board. In order to do the calibration, a temperature has been set on the TEC controller and the actual temperaure of the substrate has been checked using the SHT31. In picture 5.5 the test setup is shown whereas in table 5.1 the results of the calibration are summarized. We conclude that our temperature sensor block work properly and within the accuracy range we expected.

Controller set temperature	**SHT 31 temperature**
25 °	25.1 °
30 °	30 °
35 °	34.9 °
40 °	40 °
45 °	45.2 °

Table 5.1: Temperature check summary

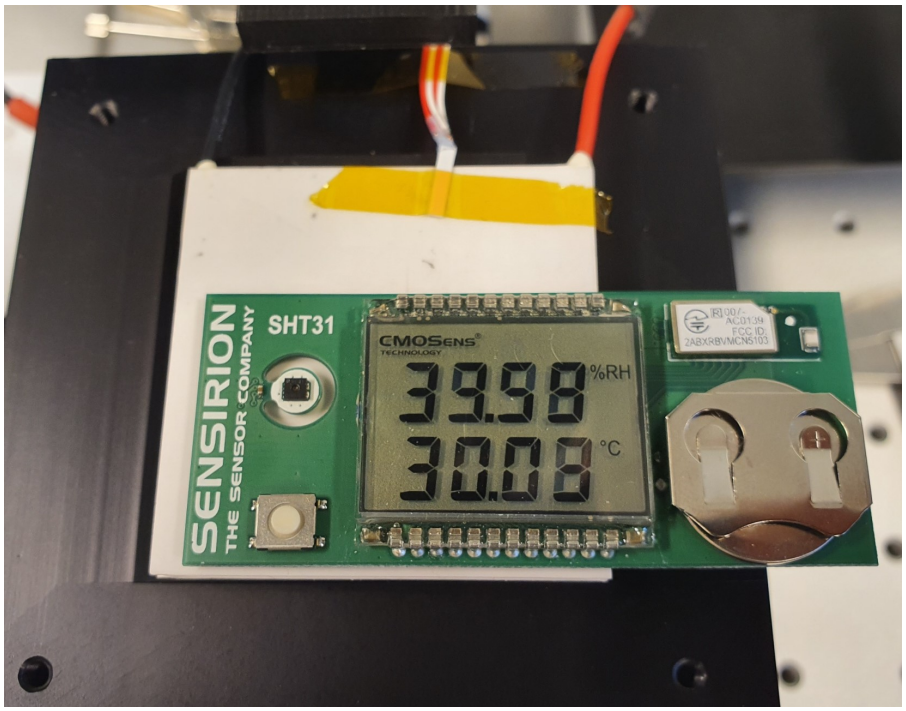

Figure 5.5: Temperature check setup

Chapter 6

Mechanical assembly

The TEC element has been placed on a heat sink in order to maximize its heating efficiency. The chosen heat sink was the ARCTIC Alpine 12 Passive. The final step was to design and build a mechanical assembly able to hold the heat sink element on the assembly sliding motor. A custom holder has been designed using Autodesk Sketchbook and 3D printed. In figure 6.2 the 3D design of the holder is shown while picture 6.1 show the final result of the completed assembly.

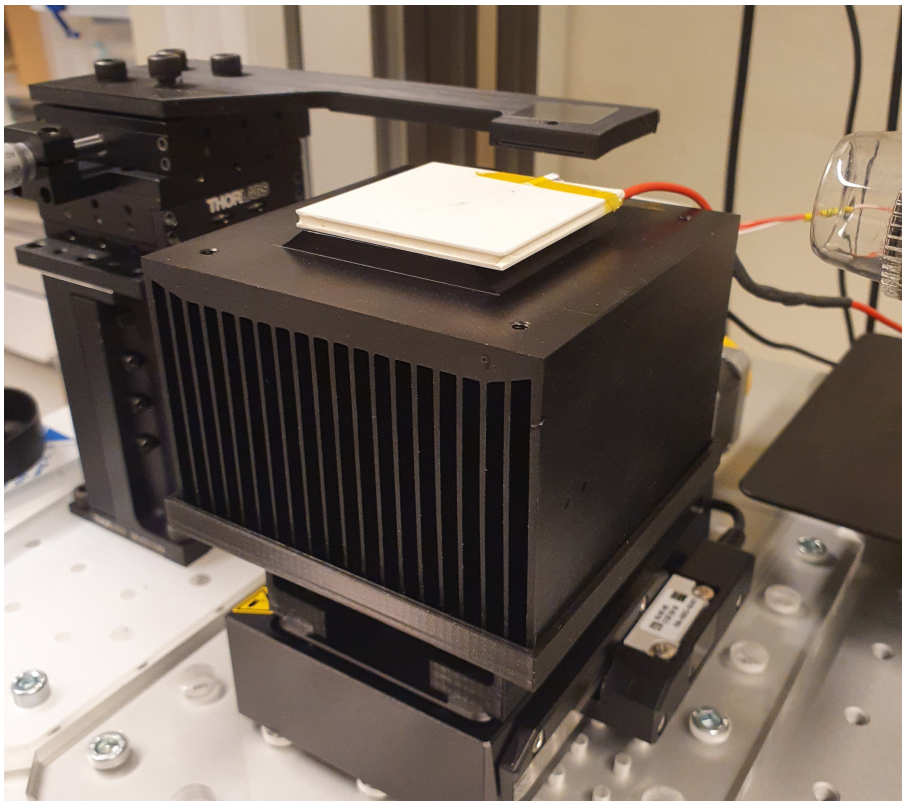

Figure 6.1: Final setup of the temperature controller

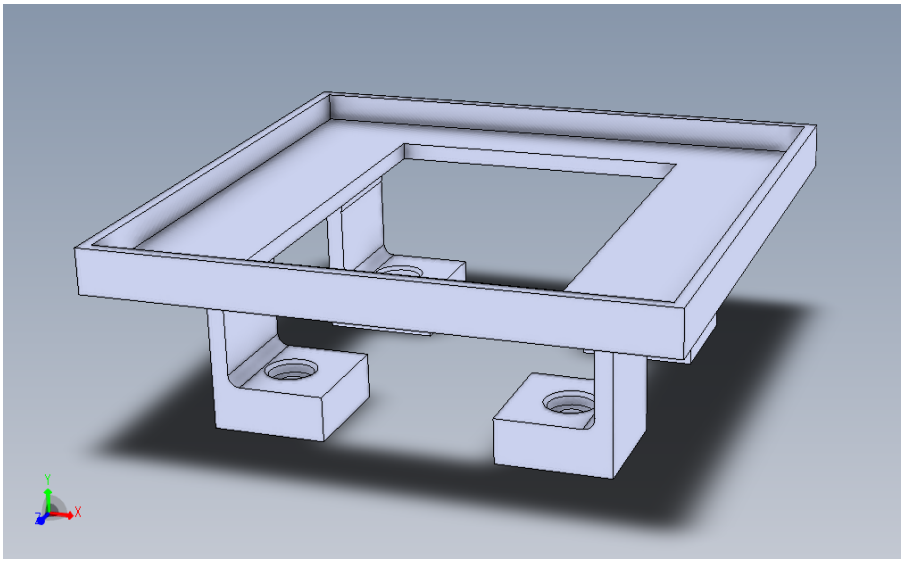

Figure 6.2: 3D mount for the heater

Chapter 7

Firmware

The TEC controller has been programmed using C language and Arduino IDE in order to speed up the process. The firmware has been written and debugged directly on the hardware. In order to make this controller more reliable, a fault detection mechanism has been implemented in the firmware.

7.1 Fault Detection

Two main fault can be identified that could in principle compromise the experiment or the circuit functionality:

1. The temperature sensor detach from the substrate: in this case the temperature detected by the sensor would be less than the target one. This would lead to a continuous increment of the controller output power reaching the maximum. In this case the controller will not work properly any more, moreover maximum delivered power to the TEC cell for long time could increase the temperature too much leading to a damage.

2. The power supply is disconnected or broken: in this case like in the previous one the temperature detected by the sensor would be less that the target one (actually no power is delivered to the cell). This would lead to a continuous increment of the output power reaching the maximum. Also in this case the controller will not work properly any more.

In order to detect these two fault a simple timer has been implemented in the firmware. If the output power stays at its maximum value (255) for more than 5 minutes one of the two faults certainly occurred. An error message is displayed and the output power is set to 0. The operator should check the power supply and the temperature sensor position and restart the controller.

7.2 Firmware code

```
1  #include <Adafruit_MAX31865.h>
2  #include <LiquidCrystal.h>
3  #include <dht11.h>
4  #include <PID_v1.h>
5
6  #define DHT11_PIN 10
7  #define outputPWM 6
8  #define RREF      400.0 //reference resistance on MAX
9  #define RNOMINAL  100.0 //nominal resistance of PT100
10 #define heatingRate 1 // [C/sec]
11
```

```
bool heating = true;
bool panicButton = false;
bool stringComplete;

double setpointT, substrateT, targetT, PWM, dewP;
String inString = "";    // string to hold input

float error, input, output, P_value, Bias_value;

Adafruit_MAX31865 max = Adafruit_MAX31865(13, 9, 8, 7);
LiquidCrystal lcd(12,11,2,3,4,5);   //rs, en, d4, d5, d6, d7
dht11 DHT;
PID myPID(&substrateT,&PWM,&setpointT,45,8,0,DIRECT);

int refreshRate = 100; //time needed to do a loop cycle

int updateTime = 1; //Serial and LCD update time in seconds
int errorTime =60; //Time in seconds with maximum PWM output before
   swithing off the cell (for security)
int errorT=0; //error timer variable
int updateT=0; //error timer variable


void setup() {
Serial.begin(9600);
lcd.begin(16, 2);
max.begin(MAX31865_4WIRE);  // set to 2WIRE or 4WIRE as necessary
pinMode(outputPWM, OUTPUT);
pinMode(A0, OUTPUT);  //INA
pinMode(A1, OUTPUT);  //INB
myPID.SetMode(AUTOMATIC);

//startup message
lcd.setCursor(0, 0);
lcd.print("TEMPERATURE");
lcd.setCursor(0, 2);
lcd.print("CONTROLLER v1.0");
Serial.println("Temperature controller v1.0");

analogWrite(outputPWM, 0);

delay(1000);

substrateT = max.temperature(RNOMINAL, RREF);
setpointT = 20;
targetT = 20;  // target is by default set to substrateT at the beginning

delay(1000);
}
```

```
void loop() {

float incomingNumber=0;
if (stringComplete) {
incomingNumber = inString.toFloat();
targetT = incomingNumber;
inString = "";
stringComplete = false;
}


// update the setpointT  to targetT if different
setpointT=updateSetpointT(setpointT,targetT);


//apply PI control
substrateT = max.temperature(RNOMINAL, RREF);
myPID.Compute();
heating=true;
digitalWrite(A0, heating);
digitalWrite(A1, !heating);

//We define PWM range between 0 and 255
if (PWM < 0)
PWM = 0;
if (PWM > 255)
PWM = 255;

//safety timer -> if PWM=255 for more that errorTime seconds -> ERROR
if(PWM==255)
errorT=errorT+1;
else
errorT=0;

if(errorT*(refreshRate/1000.0)>errorTime){
// switch current off
analogWrite(outputPWM, 0);
panicButton = true;
}else{
// update the pwm output value
analogWrite(outputPWM, PWM);
panicButton=false;
}

// update serial and lcd every updateTime seconds
if(updateT*(refreshRate/1000.0)>updateTime){
updateInterface(targetT,substrateT,heating,setpointT,PWM,panicButton);
updateT=0;
}

updateT=updateT+1;
```

```
}


float computeDewpoint(float humi, float temp) {
float k;
k = log(humi / 100) + (17.62 * temp) / (243.12 + temp);
return 243.12 * k / (17.62 - k);
}

void serialEvent() {
while (Serial.available()) {
// get the new byte:
char inChar = (char)Serial.read();
// add it to the inputString:
inString += inChar;
// if the incoming character is a newline, set a flag so the main loop
    can
// do something about it:
if (inChar == '\n') {
stringComplete = true;
}
}
}

// update serial and lcd every updateTime seconds
void updateInterface(double targetT,double substrateT,boolean heating,
    double setpointT,double PWM,boolean panicButton){

if(panicButton==false){

// update data on LCD
lcd.clear();
lcd.setCursor(0, 0);
lcd.print("SetP: ");
lcd.print(targetT, 1);
lcd.setCursor(0, 2);
lcd.print("Subs: ");
lcd.print(substrateT, 1);
lcd.setCursor(11, 2);
if(heating){
lcd.print("Heat");
} else {
lcd.print("Cool");
}
lcd.setCursor(11, 0);
lcd.print("P:");
lcd.print(PWM, 0);

// update data on the serial line
Serial.print(substrateT, 3);
Serial.print("  ");
```

```
Serial.print(setpointT, 3);
Serial.print("  ");
Serial.print(targetT, 3);
Serial.print("  ");
Serial.println(PWM, 0);
} else {

// update data on LCD
lcd.clear();
lcd.setCursor(0, 0);
lcd.print("ERROR");
lcd.setCursor(0, 2);
lcd.print("CHECK TEMP SENS");

// update data on the serial line
Serial.println("Error, check the temperature sensor or the power supply!"
   );
}
}

// update the setpointT  to targetT if different
double updateSetpointT(double setpointT,double targetT){

if(setpointT != targetT){
if(setpointT > targetT){
setpointT = setpointT - (heatingRate*(refreshRate/1000.0));
}
if(setpointT < targetT){
setpointT = setpointT + (heatingRate*(refreshRate/1000.0));
}
}
return setpointT;
}
```

Bibliography

[1] RTD temperature evaluation by Analog

[2] TEC powered with PWM/DC

[3] Manufacturers datasheet

Part VI

APPENDIX B: Cleanroom flowchart

Transfer-free graphene process on Molybdenum catalyst

Flow chart

Version
15 November 2019
Professor Sten Vollebregt

EC2422
Process engineer: Niccolò Bandinelli
Start: 25 November 2019
Contamination: No
Labs: CR100, CR10000

EKL(Else Kooi Laboratory)
DELFT UNIVERSITY OF TECHNOLOGY

Address : Feldmannweg 17, 2628 CT Delft, The
P.O. Box: 5053, 2600 GB Delft, The Netherlands
Phone : +31 - (0)15 - 2783868
Fax : +31 - (0)15 - 2622163
Website : http://ekl.tudelft.nl/EKL/Home.php

Detailed information about possible contamination:

Place/Clean Rooms used in process:

- **Write the sequence of used labs from start to finish.**
- **Which (Non-standard) materials or process steps**
- **What kind of process or machine was used?**
- **The other materials that wafers contain that are also processed on this machine**

Lab/Clean room	**(Non-standard) material/ process steps**	Process/Machine/	Other materials used in machine
CR100	non	non	non
CR10000	Yes, graphene	BlackMagic	Cu, Pt, Ni
SAL			
CR100		Litho on PAS5500/80	
MEMS			

If other labs are used:

Write the steps number: Possible contamination issues/materials.

None

If there are non-standard processing steps in a standard process: Write down the steps number, the material and machine that is used.

Step number	Material	Machine/Tool

One litho step has to be performed after the graphene growth on the waferstepper. For this manual coating and development on contaminated chucks will be used. During exposure the special contaminated wafer carrier will be used.

STARTING MATERIAL

Use 6 **single side polished process wafers**, with the following specifications:

Type:	p-type
Orientation:	1-0-0, 0 deg off orientation
Resistivity:	2-5 Ωcm
Thickness:	525 ± 15 µm
Diameter:	100.0 ± 0.2 mm

Wafers taken out of an already opened box must be cleaned before processing, according to the standard procedure.
Wafers taken out of an unopened wafer box do not have to be cleaned before processing**.**
(Use Si* cleaning line)

EC2081

1. OXIDATION WAFER 1, 2 and 3

Furnace no: C1 or D1

Target thickness: 90 nm

Program name: DRYOXID 1 hours 8 min at 1050 °C (check the furnace temperature!)

PROCESS	TEMPERATURE (in oC)	GASSES & FLOWS (in liter/min)	TIME (in minutes)	REMARKS
boat in	800	nitrogen: 3.0 oxygen: 0.3	5	
stabilize	800	nitrogen: 3.0 oxygen: 0.3	10	
heat up	+10 oC/min	nitrogen: 3.0 oxygen: 0.3	30	
stabilize	1050	nitrogen: 3.0 oxygen: 0.3	10	
oxidation	1050	nitrogen: 2.25 oxygen: 3.85	68	
cool down	-5 oC/min	nitrogen: 3.0	100	wait for operator
boat out	600	nitrogen: 3.0	5	

NOTE: The total process time can be slightly reduced in the "cool down" step: the "boat out" step can be started after ± 60 minutes, when the actual temperature of the furnace will be about 800 oC.

2. OXIDATION WAFER 4, 5 and 6

Furnace no: C1 or D1

Target thickness: 600 nm

Program name: WET1000 1 hour 56 minutes at 1000 °C (check furnace temperature!)

PROCESS	TEMPERATURE (in oC)	GASSES & FLOWS (in liter/min)	TIME (in minutes)	REMARKS
boat in	800	nitrogen: 3.0 oxygen: 0.3	5	
stabilize	800	nitrogen: 3.0 oxygen: 0.3	10	
heat up	+10 oC/min	nitrogen: 3.0 oxygen: 0.3	30	
stabilize	1050	nitrogen: 3.0 oxygen: 0.3	10	
oxidation	1050	nitrogen: 2.25 oxygen: 3.85	116	
cool down	-5 oC/min	nitrogen: 3.0	100	wait for operator
boat out	600	nitrogen: 3.0	5	

NOTE: The total process time can be slightly reduced in the "cool down" step: the "boat out" step can be started after ± 60 minutes, when the actual temperature of the furnace will be about 800 oC.

3. MEASUREMENT: OXIDE THICKNESS on wafer 1, 2 and 3

Use the Leitz MPV-SP measurement system to measure the oxide thickness:

Program: Th. SiO2 on Si, >50nm auto5pts

Oxide thickness: 90 nm

4. MEASUREMENT: OXIDE THICKNESS on wafer 4, 5 and 6

Use the Leitz MPV-SP measurement system to measure the oxide thickness:

Program: Th. SiO2 on Si, >50nm auto5pts

Oxide thickness: 600 nm

5. Catalyst deposition @ Class 100

Use the TRIKON SIGMA sputter coater for the deposition of the catalyst metal Mo layer on the process wafers.
Follow the operating instructions from the manual when using this machine.

Mo: 50 nm, recipe Mo_50nm_50C_slow

Visual inspection: the metal layer must look shiny.

6. Graphene growth @ Class 10000 on wafer 1 and 4

Use the AIXTRON BlackMagic Pro to grow graphene. Use recipe: Mo_NEW_915C_20minCH4
Use graphene reactor interior (Cu contaminated)!

USE RED BOX WITH Cu WRITTEN ON IT

7. **COATING AND BAKING on wafer 2, 3, 5 and 6**

Use the EVG 120 wafertrack to coat the wafers with resist, and follow the instructions specified for this equipment.
The process consists of a treatment with HMDS (hexamethyldisilazane) vapor with nitrogen as a carrier gas,
spin coating with Shipley SPR3012 positive photoresist, and a soft bake at 95degC for 90 seconds.
Always check the temperature of the hotplate and the relative humidity (48 ± 2 %) in the room first.

Use program "**1-Co - 3012 - 1,4µm**".

8. **ALIGNMENT AND EXPOSURE: SN**

Processing will be performed on the ASM PAS 5500/80 automatic waferstepper.
Follow the operating instructions from the manual when using this machine.

Use EC2125 **mask** (box ?), job Diesize_10mm/DIE10x10_4IMG, layer ID = 2, and the exposure energy E = 55 ?mJ/cm^2.
Mask name = 2x2

9. **DEVELOPMENT**

Use the developer station of the EVG120 system to develop the wafers. The process consists of:

- a post-exposure bake at 115 °C for 90 seconds
- developing with Shipley MF322 with a single puddle process
- a hard bake at 100 °C for 90 seconds

Always follow the instructions for this equipment.

Use program "**1-Dev - SP**".

10. PLASMA ETCHING OF MOLYBDENUM

Use the Trikon Ωmega 201 plasma etcher.
Follow the operating instructions from the manual when using this machine.
The process conditions of the etch program may not be changed !

Use sequence **MO_TEST2** and set the platen temperature to **25 °C**. For 30 seconds
Perform a test on one wafer first and check for Mo etching residues and SiO_2 over-etch.

11. RESIST STRIPPING with Tepla

Use the Tepla plasma system to remove the photoresist in an oxygen plasma.
Follow the instructions specified for the Tepla stripper, and use the quartz carrier.
Use program 1

12. Graphene growth @ Class 10000 on wafer 2, 3, 5 and 6

Use the AIXTRON BlackMagic Pro to grow graphene. Use recipe: Mo_NEW_915C_20minCH4

Use graphene reactor interior (Cu contaminated)!

Acknowledgements

I would like to express my gratitude to professors Mastrangeli and Vollebregt, that guided me during my experience in Delft: their advices and their positivity helped quite a lot overcoming obstacles on my path. A deep gratitude goes to professor Cocuzza, his passion and enthusiasm during lessons inspired me to follow this path. I would like also to thank all the EKL staff, in particular: Mario, Silvana, Tom and Johannes for introducing me to the wonderful world of cleanroom. Thanks to all my Delft colleague for their help, a special thank to Gandika that helped me a lot with AFM. I would like to thanks all my friends and colleague that I met in Turin. Thanks specially to Yaquian, my super office roommate that warmed a bit the cold Dutch winter. Thanks to my closest friends Camilla, Valentina and Giulia for their care and finally, at last but not least my deepest thank goes to my family.

List of Figures

List of Tables

Bibliography

[1] K. S. Novoselov, A. K. Geim, S. V. Morozov, D. Jiang, Y. Zhang, S. V. Dubonos, I. V. Grigorieva, and A. A. Firsov, "Electric field effect in atomically thin carbon films," *Science*, vol. 306, no. 5696, pp. 666–669, 2004.

[2] J. Warner, F. Schaffel, M. Rummeli, and A. Bachmatiuk, *Graphene: Fundamentals and emergent applications*. Elsevier Science, 2012.

[3] M. I. Mikhail Katsnelson, *Graphene: Carbon in Two Dimensions*. Cambridge University Press, 2012.

[4] A. Geim and K. Novoselov, "The rise of graphene," *Nature materials*, vol. 6, pp. 183–91, 04 2007.

[5] N. Peres, "Graphene, new physics in two dimensions," *Europhysics News*, vol. 40, no. 3, pp. 17–20, 2009.

[6] ISO, "Ts 80004-13:2017," 2017.

[7] C. Lee, X. Wei, J. W. Kysar, and J. Hone, "Measurement of the elastic properties and intrinsic strength of monolayer graphene," *Science*, vol. 321, no. 5887, pp. 385–388, 2008.

[8] D. G. Papageorgiou, I. A. Kinloch, and R. J. Young, "Mechanical properties of graphene and graphene-based nanocomposites," *Progress in Materials Science*, vol. 90, pp. 75 – 127, 2017.

[9] W. A. de Heer, C. Berger, X. Wu, M. Sprinkle, Y. Hu, M. Ruan, J. A. Stroscio, P. N. First, R. Haddon, B. Piot, and et al., "Epitaxial graphene electronic structure and transport," *Journal of Physics D: Applied Physics*, vol. 43, p. 374007, Sep 2010.

[10] A. Kumar and C. H. Lee, "Synthesis and biomedical applications of graphene : Present and future trends (chapter 3)," 2018.

[11] X. Chen, L. Zhang, and S. Chen, "Large area cvd growth of graphene," *Synthetic Metals*, vol. 210, pp. 95 – 108, 2015. Reviews of Current Advances in Graphene Science and Technology.

[12] S. Hofmann, P. Braeuninger, and R. Weatherup, "Cvd-enabled graphene manufacture and technology," *The journal of physical chemistry letters*, vol. 6, pp. 2714–2721, 07 2015.

[13] Y. Wu, G. Yu, H. Wang, B. Wang, Z. Chen, Y. Zhang, B. Wang, X. Shi, X. Xie, Z. Jin, and X. Liu, "Synthesis of large-area graphene on molybdenum foils by chemical vapor deposition," *Carbon*, vol. 50, no. 14, pp. 5226 – 5231, 2012.

[14] Q. Yu, J. Lian, S. Siriponglert, H. Li, Y. P. Chen, and S.-S. Pei, "Graphene segregated on ni surfaces and transferred to insulators," *Applied Physics Letters*, vol. 93, no. 11, p. 113103, 2008.

[15] Y. Zhang, L. Gomez, F. N. Ishikawa, A. Madaria, K. Ryu, C. Wang, A. Badmaev, and C. Zhou, "Comparison of graphene growth on single-crystalline and polycrystalline ni by chemical vapor deposition," *The Journal of Physical Chemistry Letters*, vol. 1, no. 20, pp. 3101–3107, 2010.

[16] X. Li, W. Cai, J. An, S. Kim, J. Nah, D. Yang, R. Piner, A. Velamakanni, I. Jung, E. Tutuc, S. K. Banerjee, L. Colombo, and R. S. Ruoff, "Large-area synthesis of high-quality and uniform graphene films on copper foils," *Science*, vol. 324, no. 5932, pp. 1312–1314, 2009.

[17] B. Wang, Y. Zhang, Z. Chen, Y. Wu, Z. Jin, X. Liu, L. Hu, and G. Yu, "High quality graphene grown on single-crystal mo(110) thin films," *Materials Letters*, vol. 93, pp. 165 – 168, 2013.

[18] Y. Grachova, S. Vollebregt, A. L. Lacaita, and P. M. Sarro, "High quality wafer-scale cvd graphene on molybdenum thin film for sensing application," *Procedia Engineering*, vol. 87, pp. 1501 – 1504, 2014. EUROSENSORS 2014, the 28th European Conference on Solid-State Transducers.

[19] S. Vollebregt, B. Alfano, F. Ricciardella, A. J. M. Giesbers, Y. Grachova, H. W. van Zeijl, T. Polichetti, and P. M. Sarro, "A transfer-free wafer-scale cvd graphene fabrication process for mems/nems sensors," pp. 17–20, Jan 2016.

[20] F. Ricciardella, S. Vollebregt, E. Kurganova, A. Giesbers, M. Ahmadi, and L. Sarro, "Growth of multi-layered graphene on molybdenum catalyst by solid phase reaction with amorphous carbon," 04 2019.

[21] Y. Dong, Y. Xie, C. Xu, Y. Fu, X. Fan, X. Li, L. Wang, F. Xiong, W. Guo, G. Pan, Q. Wang, F. Qian, and J. Sun, "Transfer-free, lithography-free and fast growth of patterned CVD graphene directly on insulators by using sacrificial metal catalyst," *Nanotechnology*, vol. 29, p. 365301, jun 2018.

[22] F. Ricciardella, S. Vollebregt, B. Boshuizen, F. Danzl, I. Cesar, P. Spinelli, and P. Sarro, "Wafer-scale transfer-free process of multi-layered graphene grown by chemical vapor deposition," *Materials Research Express*, 02 2020.

[23] A. Ferrari and D. Basko, "Raman spectroscopy as a versatile tool for studying the properties of graphene," *Nature nanotechnology*, vol. 8, pp. 235–46, 04 2013.

[24] K. Schneider, A. Bräuer, M. Fleischer, and D. P. Kern, "Graphite/graphene grown on molybdenum via cvd," pp. 481–484, July 2015.

[25] W. Z. L. Wang, *Scanning Microscopy for Nanotechnology.* Springer, 2007.

[26] R. Jagtap and A. Ambre, "Atomic force microscopy (afm): Basics and its important applications for polymer characterization: An overview," *Indian Journal of Engineering & Materials Sciences*, vol. 13, pp. 368–384, 09 2006.

[27] F.-G. Bănică, *Chemical Sensors and Biosensors: Fundamentals and Applications*. 08 2012.

[28] S. Capone, A. Forleo, L. Francioso, R. Rella, P. Siciliano, J. Spadavecchia, D. Presicce, and A. Taurino, "Solid state gas sensors: State of the art and future activities," *Cheminform*, vol. 35, 07 2004.

[29] F. Schedin, A. Geim, S. Morozov, E. Hill, P. Blake, M. Katsnelson, and K. Novoselov, "Detection of individual gas molecules adsorbed on graphene," *Nature materials*, vol. 6, pp. 652–5, 10 2007.

[30] W. Yuan and G. Shi, "Graphene-based gas sensors," *J. Mater. Chem. A*, vol. 1, 08 2013.

[31] S. Hwang, J. Lim, H. Park, W. Kim, S. Song, J. H. Kim, S. Lee, D. Woo, and S. C. Jun, "Chemical vapor sensing properties of graphene based on geometrical evaluation," *Current Applied Physics*, vol. 12, p. 1017–1022, 07 2012.

[32] W. Tian, X. Liu, and W. Yu, "Research progress of gas sensor based on graphene and its derivatives: A review," *Applied Sciences*, vol. 8, p. 1118, 07 2018.

[33] B. Guo, F. Liang, B. Zhang, and J. R. Gong, "Graphene doping: A review," *Insciences Journal*, vol. 1, pp. 80–89, 04 2011.

[34] G. Lee, G. Yang, A. Cho, J. W. Han, and J. Kim, "Defect-engineered graphene chemical sensors with ultrahigh sensitivity," *Phys. Chem. Chem. Phys.*, vol. 18, pp. 14198–14204, 2016.

[35] G. Mastrapa and F. Freire, "Plasma-treated cvd graphene gas sensor performance in environmental condition: The role of defects on sensitivity," *Journal of Sensors*, vol. 2019, pp. 1–7, 11 2019.

[36] F. Ricciardella, S. Vollebregt, T. Polichetti, B. Alfano, E. Massera, and L. Sarro, "High sensitive gas sensors realized by a transfer-free process of cvd graphene," 11 2016.

[37] F. Ricciardella, S. Vollebregt, T. Polichetti, B. Alfano, E. Massera, and P. Sarro, "Low temperature cvd grown graphene for highly selective gas sensors working under ambient conditions †," vol. 1, 08 2017.

[38] F. Ricciardella, S. Vollebregt, T. Polichetti, M. Miscuglio, B. Alfano, M. L. Miglietta, E. Massera, G. Di Francia, and P. M. Sarro, "Effects of graphene defects on gas sensing properties towards no2 detection," *Nanoscale*, vol. 9, pp. 6085–6093, 2017.

[39] K. Pi, K. M. McCreary, W. Bao, W. Han, Y. F. Chiang, Y. Li, S.-W. Tsai, C. N. Lau, and R. K. Kawakami, "Electronic doping and scattering by transition metals on graphene," *Phys. Rev. B*, vol. 80, p. 075406, Aug 2009.

[40] Y. Ren, S. Chen, W. Cai, Y. Zhu, C. Zhu, and R. Ruoff, "Controlling the electrical transport properties of graphene by in situ metal deposition," *Applied Physics Letters*, vol. 97, pp. 053107–053107, 08 2010.

[41] S. W. Huh, J. Park, K. S. Kim, B. H. Hong, and S. B. Kim, "Selective n-type doping of graphene by photo-patterned gold nanoparticles.," *ACS nano*, vol. 5 5, pp. 3639–44, 2011.

[42] Y. Wu, W. Jiang, Y. Ren, W. Cai, W. Lee, H. Li, R. Piner, C. Pope, Y. Hao, H. Ji, J. Kang, and R. Ruoff, "Tuning the doping type and level of graphene with different gold configurations," *Small (Weinheim an der Bergstrasse, Germany)*, vol. 8, pp. 3129–36, 10 2012.

[43] M. Gautam and A. H. Jayatissa, "Detection of organic vapors by graphene films functionalized with metallic nanoparticles," 2012.

[44] J. Eriksson, D. Puglisi, Y. H. Kang, R. Yakimova, and A. L. Spetz, "Adjusting the electronic properties and gas reactivity of epitaxial graphene by thin surface metallization," *Physica B: Condensed Matter*, vol. 439, pp. 105 – 108, 2014. 5th South African Conference on Photonic Materials (SACPM 2013).

[45] Y.-H. Zhang, K.-G. Zhou, K.-F. Xie, J. Zeng, H.-L. Zhang, and Y. Peng, "Tuning the electronic structure and transport properties of graphene by noncovalent functionalization: effects of organic donor, acceptor and metal atoms," *Nanotechnology*, vol. 21, p. 065201, jan 2010.

[46] Y. Zou, F. Li, Z. H. Zhu, M. W. Zhao, X. G. Xu, and X. Y. Su, "An ab initio study on gas sensing properties of graphene and si-doped graphene," *The European Physical Journal B*, vol. 81, pp. 475–479, Jun 2011.

[47] D. Singh, A. Kumar, and D. Kumar, "Adsorption of small gas molecules on pure and al-doped graphene sheet: a quantum mechanical study," *Bulletin of Materials Science*, vol. 40, pp. 1263–1271, Oct 2017.

[48] S. Ni, L. Isa, and H. Wolf, "Capillary assembly as a tool for the heterogeneous integration of micro- and nanoscale objects," *Soft Matter*, vol. 14, 03 2018.

[49] N. Vogel, M. Retsch, C.-A. Fustin, A. Campo, and U. Jonas, "Advances in colloidal assembly: The design of structure and hierarchy in two and three dimensions," *Chemical reviews*, vol. 115, 06 2015.

[50] P. Lambert, *Surface Tension in Microsystems: Engineering Below the Capillary Length*. 01 2013.

[51] R. Deegan, O. Bakajin, T. Dupont, G. Huber, S. Nagel, and T. Witten, "Capillary flow as the cause of ring stains from dried liquid drops," *Nature*, vol. 389, pp. 827–829, 10 1997.

[52] T. Kraus, L. Malaquin, H. Schmid, W. Riess, N. Spencer, and H. Wolf, "Nanoparticle printing with single-particle resolution," *Nature nanotechnology*, vol. 2, pp. 570–6, 09 2007.

[53] L. Malaquin, T. Kraus, H. Schmid, E. Delamarche, and H. Wolf, "Controlled particle placement through convective and capillary assembly," *Langmuir : the ACS journal of surfaces and colloids*, vol. 23, pp. 11513–21, 12 2007.

[54] P. Born, S. Blum, A. Munoz, and T. Kraus, "Role of the meniscus shape in large-area convective particle assembly," *Langmuir : the ACS journal of surfaces and colloids*, vol. 27, pp. 8621–33, 06 2011.

[55] C. Kuemin, L. Nowack, L. Bozano, N. Spencer, and H. Wolf, "Oriented assembly of gold nanorods on the single-particle level," *Advanced Functional Materials*, vol. 22, pp. 702–708, 02 2012.

[56] S. Ni, J. Leemann, H. Wolf, and L. Isa, "Nanoparticle insights into mechanisms of capillary assembly," *Faraday Discuss.*, vol. 181, 12 2014.

[57] M. Asbahi, S. Mehraeen, F. Wang, N. Yakovlev, K. Chong, J. Cao, M. Tan, and J. Yang, "Large area directed self-assembly of sub-10 nm particles with single particle positioning resolution," *Nano letters*, vol. 15, 08 2015.

[58] D. Frenkel, *Order through disorder: Entropy-driven phase transitions*, vol. 415, pp. 137–148. 01 1970.

[59] V. Flauraud, M. Mastrangeli, G. D. Bernasconi, J. Butet, D. T. L. Alexander, E. Shahrabi, O. J. F. Martin, and J. Brugger, "Nanoscale topographical control of capillary assembly of nanoparticles," *Nature nanotechnology*, vol. 12, p. 73—80, January 2017.

[60] D. Virganavičius, M. Juodėnas, T. Tamulevičius, H. Schift, and S. Tamulevičius, "Investigation of transient dynamics of capillary assisted particle assembly yield," *Applied Surface Science*, vol. 406, pp. 136–143, 02 2017.

[61] Wikipedia, "Else kooi," 2020.

[62] S.-E. Zhu, S. Yuan, and G. Janssen, "Optical transmittance of multilayer graphene," *EPL (Europhysics Letters)*, vol. 108, 09 2014.

[63] Siyu, H. Huang, C. Yuan, L. Feng, M. Zhai, X. Shi, C. Qi, and G. Wang, "Thickness-dependent strain effect on the deformation of the graphene-encapsulated au nanoparticles," *Journal of Nanomaterials*, vol. 2014, pp. 1–6, 01 2014.

[64] B. Vasić, U. Ralević, K. C. Zobenica, M. M. Smiljanić, R. Gajić, M. Spasenović, and S. Vollebregt, "Low-friction, wear-resistant, and electrically homogeneous multilayer graphene grown by chemical vapor deposition on molybdenum," *Applied Surface Science*, vol. 509, p. 144792, 2020.

[65] E. Rut'kov, A. Tontegode, M. Usufov, and N. Gall, "Carbon interaction with heated molybdenum surface," *Applied Surface Science*, vol. 78, no. 2, pp. 179 – 184, 1994.

[66] V. Veldhoven and Z. August, "Integrated catalytic fabrication approaches for graphene-based electronic devices," 2019.